Precise Measurement of the Electric Dipole Moment of the τ Lepton at Belle

Dissertation

Division of Particle and Astrophysical Sciences,
Graduate School of Science,
Nagoya University, Japan

by
Kenji Inami

January, 2003

Preface

Tau lepton is the heaviest lepton among the elementary particles known to exist. This thesis describes my research on the τ lepton's electric dipole moment (EDM). The EDM manifests a fundamental property on the elementary particle. Especially its non-zero magnitude indicates presence of the new physics world beyond the Standard Model.

The data analyzed were accumulated during 1999-2001 by the KEKB/Belle experiment. KEKB is an e^+e^- asymmetric collider accelerator built at KEK and delivers us the world highest intense τ-pairs at $\sqrt{s} = 10.58\,\mathrm{GeV}$ in the process of $e^+e^- \to \tau^+\tau^-$. I have engaged in an international collaboration group for high energy physics experiment, named Belle, as a graduate student at Nagoya University for these 6 years, and took part specifically in constructing the Belle detector, particularly the central-drift-chamber, operating the experiment system to record data, producing and calibrating reconstruction parameters of the tracking system and analyzing the data to extract physics outcome. In the analysis, I investigated the optimal observable method, confirmed its analytical proof, calculated the matrix element and selected and analyzed the τ-lepton data. During this period, I have been fascinated with physics concept on space-time symmetry expressed as CP (Charge conjugation and Parity reflection) and T (Time reflection) transformations, and eager to search for any violation phenomenon of their invariance ever observed. Large amount of τ-lepton data accumulated at Belle, ever obtained in the world, could satisfy my thirst for knowledge and grow a ripe outcome as this thesis.

Acknowledgment

I greatly appreciate Prof. T. Ohshima for giving me a chance to study τ-physics and leading me with much encouragement. I would like to thank Prof. T. Iijima, Dr. A. Sugiyama, Dr. K. Senyo and the members of our laboratory for much help.

I would like to express my gratitude to Prof. K. Hagiwara for detailed instructions on the theoretical calculation and many helpful discussions. I also thank Professors O. Nachtmann and Z. Wąs for their constructive advice.

Further, I thank all members of the Belle collaboration. Especially, I would like to thank the collaborators; Professors H. Hayashii, S. I. Eidelman, B. Yabsley and H. Kichimi for many detailed discussions on the analysis. I also acknowledge the KEKB accelerator group for their excellent operation of the KEKB accelerator.

This research was supported by a Grant-in-Aid for JSPS Fellows (01655, 2001).

Abstract

To search for CP-violation (CPV) signatures in the lepton sector, an electric dipole moment, d_τ, of the τ lepton was measured using the $e^+e^- \to \tau^+\tau^-$ reaction collected with the Belle detector at the KEKB collider at $\sqrt{s} = 10.58\,\mathrm{GeV}$. This is a good probe of new physics beyond the Standard Model (SM), since such physics produce the CPV in the lepton sector, though the SM does not predict any appreciable effect, and such effect is expected to be enhanced for τ leptons due to their large mass.

An *optimal observable method* was adopted to extract d_τ, which uses all experimentally available information of the spin and momenta of the τ decays, and maximizes the sensitivity to d_τ. By extracting the conversion parameters from the observables to d_τ using a full Monte Carlo simulation with the electric dipole moment effect, the systematic uncertainties arising from the detector acceptance effect were successfully suppressed.

All of the results are consistent with zero-EDM within the errors. Using 29.5 fb^{-1} data, which correspond to 26.8 million generated τ-pair events, the following result was obtained:

$$Re(d_\tau) = (1.15 \pm 1.70) \times 10^{-17}\, e\,\mathrm{cm},$$
$$Im(d_\tau) = (-0.83 \pm 0.86) \times 10^{-17}\, e\,\mathrm{cm},$$

and the 95% confidence level limits was set to be

$$-2.2 < Re(d_\tau) < 4.5\ (10^{-17}\, e\,\mathrm{cm}),$$
$$-2.5 < Im(d_\tau) < 0.8\ (10^{-17}\, e\,\mathrm{cm}).$$

This investigation has successfully improved the sensitivity to the τ lepton's electric dipole moment by an order of magnitude over previous measurements. It is not only due to a 100 times larger statistics but also due to well-controlled systematic uncertainties.

Contents

Chapter 1

Introduction

The modern theory of particle physics, called the "Standard Model", was established with combining the electroweak theory proposed by Glashow, Weinberg and Salam in 1967 and the QCD theory developed in 1960s. Although the Standard Model (SM) has been able to solve many kinds of phenomena involving the elementary particles, recently evidence for neutrino oscillation has been found [1] and its effect requires the extention of the SM. Moreover, the existence of new physics phenomena beyond the SM (BSM) is anticipated in order to explain the present experimental phenomena more comprehensively and completely.

CP violation phenomena in the quark sector within the framework of the SM have been confirmed by B-factory experiments [2, 3] using neutral B meson decays. On the other hand, CP violation in the lepton sector has not been measured. The SM prediction is extremely small, since CP violation in the SM arises from a high-order loop correction with the quark current. However, many BSMs predict some large CP violation. Therefore, the CP violation effect in the lepton sector has been searched as a probe of BSM.

In this analysis, the electric dipole moment (EDM) of the τ lepton was measured using data corrected with the Belle detector at the KEKB collider at $\sqrt{s} = 10.58$ GeV. The EDM is a first-order approximation of the CP-violating parameter. One of the advantages of using the τ lepton is that the sensitivity for BSM could be highest, because the new gauge bosons in BSM strongly couple with heavy fermions, and the τ lepton is the heaviest lepton. Additionally, the decay configuration of the τ lepton is simpler than the quarks' reaction. Therefore, the τ lepton is a good experimental tool to search for BSM.

The KEKB/Belle experiment has brought about the highest luminosity in the world. The achieved peak luminosity is more than 8×10^{33} cm^{-2}s^{-1}, and the integrated luminosity per one year is expected to be more than 100 fb^{-1}. Our experiment produces τ pairs, as many as the B pairs, since the cross sections are 0.912 nb for $e^+e^- \to \tau^+\tau^-$ and 1.05 nb for $e^+e^- \to b\bar{b}$. Thus, KEKB is not only a "B" factory, but also a "τ" factory. Its very high statistics allows us a very precise measurement with the τ lepton.

Previous experimental measurements have been performed at LEP, where L3 [4] found $-3.1 < Re(d_\tau) < 3.1 \times 10^{-16} e\,\mathrm{cm}$ and OPAL [5] found $|Re(d_\tau)| < 3.7 \times 10^{-16} e\,\mathrm{cm}$, using the process $e^+e^- \to \tau^+\tau^-\gamma$, and at ARGUS [6], which set the limits $|Re(d_\tau)| < 4.6 \times 10^{-16} e\,\mathrm{cm}$ and $|Im(d_\tau)| < 1.8 \times 10^{-16} e\,\mathrm{cm}$ based on a study of $e^+e^- \to \tau^+\tau^-$ production. This analysis is the first direct measurement of the τ lepton's EDM with a sensitivity in the $10^{-17} e\,\mathrm{cm}$ range. Eight different final states in the decay of τ-pairs, $(e\nu\bar{\nu})(\mu\nu\bar{\nu})$, $(e\nu\bar{\nu})(\pi\nu)$, $(\mu\nu\bar{\nu})(\pi\nu)$, $(e\nu\bar{\nu})(\rho\nu)$, $(\mu\nu\bar{\nu})(\rho\nu)$, $(\pi\nu)(\rho\nu)$, $(\rho\nu)(\rho\bar{\nu})$, and $(\pi\nu)(\pi\bar{\nu})$, have been analyzed, where all particles except ν and $\bar{\nu}$ are positively or negatively charged.

The EDM can be measured using a CP-odd spin-momentum correlations of the τ pair reaction. In order to obtain the highest sensitivity for the EDM, an *optimal observable method* is adopted, which is formed using the matrix elements calculated by the measured kinematical information. In this thesis, the following will be described:

- Lagrangian with the electric-dipole-moment term
- Optimal observable method
- Introduction to the KEKB/Belle experiment
- Analysis and conclusion

Chapter 2

Electric Dipole Moment

2.1 P and T symmetries

Classically, the electric dipole moment (EDM) is given by

$$\boldsymbol{d} = \int \rho(r)\boldsymbol{r}d^3r, \tag{2.1}$$

where $\rho(\boldsymbol{r})$ is the electric charge density. If there is a structure of the charge distribution, the EDM becomes a non-zero value. Among the properties of elementary particles, the spacial direction is only characterized by the axis of the rotation symmetry, which is the spin, $\boldsymbol{S}$. Thus, the electric dipole moment $\boldsymbol{d}$ must be formed to be proportional to the spin as

$$\boldsymbol{d} = d\boldsymbol{S}, \tag{2.2}$$

where d is a constant representing the size of the EDM.

P (Parity) transformation changes a space cortinate. It changes the sign of the position vector $\boldsymbol{r}$ and momentum vector $\boldsymbol{p}$. Because the angular momentum $\boldsymbol{l}$ is defined as $\boldsymbol{l} \equiv \boldsymbol{r} \times \boldsymbol{p}$, the sign is not changed under P transformation. T transformation reflects the time. Therefore, it changes the sign of $\boldsymbol{p}$ and $\boldsymbol{l}$, while $\boldsymbol{r}$ is not changed. The transformation properties of the spin is the same with $\boldsymbol{l}$. Therefore, under a P and T transformations, the spin $\boldsymbol{S}$ is changed as $\boldsymbol{S} \to \boldsymbol{S}$ and $\boldsymbol{S} \to -\boldsymbol{S}$, respectively. On the other hand, because the P and T transformation properties of the EDM $\boldsymbol{d}$ are determined by the position $\boldsymbol{r}$ as shown in Eq.(2.1), $\boldsymbol{d}$ is changed as $\boldsymbol{d} \to -\boldsymbol{d}$ and $\boldsymbol{d} \to \boldsymbol{d}$ under the P and T transformation, respectively. Therefore, Eq.(2.2) violates both P and T symmetry. simultaneously. Thus if either P or T symmetry is required, d must vanish. Under CPT symmetry, Eq.(2.2) also violates CP symmetry. Table 2.1 summarize the change in the signs of $\boldsymbol{S}$ and $\boldsymbol{d}$ under P and T transformations with other fundamental variables.

2.2 Formalism

In this section, the theoretical calculations of the cross section and the matrix elements with the τ EDM effect for the process $e^+e^- \to \tau^+\tau^-$ are described.

Table 2.1: P and T transformation properties of the spin $\boldsymbol{S}$, the EDM $\boldsymbol{d}$ and other fundamental variables.

	P	T
Spin $\boldsymbol{S}$	$\boldsymbol{S}$	$-\boldsymbol{S}$
EDM $\boldsymbol{d}$	$-\boldsymbol{d}$	$\boldsymbol{d}$
Position $\boldsymbol{r}$	$-\boldsymbol{r}$	$\boldsymbol{r}$
Momentum $\boldsymbol{p}$	$-\boldsymbol{p}$	$-\boldsymbol{p}$
Angular Momentum $\boldsymbol{l}$	$\boldsymbol{l}$	$-\boldsymbol{l}$
Charge q	q	q
Electric field $\boldsymbol{E}$	$-\boldsymbol{E}$	$\boldsymbol{E}$
Magnetic field $\boldsymbol{B}$	$\boldsymbol{B}$	$-\boldsymbol{B}$

2.2.1 Lagrangian

The effective Lagrangian with the EDM term can be expressed as

$$\mathcal{L}_{\mathrm{eff}} = \mathcal{L}_{\mathrm{SM}} + \Delta\mathcal{L}, \tag{2.3}$$

$$\mathcal{L}_{\mathrm{SM}} = \bar{\psi}(i \not\partial - eQ \not A)\psi, \tag{2.4}$$

$$\begin{aligned} \Delta\mathcal{L} &= -ic\bar{\psi}\sigma^{\mu\nu}\gamma_5\psi\partial_\mu A_\nu + (h.c.), \\ &= -\frac{i}{2}\bar{\psi}\sigma^{\mu\nu}\gamma_5\psi d_\tau F_{\mu\nu}, \end{aligned} \tag{2.5}$$

where $d_\tau (\equiv c + c^*)$ is the electric dipole form-factor, A_μ is the electromagnetic vector potential and $F_{\mu\nu}$ is the electromagnetic field tensor given by $F^{\mu\nu} = \partial^\mu A^\nu - \partial^\nu A^\mu$. $\mathcal{L}_{\mathrm{SM}}$ is the Lagrangian for the lowest order Standard Model and $\Delta\mathcal{L}$ is the EDM term. Here, only the lowest-order gamma-exchange diagram and EDM contribution are considered, as shown in Figure 2.1; the Z^0 exchange diagram is ignored because the contribution of Z^0 is negligible at $\sqrt{s} = 10.58$ GeV. The electric dipole form-factor is often used in terms of the dimensionless dipole moment, $\tilde{a}_\tau$, given as

$$d_\tau = \frac{e}{2m_\tau}\tilde{a}_\tau. \tag{2.6}$$

The form-factor is a real number because $d_\tau \equiv c + c^*$. However, from the experimental point of view, the form-factor is generally treated as a complex number. The imaginary part of d_τ is the CPT-violating parameter, and for example, when the EDMs of the τ^+ and τ^- are different, the imaginary part of d_τ can arise effectively.

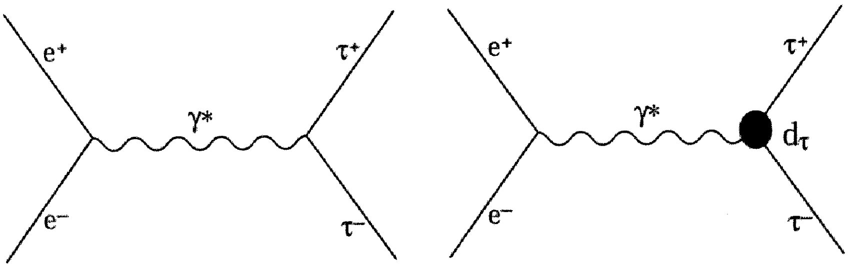

Figure 2.1: Diagrams for the lowest order(left) and the EDM interaction(right).

A part of the EDM term can be calculated as

$$\sigma^{0i}\gamma_5 F_{0i} = \sigma^{i0}\gamma_5 F_{i0} = -i\begin{pmatrix} \sigma^i & 0 \\ 0 & \sigma^i \end{pmatrix} E^i,$$

where E^i is the electric field and σ^i is the spin operator. At the non-relativistic limit, the EDM term is approximately expressed as

$$\Delta\mathcal{L} = -\frac{i}{2} d_\tau(q^2)\bar{\psi}\sigma^{\mu\nu}\gamma_5\psi F_{\mu\nu} \rightarrow -d_\tau(0)\boldsymbol{\sigma}\cdot\boldsymbol{E}.$$

Hence, the Lagrangian, $\Delta\mathcal{L}$, surely represents the EDM interaction.

In this analysis, the possible s-dependence is ignored in common with other experiments, while assuming $d_\tau(s) \equiv d_\tau$, which is constant. $d_\tau(0)$ corresponds to the *"Electric Dipole Moment"* of the τ lepton, and this term is used for d_τ hereafter.

2.2.2 Factorization

The differential cross section for the process

$$e^+(\boldsymbol{p}) + e^-(-\boldsymbol{p}) \rightarrow \tau^+(\boldsymbol{k}, \boldsymbol{S}_+) + \tau^-(-\boldsymbol{k}, \boldsymbol{S}_-),$$

can be written as [7, 8]

$$d\sigma = \mathcal{A}^2_{\text{prod}}(1 + a_\mu S^\mu_+ + b_\mu S^\mu_- + c_{\mu\nu}S^\mu_+ S^\nu_-)dQ, \tag{2.7}$$

where $\boldsymbol{p}$ and $\boldsymbol{k}$ are the momenta for the electron and τ, $\boldsymbol{S}_\pm$ is the spin vector of the $\tau^\pm$; $a_\mu, b_\mu, c_{\mu\nu}$ are the coefficients as a function of p and k, and $\mathcal{A}^2_{\text{prod}}$ is the spin-averaged squared matrix element for the τ pair production vertex. dQ is the Lorentz-invariant phase space factor. On the other hand, the differential partial width for the τ decay is given in this representation by

$$d\Gamma = \frac{1}{2m_\tau}\bar{\mathcal{A}}^2(1 + h_\mu S^\mu)dQ, \tag{2.8}$$

where the polarimeter vector, h_μ, is a function of the momenta of the τ and the decay particles. The zero-th element is defined to be $h_0 = 0$.

The cross section for the combined production and decay processes can be written as

$$d\sigma = \mathcal{A}^2_{\text{prod}}\bar{\mathcal{A}}^2\bar{\mathcal{A}}'^2(1 - a_\mu h^\mu_+ - b_\mu h^\mu_- + c_{\mu\nu}h^\mu_+ h^\nu_-)dQ. \tag{2.9}$$

Thus, the cross section of the τ reaction can be factorized to the production part and the decay part. These functions are connected with the τ's spin vectors.

2.2.3 τ pair production vertex

Here, the spin amplitudes of the reaction

$$e^-(p, \lambda) + e^+(\bar{p}, \bar{\lambda}) \rightarrow \tau^-(k, \sigma) + \tau^+(\bar{k}, \bar{\sigma})$$

is calculated where $p, \bar{p}, k$ and $\bar{k}$ denote the 4-momenta and $\lambda, \bar{\lambda}, \sigma$ and $\bar{\sigma}$ denote the helicities for the initial electrons and the produced τs. The "bar" indicates the respective antiparticles. The helicities are represented by "+" and "−" for the left-handed and right-handed particles. In this calculation, the electron mass is neglected.

In the following, the coordinate system defined in Figure 2.2 is used, which is the center-of-mass system with the z-axis parallel to the τ^- momentum-vector and the angle θ is between the τ^- and e^- momentum-vectors, in order to make the calculation simple. The Weyl-basis conventions is used, which is defined in HELAS [9, 10] / MadGraph [11]. The 4-momenta are therefore defined as follows:

$$\begin{aligned}
p^\mu &= E(1, -\sin\theta, 0, \cos\theta), \\
\bar{p}^\mu &= E(1, \sin\theta, 0, -\cos\theta), \\
k^\mu &= E(1, 0, 0, \beta), \\
\bar{k}^\mu &= E(1, 0, 0, -\beta).
\end{aligned}$$

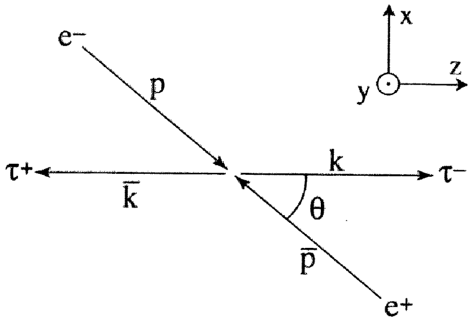

Figure 2.2: Coordinate system.

From the effective Lagrangian, Eq.(2.3)-(2.5), the spin-dependent amplitudes are written as

$$i\mathcal{M} = -ieQ_e(j_{L\mu} + j_{R\mu})\frac{-i}{s}[-ieQ_\tau(J_L^\mu + J_R^\mu) - i\frac{e}{2m_\tau}\tilde{a}_\tau J_{\tilde{a}}^\mu], \qquad (2.10)$$

where Q_e and Q_τ are the charge of an electron and τ ($Q_e = -1$ $Q_\tau = -1$). s is the squared center-of-mass energy ($\sqrt{s} = 2E$); m is the τ mass, m_τ. The charged currents are defined as follows:

$$j_L^\mu = \bar{v}(\bar{p}, \bar{\lambda} = +)\gamma^\mu \frac{1-\gamma_5}{2} u(p, \lambda = -), \qquad (2.11)$$

$$j_R^\mu = \bar{v}(\bar{p}, \bar{\lambda} = -)\gamma^\mu \frac{1+\gamma_5}{2} u(p, \lambda = +), \qquad (2.12)$$

$$J_L^\mu = \bar{u}(k, \sigma)\gamma^\mu \frac{1-\gamma_5}{2} v(\bar{k}, \bar{\sigma}), \qquad (2.13)$$

$$J_R^\mu = \bar{u}(k, \sigma)\gamma^\mu \frac{1+\gamma_5}{2} v(\bar{k}, \bar{\sigma}), \qquad (2.14)$$

$$J_a^\mu = -i\bar{u}(k, \sigma)\sigma^{\mu\nu} q_\nu v(\bar{k}, \bar{\sigma}), \qquad (2.15)$$

$$J_{\tilde{a}}^\mu = -\bar{u}(k, \sigma)\sigma^{\mu\nu} q_\nu v(\bar{k}, \bar{\sigma}). \qquad (2.16)$$

q_ν is the 4-momentum of the internal gamma, defined as $q_\nu = (\sqrt{s}, 0, 0, 0)$ in this coordinate system.

Then, the spin-dependent amplitudes, $\mathcal{M}(\lambda\bar{\lambda}\sigma\bar{\sigma})$, are obtained as:

$$\mathcal{M}(+-++) = \frac{e^2}{s}[-4Em\sin\theta] + \frac{-e^2}{2m_\tau s}\tilde{a}_\tau[8iE^3\beta\sin\theta],$$

$$
\begin{aligned}
\mathcal{M}(+-+-) &= \frac{e^2}{s}[-4E^2(1+\cos\theta)], \\
\mathcal{M}(+--+) &= \frac{e^2}{s}[4E^2(1-\cos\theta)], \\
\mathcal{M}(+---) &= \frac{e^2}{s}[4Em\sin\theta] + \frac{-e^2}{2m_\tau s}\tilde{a}_\tau[8iE^3\beta\sin\theta], \\
\mathcal{M}(-+++) &= \frac{e^2}{s}[-4Em\sin\theta] + \frac{-e^2}{2m_\tau s}\tilde{a}_\tau[8iE^3\beta\sin\theta], \\
\mathcal{M}(-++-) &= \frac{e^2}{s}[4E^2(1-\cos\theta)], \\
\mathcal{M}(-+-+) &= \frac{e^2}{s}[-4E^2(1+\cos\theta)], \\
\mathcal{M}(-+--) &= \frac{e^2}{s}[4Em\sin\theta] + \frac{-e^2}{2m_\tau s}\tilde{a}_\tau[8iE^3\beta\sin\theta].
\end{aligned}
$$

The first term in each amplitude shows the lowest-order coupling and the second term shows the interference term of the lowest order and the EDM coupling. The EDM terms appear in the amplitude of the $(\sigma\bar{\sigma}) = (++)$ and $(--)$ states, while the $(\sigma\bar{\sigma}) = (+-)$ and $(-+)$ states are independent of the EDM. Schematic views of these spin states are shown in Figures 2.3 and 2.4. It indicates that the EDM coupling affects the interaction between the left-handed and right-handed τ lepton. The interference of the diagrams shown in Figure 2.3 and 2.4 causes a first-order CP-violating effect.

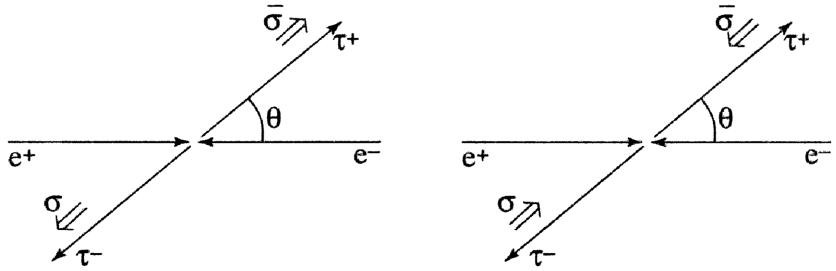

Figure 2.3: Spin states that induce the electric dipole moment.

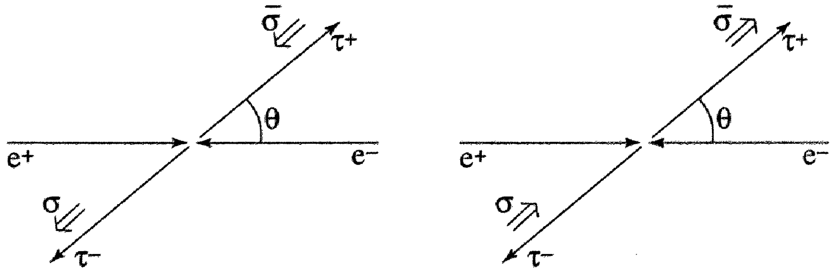

Figure 2.4: Spin states that are independent of the electric dipole moment.

To calculate the amplitudes from the experimental observables, it is convenient to transfer the spin amplitudes from the bispinor indices to the spin-vector notation. The spin vectors are given by the τ direction and the momenta of the decay daughters. The spin-density matrix, $\mathcal{M}$, of the reaction $e^+(\boldsymbol{p})e^-(-\boldsymbol{p}) \to \tau^+(\boldsymbol{k}, \boldsymbol{S}_+)\tau^-(-\boldsymbol{k}, \boldsymbol{S}_-)$ is given by [12]

$$
\begin{aligned}
\mathcal{M}^2_{\text{prod}} &= \mathcal{M}^2_{\text{SM}} + Re(d_\tau)\mathcal{M}^2_{Re} + Im(d_\tau)\mathcal{M}^2_{Im} + |d_\tau|^2\mathcal{M}^2_{d^2}, && (2.17)\\
\mathcal{M}^2_{\text{SM}} &= \frac{e^4}{k_0^2}[k_0^2 + m_\tau^2 + |\boldsymbol{k}^2|(\hat{\boldsymbol{k}}\cdot\hat{\boldsymbol{p}})^2 - \boldsymbol{S}_+\cdot\boldsymbol{S}_-|\boldsymbol{k}|^2(1 - (\hat{\boldsymbol{k}}\cdot\hat{\boldsymbol{p}})^2) \\
&\quad +2(\hat{\boldsymbol{k}}\cdot\boldsymbol{S}_+)(\hat{\boldsymbol{k}}\cdot\boldsymbol{S}_-)(|\boldsymbol{k}|^2 + (k_0 - m_\tau)^2(\hat{\boldsymbol{k}}\cdot\hat{\boldsymbol{p}})^2) + 2k_0^2(\hat{\boldsymbol{p}}\cdot\boldsymbol{S}_+)(\hat{\boldsymbol{p}}\cdot\boldsymbol{S}_-) \\
&\quad -2k_0(k_0 - m_\tau)(\hat{\boldsymbol{k}}\cdot\hat{\boldsymbol{p}})((\hat{\boldsymbol{k}}\cdot\boldsymbol{S}_+)(\hat{\boldsymbol{p}}\cdot\boldsymbol{S}_-) + (\hat{\boldsymbol{k}}\cdot\boldsymbol{S}_-)(\hat{\boldsymbol{p}}\cdot\boldsymbol{S}_+))], && (2.18)\\
\mathcal{M}^2_{Re} &= 4\frac{e^3}{k_0}|\boldsymbol{k}|[\ -(m_\tau + (k_0 - m_\tau)(\hat{\boldsymbol{k}}\cdot\hat{\boldsymbol{p}})^2)(\boldsymbol{S}_+ \times \boldsymbol{S}_-)\cdot\hat{\boldsymbol{k}} \\
&\qquad + k_0(\hat{\boldsymbol{k}}\cdot\hat{\boldsymbol{p}})(\boldsymbol{S}_+ \times \boldsymbol{S}_-)\cdot\hat{\boldsymbol{p}}\ ], && (2.19)\\
\mathcal{M}^2_{Im} &= 4\frac{e^3}{k_0}|\boldsymbol{k}|[\ -(m_\tau + (k_0 - m_\tau)(\hat{\boldsymbol{k}}\cdot\hat{\boldsymbol{p}})^2)(\boldsymbol{S}_+ - \boldsymbol{S}_-)\cdot\hat{\boldsymbol{k}} \\
&\qquad + k_0(\hat{\boldsymbol{k}}\cdot\hat{\boldsymbol{p}})(\boldsymbol{S}_+ - \boldsymbol{S}_-)\cdot\hat{\boldsymbol{p}}\ ], && (2.20)\\
\mathcal{M}^2_{d^2} &= 4e^2|\boldsymbol{k}|^2\cdot\ (1 - (\hat{\boldsymbol{k}}\cdot\hat{\boldsymbol{p}})^2)(1 - \boldsymbol{S}_+\cdot\boldsymbol{S}_-), && (2.21)
\end{aligned}
$$

where k_0 is the energy of the τ, m_τ is the τ mass, $\boldsymbol{p}$ is the three-momentum of the e^+, $\boldsymbol{k}$ is the three-momentum of the τ^+, $\boldsymbol{S}_\pm$ are the spin vectors for $\tau^\pm$, and hat denotes a unit momentum. $\mathcal{M}^2_{\text{SM}}$ corresponds to the SM term. $\mathcal{M}^2_{Re}$ and $\mathcal{M}^2_{Im}$ are interference terms (related to the real and imaginary parts of d_τ, respectively) between the SM and CPV amplitudes.

Concerning the components of the spin-momentum correlation, the following expressions are obtained for the CP and T transformation:

$$
\begin{aligned}
\mathcal{CP}\,((\boldsymbol{S}_+ \times \boldsymbol{S}_-)\cdot\boldsymbol{k}_+) &= (\boldsymbol{S}_- \times \boldsymbol{S}_+)\cdot(-\boldsymbol{k}_-) = -(\boldsymbol{S}_+ \times \boldsymbol{S}_-)\cdot\boldsymbol{k}_+,\\
\mathcal{CP}\,((\boldsymbol{S}_+ - \boldsymbol{S}_-)\cdot\boldsymbol{k}_+) &= (\boldsymbol{S}_- - \boldsymbol{S}_+)\cdot(-\boldsymbol{k}_-) = -(\boldsymbol{S}_+ - \boldsymbol{S}_-)\cdot\boldsymbol{k}_+.
\end{aligned}
$$

$$
\begin{aligned}
\mathcal{T}\,((\boldsymbol{S}_+ \times \boldsymbol{S}_-)\cdot\boldsymbol{k}_+) &= ((-\boldsymbol{S}_+) \times (-\boldsymbol{S}_-))\cdot(-\boldsymbol{k}_+) = -(\boldsymbol{S}_+ \times \boldsymbol{S}_-)\cdot\boldsymbol{k}_+,\\
\mathcal{T}\,((\boldsymbol{S}_+ - \boldsymbol{S}_-)\cdot\boldsymbol{k}_+) &= ((-\boldsymbol{S}_+) - (-\boldsymbol{S}_-))\cdot(-\boldsymbol{k}_+) = \ \ (\boldsymbol{S}_+ - \boldsymbol{S}_-)\cdot\boldsymbol{k}_+.
\end{aligned}
$$

The same expressions are given for $\boldsymbol{p}_\pm$ instead of $\boldsymbol{k}_\pm$. Therefore, $\mathcal{M}^2_{Re}$ show the CP-odd and T-odd property, while $\mathcal{M}^2_{Im}$ show the CP-odd and T-even. These properties also mean that the EDM is the CP-violating parameter. Moreover, the EDM for the imaginary part is the CPT-violating parameter.

Figures 2.5 and 2.6 show the spin-momentum correlations for $(\boldsymbol{S}_+ \times \boldsymbol{S}_-)\cdot\boldsymbol{k}$ and $(\boldsymbol{S}_+ - \boldsymbol{S}_-)\cdot\boldsymbol{k}$, respectively. The sign of $(\boldsymbol{S}_+ \times \boldsymbol{S}_-)\cdot\boldsymbol{k}$ depends on the transverse spin correlation to $\boldsymbol{k}$, while the sign of $(\boldsymbol{S}_+ - \boldsymbol{S}_-)\cdot\boldsymbol{k}$ depends on the longitudinal spin correlation. Therefore, the EDM for the real part causes the angular asymmetry around the $\boldsymbol{k}$ and $\boldsymbol{p}$, and the EDM for the imaginary part causes the asymmetry along the $\boldsymbol{k}$ and $\boldsymbol{p}$, as shown in the left side of each figure.

2.3 Experimental results

The EDM of the τ lepton was measured at the LEP and ARGUS experiments. At LEP, two experimental groups, L3 and OPAL, reported the bound of the EDM using the radiative τ-pair process $e^+e^- \to \tau^+\tau^-\gamma$ at Z^0 resonance. The EDM was extracted using the likelihood

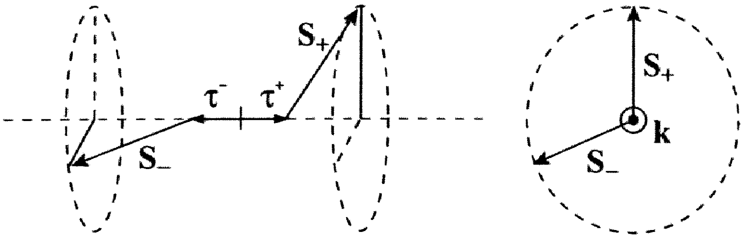

Figure 2.5: Configuration of the spin correlation for $(\boldsymbol{S}_+ \times \boldsymbol{S}_-)\cdot\boldsymbol{k}$ related to $\mathcal{M}^2_{Re}$. The sign depends on the transverse spin correlation.

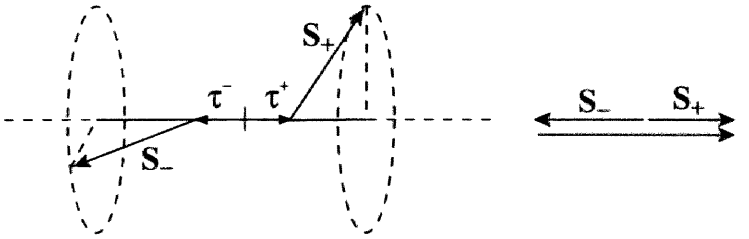

Figure 2.6: Configuration of the spin correlation for $(\boldsymbol{S}_+ - \boldsymbol{S}_-)\cdot\boldsymbol{k}$ related to $\mathcal{M}^2_{Im}$. The sign depends on the longitudinal spin correlation.

method from the momentum information of the radiated photon. L3 found $-3.1 < Re(d_\tau) < 3.1\times10^{-16}e\,\mathrm{cm}$ [4] and OPAL found $|Re(d_\tau)| < 3.7\times10^{-16}e\,\mathrm{cm}$ [5]. The ARGUS experiment adopted the optimal observable method using the event shape of the reaction $e^+e^- \to \tau^+\tau^-$, which is the same method in this thesis, and set the limits $|Re(d_\tau)| < 4.6\times10^{-16}e\,\mathrm{cm}$ and $|Im(d_\tau)| < 1.8\times10^{-16}e\,\mathrm{cm}$ [6].

The EDM properties for several particles were also measured. The current best EDM values and the Standard Model predictions are listed in Table 2.2. The non-zero EDM has not been observed. The basic method for the EDM measurements of the electron, neutron and proton is to measure a shift of the resonance using the NMR technique with the electric field which make a energy shift due to the interaction with EDM. The electron EDM was extracted using atomic-beam magnetic resonance of the atomic thallium [38], because in heavy paramagnetic atoms the electron EDM results in an atomic EDM enhanced by some factor due to relativistic effect. The proton EDM was also extracted from a shift of the thallium spin resonance in the electric field [41]. The neutron EDM was measured by a shift of the Larmor frequency of ultra-cold neutrons, whose energy is a order of 10^{-7}eV, in a electric field parallel to a highly uniform $1\mu T$ magnetic field [40]. The muon EDM was measured by the vertical spin motion in the muon storage ring [39]. The spin direction was detected by the electron direction decaying from the muon.

2.4 Models

Here, models that are considered to induce the effect on the electric dipole moment of the τ lepton are briefly described.

Standard Model

In the current Standard Model, the CP-violation effect in the lepton sector arises from a three-loop QCD correction. Its origin is the CP phase of the CKM matrix. The EDM of

Table 2.2: Experimental results and the Standard Model (SM) predictions of the EDMs for the electron, muon, neutron and proton.

	EDM ($e$cm)	SM prediction ($e$cm)
electron	$(6.9 \pm 7.4) \times 10^{-28}$ [38]	$\sim 8 \times 10^{-41}$ [13, 14]
muon	$(3.7 \pm 3.4) \times 10^{-19}$ [39]	$\sim 1.6 \times 10^{-38}$ [13, 14]
neutron	$(-1.0 \pm 3.6) \times 10^{-26}$ [40]	$1.4 \times 10^{-33} \sim 1.6 \times 10^{-31}$ [42]
proton	$(-3.7 \pm 6.3) \times 10^{-23}$ [41]	—

the lepton is given by

$$d_l \sim 1.6(m_l/\mathrm{MeV}) \times 10^{-40} e\,\mathrm{cm},$$

where m_l is the mass of the lepton [13, 14]. For the τ lepton, the EDM is expected as $d_\tau \sim 3 \times 10^{-37} e\,\mathrm{cm}$.

By comparing the limit of the current experiments, it is found to be too small to observe. Therefore, an observation of a non-zero EDM would indicate new physics beyond the Standard Model.

Neutrino oscillation

Recently, some neutrino-oscillation experiments have reported that neutrinos are massive and their flavor oscillates [1]. Lepton flavor mixing causes anomalous lepton dipole moments and the lepton flavor-violating decays. However, even if neutrino oscillation exists, the contribution to the anomalous dipole moments is very small. With the lepton-flavor mixing matrix, whose parameter space is obtained from the experimental results, the EDM of the τ lepton is estimated to be $d_\tau \sim 10^{-25} e\,\mathrm{cm}$ using the effective Lagrangian approach [15]. The source of the CP-violating effect is the CP phase in the lepton mixing matrix.

Multi-Higgs-doublet model

In the case of the two- or multi-Higgs-doublet models, the CP violation is generated by the interference of the tree-level production process, $e^+e^- \to \gamma, X \to \tau^+\tau^-$, where X is some new Higgs boson. The strength of the interference term is proportional to the initial and the final state fermion masses $m_e m_\tau$. Because of the small electron mass m_e, it is hopeless to search for CP violation from the tree-level production process [19].

In the Higgs models containing neutral spin-0 bosons, which may couple to leptons through lepton-flavor-conserving scalar and pseudoscalar couplings, the strength of the EDM is proportional to m_l^3 [16]. Using the present limit of the electron EDM, $d_e < (6.9 \pm 9.4) \times 10^{-28} e\,\mathrm{cm}$, the τ EDM on the order of $10^{-17} e\,\mathrm{cm}$ is possible.

In other Multi-Higgs-doublet models [17, 18], the EDM arises through two-loop diagrams with the neutral Higgs bosons and the top-quark loop. The CP violation is arise from the propagator of the neutral Higgs bosons. Because of the coupling constant of Higgs bosons to fermions, the EDM is proportional to the fermion mass, m_f. In this case, d_τ is estimated to be $d_\tau < 4 \times 10^{-21} e\,\mathrm{cm}$ [19].

SUSY model

τ-$\tilde{\tau}$-neutralino coupling may contain the CP phase and generate a non-zero EDM in one loop diagram, such as in Figure 2.7. The contribution to d_l from these diagram is proportional to left-handed and right-handed slepton mixing matrices. In the popular MSSM predictions, its coupling is proportional to the fermion mass [19]. Considering the limit of the electron EDM, the τ EDM must be less than $4 \times 10^{-23} e\,\mathrm{cm}$. However, in the generic MSSM model, the constraint of the parameters in the above estimation is not necessarily true. Under the particular parameter set, the τ EDM can be larger than $10^{-22} e\,\mathrm{cm}$. In this case, a model [19] predicts that $d_\tau \simeq 10^{-19} e\,\mathrm{cm}$.

Leptoquark model

The couplings of the leptoquark boson to the τ lepton and the top quark may generate the CP-violation effect at the one-loop level. In the scalar leptoquark doublet model [20], which assumed that the couplings of the scalar leptoquarks are of the Higgs boson type, the couplings of the leptoquarks would be proportional to the mass of the right-handed fermion involved. Furthermore, the generation-changing couplings are assumed to be small. In this case, because the corresponding quark is coupled with leptoquark on the loop diagram, the EDMs of the leptons are scaled by the following relation:

$$d_e : d_\mu : d_\tau = m_u^2 m_e : m_c^2 m_\mu : m_t^2 m_\tau .$$

Therefore, the τ EDM can have a larger value of $10^{-19} e\,\mathrm{cm}$ with a restriction of the electron EDM.

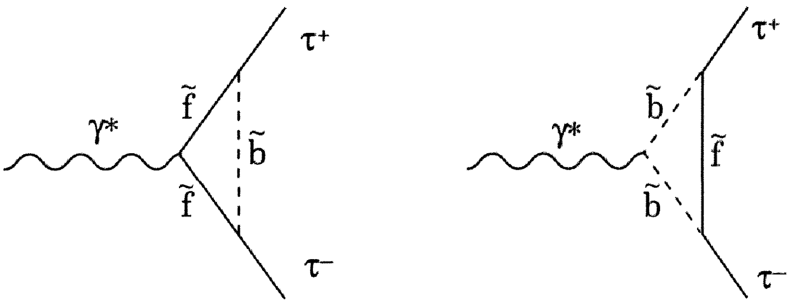

Figure 2.7: One-loop diagrams that may induce an electric dipole moment. "f̃" and "b̃" show new fermions and bosons of a model, respectively.

Chapter 3

Observable

In this analysis, the 'optimal observable method' [21][22] is used in order to obtain the highest sensitivity for d_τ. The observables are calculated for the reaction $e^+e^- \to \tau^+\tau^-$ with a combination of the decays, $\tau \to e\nu\bar{\nu}$, $\tau \to \mu\nu\bar{\nu}$, $\tau \to \pi\nu$ and $\tau \to \rho\nu$, which cover about 72% of all possible τ decays.

3.1 Optimal observable

To search for CP violation in the reaction $e^+e^- \to \tau^+\tau^-$, CP-odd observables are proposed in Ref. [12], such as

$$
\begin{aligned}
T^{ij} &= (q_+ - q_-)^i (q_+ \times q_-)^j + (i \leftrightarrow j), \\
Q^{ij} &= (q_+ + q_-)^i (q_+ - q_-)^j - \frac{\delta^{ij}}{3}(q_+^2 - q_-^2) + (i \leftrightarrow j),
\end{aligned}
$$

where $q_\pm$ shows the momentum of the charged particle from the $\tau^\pm$ decay and $i, j = 1...3$ are Cartesian vector indices. The CP-odd optimal observables are formed based on all experimentally available information in a statistically optimal way. These observables use the combined information of the CP-odd observables, such as T^{ij} and Q^{ij}, which use only part of the kinematical information.

The optimal observable, $\mathcal{O}$, is derived to yield the largest possible signal-to-noise ratio, defined by

$$S \equiv \sqrt{\frac{\langle \mathcal{O} \rangle^2}{\langle \mathcal{O}^2 \rangle - \langle \mathcal{O} \rangle^2}}.$$

For the case that the differential cross section is given by

$$d\sigma = d\sigma_0 + \lambda d\sigma_1,$$

where λ is a small parameter which we want to measure, the optimal observable is formed as

$$\mathcal{O} = \frac{d\sigma_1}{d\sigma_0}.$$

The proof is described in Appendix A.

The sensitivity of the optimal observable is ideally the same as that for the likelihood method. Moreover, since this optimal observable is a kind of moment, the analysis procedure is simple compared to that of the likelihood method.

3.2 Observables for EDM

The matrix elements for the production of a τ pair $\mathcal{M}_{\text{prod}}$ and the τ decay $\mathcal{M}_{\text{dec}}$ can be factorized using the Born approximation as $\mathcal{M}^2 = \mathcal{M}^2_{\text{prod}} \cdot \mathcal{M}^2_{\text{dec}}$, so that the optimal observables in this analysis are formed as

$$\mathcal{O}_{Re} = \frac{\mathcal{M}^2_{Re}}{\mathcal{M}^2_{\text{SM}}}, \quad \mathcal{O}_{Im} = \frac{\mathcal{M}^2_{Im}}{\mathcal{M}^2_{\text{SM}}}, \tag{3.1}$$

where the matrix elements $\mathcal{M}^2_{\text{SM}}$, $\mathcal{M}^2_{Re}$ and $\mathcal{M}^2_{Im}$ are defined in Eq.(2.18), (2.19) and (2.20), respectively, and are calculated event-by-event, as described later. Because of the properties of the matrix elements, $\mathcal{O}_{Re}$ is CP-odd and T-odd, while $\mathcal{O}_{Im}$ is CP-odd and T-even.

Using the squared matrix element $\mathcal{M}^2_{\text{prod}}$, the differential cross section, $d\sigma$, is given as $d\sigma \propto \mathcal{M}^2_{\text{prod}} d\phi$, where ϕ represents a phase-space variable. The mean value of the observable $\mathcal{O}_{Re}$ is expressed as

$$\begin{aligned}
\langle \mathcal{O}_{Re} \rangle &\propto \int \mathcal{O}_{Re} d\sigma \propto \int \mathcal{O}_{Re} \mathcal{M}^2_{\text{prod}} d\phi, \\
&= \int \frac{\mathcal{M}^2_{Re}}{\mathcal{M}^2_{\text{SM}}} (\mathcal{M}^2_{\text{SM}} + Re(d_\tau)\mathcal{M}^2_{Re} + Im(d_\tau)\mathcal{M}^2_{Im} + |d_\tau|^2 \mathcal{M}^2_{d^2})\, d\phi, \\
&= \int \mathcal{M}^2_{Re} d\phi + Re(d_\tau) \int \frac{(\mathcal{M}^2_{Re})^2}{\mathcal{M}^2_{\text{SM}}} d\phi \\
&\quad + Im(d_\tau) \int \frac{\mathcal{M}^2_{Re}\mathcal{M}^2_{Im}}{\mathcal{M}^2_{\text{SM}}} d\phi + |d_\tau|^2 \int \frac{\mathcal{M}^2_{Re}\mathcal{M}^2_{d^2}}{\mathcal{M}^2_{\text{SM}}} d\phi.
\end{aligned} \tag{3.2}$$

The third term, the integration for the cross term of $\mathcal{M}^2_{Re}$ and $\mathcal{M}^2_{Im}$, drops out because they are orthogonal. The fourth term, which includes $\mathcal{M}^2_{d^2}$, is disregarded, since d_τ is small. Similar expressions are obtained for the imaginary part. From Eq.(3.2), $\langle \mathcal{O}_{Re} \rangle$ and $\langle \mathcal{O}_{Im} \rangle$ are then approximately given by linear functions of d_τ:

$$\langle \mathcal{O}_{Re} \rangle = a_{Re} \cdot Re(d_\tau) + b_{Re}, \quad \langle \mathcal{O}_{Im} \rangle = a_{Im} \cdot Im(d_\tau) + b_{Im}. \tag{3.3}$$

Here, a_{Re} and a_{Im} express the sensitivity for $Re(d_\tau)$ and $Im(d_\tau)$, respectively; b_{Re} and b_{Im} provide offsets. Because the coefficients are expressed as

$$\int \frac{(\mathcal{M}^2_{Re})^2}{\mathcal{M}^2_{\text{SM}}} d\phi \simeq \int \left(\frac{\mathcal{M}^2_{Re}}{\mathcal{M}^2_{\text{SM}}}\right)^2 \mathcal{M}^2_{\text{prod}} d\phi, \quad \int \frac{(\mathcal{M}^2_{Im})^2}{\mathcal{M}^2_{\text{SM}}} d\phi \simeq \int \left(\frac{\mathcal{M}^2_{Im}}{\mathcal{M}^2_{\text{SM}}}\right)^2 \mathcal{M}^2_{\text{prod}} d\phi,$$

a_{Re} and a_{Im} are given by the mean of the squared observable, $a_{Re} = \langle \mathcal{O}^2_{Re} \rangle$ and $a_{Im} = \langle \mathcal{O}^2_{Im} \rangle$. Because of the CP-odd properties of $\mathcal{M}^2_{Re}$ and $\mathcal{M}^2_{Im}$. the offsets b_{Re} and b_{Im} should be null for a symmetric acceptance cut.

By using Eq.(3.3), the EDMs, $Re(d_\tau)$ and $Im(d_\tau)$, can be extracted from $\langle \mathcal{O}_{Re} \rangle$ and $\langle \mathcal{O}_{Im} \rangle$.

3.3 Calculation of the observables

The observables are calculated with the matrix elements defined in Eq.(2.18) - (2.20), which are expressed by the e^+ beam direction $\hat{\boldsymbol{p}}$, the τ^+ flight direction $\hat{\boldsymbol{k}}$ and the spin vectors, $\boldsymbol{S}_\pm$. Experimentally, because of undetectable particles, i.e. neutrinos, we can not fully reconstruct the quantities $\hat{k}$ and $S_\pm$. Therefore, the deduced observables are used in the analysis, which is calculated using the mean value of $\mathcal{M}^2_{\rm SM}$, $\mathcal{M}^2_{Re}$ and $\mathcal{M}^2_{Im}$ averaging over the possible kinematic configurations for each event. How to calculate the possible τ directions, the spin vectors and the mean value of the matrix elements is described below.

3.3.1 Tau flight direction

Since the allowed kinematical range is largely different between hadronic decay and leptonic decay, the average is calculated in three individual cases:

hadron-hadron: Both τ leptons decay to hadrons.

lepton-hadron: One τ lepton decays leptonically and the other decays to hadrons.

lepton-lepton: Both τ leptons decay leptonically.

hadron-hadron

For hadronic decay, the flight direction of the mother τ lepton is constrained on the cone around the flight direction of the decay daughter particle. The opening angle, $\theta_{\rm cone}$, is calculated while neglecting the neutrino mass as

$$\cos\theta_{\rm cone} = \frac{2E_\tau E - m^2 - m_\tau^2}{2|\boldsymbol{k}||\boldsymbol{p}|}, \tag{3.4}$$

where E, $\boldsymbol{p}$ and m are the measured energy, momentum and mass of the decay daughter. Therefore, in the case that both τ leptons decay hadronically, the τ flight direction can be reconstructed as the intersections of two cones, as shown in Figure 3.1.

For the reaction $e^+e^- \to \tau^+(\boldsymbol{k})\tau^-(-\boldsymbol{k}) \to A^+(\boldsymbol{p}_A)B^-(\boldsymbol{p}_B)\nu_\tau\bar{\nu}_\tau$ in the τ pair rest frame, two solutions of the τ^+ flight direction, $\hat{\boldsymbol{k}}$, can be calculated as

$$\hat{\boldsymbol{k}}_\pm = u\hat{\boldsymbol{p}}_A + v\hat{\boldsymbol{p}}_B \pm w\frac{\hat{\boldsymbol{p}}_A \times \hat{\boldsymbol{p}}_B}{|\hat{\boldsymbol{p}}_A \times \hat{\boldsymbol{p}}_B|}, \tag{3.5}$$

where $\boldsymbol{p}_A$ and $\boldsymbol{p}_B$ are the three-momentum vectors of the decay products A^+ and B^-, respectively. The hats denote unit momenta. Using the definitions

$$\hat{\boldsymbol{k}}\hat{\boldsymbol{p}}_A = \cos\theta_A, \quad \hat{\boldsymbol{k}}\hat{\boldsymbol{p}}_B = \cos\theta_B,$$

where θ_A and θ_B show the open angles of the cones for A^+ and B^-, the coefficients u, v and w are represented as

$$u = \frac{\cos\theta_A + \hat{\boldsymbol{p}}_A\hat{\boldsymbol{p}}_B\cos\theta_B}{1-(\hat{\boldsymbol{p}}_A\hat{\boldsymbol{p}}_B)^2}, \tag{3.6}$$

$$v = \frac{\cos\theta_B + \hat{\boldsymbol{p}}_A\hat{\boldsymbol{p}}_B\cos\theta_A}{1-(\hat{\boldsymbol{p}}_A\hat{\boldsymbol{p}}_B)^2}, \tag{3.7}$$

$$w = \sqrt{1-u^2-v^2-2uv(\hat{\boldsymbol{p}}_A\hat{\boldsymbol{p}}_B)}. \tag{3.8}$$

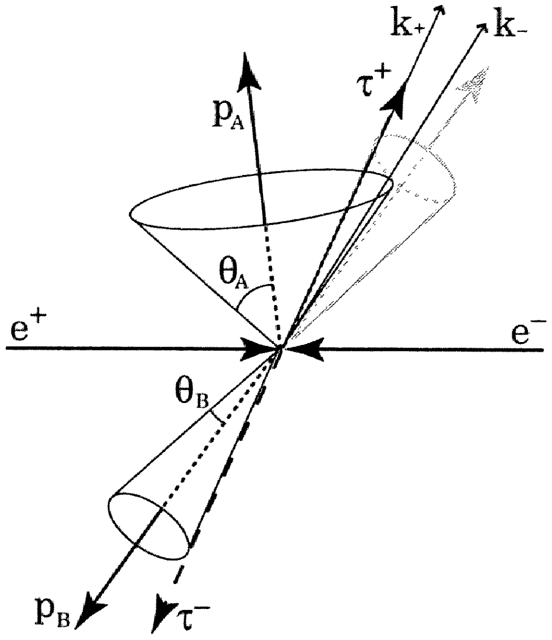

Figure 3.1: Schematic view of the τ pair reaction $e^+e^- \to \tau^+(k^+)\tau^-(k^-) \to A^+(p_A)B^-(p_B)\nu_\tau\bar{\nu}_\tau$. θ_A and θ_B are the opening angles between the τ momentum and the momentum of the decay products.

lepton-hadron

For the leptonic τ decay $\tau \to l\nu\bar{\nu}$, the opening angle, θ_l, between the measured lepton and the mother τ cannot be given as an unique solution due to two missing neutrinos. θ_l is thus given by

$$\cos\theta_l = \frac{2E_\tau E_l - m_l^2 - m_\tau^2 + m_{\nu\nu}^2}{2|\boldsymbol{k}||\boldsymbol{p}_l|}, \tag{3.9}$$

where $m_{\nu\nu}$ is the effective invariant mass of two daughter neutrinos, whose possible range is over $0 < m_{\nu\nu} < \sqrt{m_\tau^2 + m_l^2 - 2m_\tau m_l}$. Because of the $m_{\nu\nu}$ ambiguity, the kinematically allowed τ direction is widely ranged compared to the hadronic decay case, as illustrated in Figure 3.2.

lepton-lepton

For the lepton-lepton modes, there are ambiguities of $m_{\nu\nu}$ in both τ decays. The kinematically allowed region of $\boldsymbol{k}$ is an overlap domain of two cones. Their allowed θ_l range is the same as that in the lepton-hadron case.

Reconstructed Tau direction

Figure 3.3 shows the angle difference between the generated τ direction and the reconstructed one used in the calculation. The accuracy of the reconstructed τ direction in the hadronic decay modes is better than that in the leptonic modes. The long small tail in the $\pi\pi$ mode is due to an incorrect selection of the two $\hat{\boldsymbol{k}}_\pm$ directions.

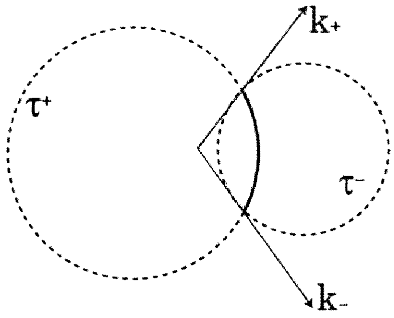

Figure 3.2: Projection view for the lepton-hadron final state. The solid curve shows the allowed region of the τ direction in the case that τ^+ decays hadronically and τ^- decays leptonically.

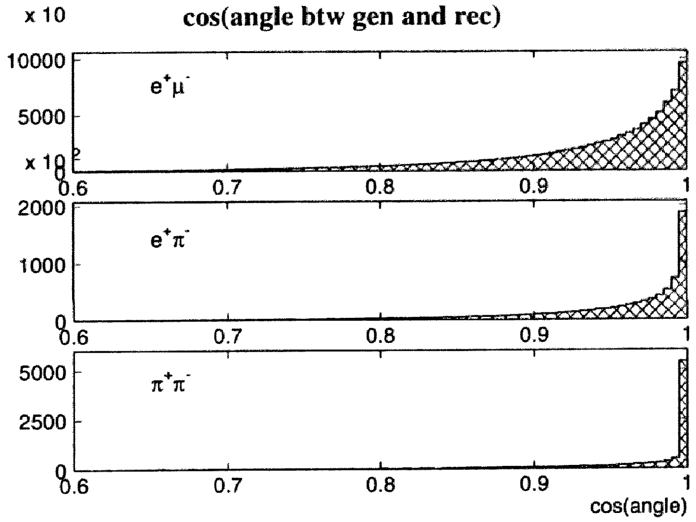

Figure 3.3: Cosine of the angle between the generated τ direction and the reconstructed direction used in the calculation for $e^+\mu^-$(top), $e^+\pi^-$(middle) and $\pi^+\pi^-$(bottom).

3.3.2 Spin vector

The spin vectors are calculated based on the measured momenta of the decay particles and the above-extracted tau flight direction. The following gives the polarimeter vectors $\boldsymbol{h}$ [8, 27], shown in Eq.(2.8) for different decay modes, where all momenta are defined in the τ rest frame:

- $\tau^\pm(k_\pm, S_\pm) \rightarrow l(p_{l^\pm})\nu_l(q_l)\nu_\tau(q_\tau)$

$$\boldsymbol{h}^\pm = \mp \frac{(4E'_l - m_l - \frac{3m_l^2}{m_\tau})/E'_l}{3m_l - 4E'_l - \frac{2m_l^2}{E'_l} + \frac{3m_l^2}{m_\tau}} \boldsymbol{p}'_{l\pm}, \tag{3.10}$$

- $\tau^{\pm}(k_{\pm}, \boldsymbol{S}_{\pm}) \to \pi(p_{\pi^{\pm}})\nu_{\tau}(q_{\tau})$

$$\boldsymbol{h}^{\pm} = \pm\frac{\boldsymbol{p}'_{\pi^{\pm}}}{|\boldsymbol{p}'_{\pi^{\pm}}|}, \tag{3.11}$$

- $\tau^{\pm}(k_{\pm}, \boldsymbol{S}_{\pm}) \to \pi(p_{\pi^{\pm}})\pi(p_{\pi^0})\nu_{\tau}(q_{\tau})$

$$\boldsymbol{h}^{\pm} = \pm m_{\tau}\frac{2(p' \cdot q'_{\tau})\boldsymbol{p}' - (p')^2\boldsymbol{q}'_{\tau}}{2(p' \cdot q'_{\tau})(p' \cdot k'_{\pm}) - (p')^2(q'_{\tau} \cdot k'_{\pm})}, \tag{3.12}$$

where $p = p_{\pi^{\pm}} - p_{\pi^0}$.

The momentum $\boldsymbol{p}'$ and energy E' in the τ rest frame are expressed in terms of their quantities in the τ pair rest frame, as follows:

$$\boldsymbol{p}' = \boldsymbol{p} + \frac{\gamma - 1}{\beta^2}(\boldsymbol{\beta} \cdot \boldsymbol{p})\boldsymbol{\beta} + \gamma E\boldsymbol{\beta}, \tag{3.13}$$

$$E' = \gamma(E + \boldsymbol{\beta} \cdot \boldsymbol{p}), \tag{3.14}$$

where $\boldsymbol{\beta} = -\boldsymbol{k}_{\pm}/E_{\tau}$, $\gamma = E_{\tau}/m_{\tau}$ and $\boldsymbol{k}_{\pm} = \pm\boldsymbol{k}$. $\boldsymbol{k}$ and E_{τ} are also defined in the τ pair rest frame. As a result, the spin vectors $\boldsymbol{S}$, defined as $\boldsymbol{S} \equiv -\boldsymbol{h}$, are given as follows from Eq.(2.7) and Eq.(2.9). In the equations, $k = (E_{\tau}, \boldsymbol{k})$ and the four momenta in the τ pair rest frame are used:

- $\tau \to l\nu_l\nu_{\tau}$

$$\boldsymbol{S}_{\pm} = \frac{4c_{\pm} - m_{\tau}^2 - 3m_l^2}{3m_{\tau}^2 c_{\pm} - 4c_{\pm}^2 - 2m_l^2 m_{\tau} + 3c_{\pm}m_l^2}\left(\pm m_{\tau}\boldsymbol{p}_{l^{\pm}} - \frac{c_{\pm} + E_{l^{\pm}}m_{\tau}}{E_{\tau} + m_{\tau}}\boldsymbol{k}\right), \tag{3.15}$$
$$c_{\pm} = E_{\tau}E_{l^{\pm}} \mp \boldsymbol{k} \cdot \boldsymbol{p}_{l^{\pm}},$$

- $\tau \to \pi\nu_{\tau}$

$$\boldsymbol{S}_{\pm} = \frac{2}{m_{\tau}^2 - m_{\pi}^2}\left(\mp m_{\tau}\boldsymbol{p}_{\pi^{\pm}} + \frac{m_{\tau}^2 + m_{\pi}^2 + 2m_{\tau}E_{\pi^{\pm}}}{2(E_{\tau} + m_{\tau})}\boldsymbol{k}\right), \tag{3.16}$$

- $\tau \to \rho\nu_{\tau} \to \pi\pi^0\nu_{\tau}$

$$\boldsymbol{S}_{\pm} = \mp\frac{1}{(k_{\pm}H_{\pm}) - m_{\tau}^2(p_{\pi^{\pm}} - p_{\pi^0})^2}\left(\mp H_0^{\pm}\boldsymbol{k} + m_{\tau}\boldsymbol{H}^{\pm} + \frac{\boldsymbol{k}(\boldsymbol{k} \cdot \boldsymbol{H}^{\pm})}{(E_{\tau} + m_{\tau})}\right), \tag{3.17}$$
$$(H^{\pm})^{\nu} = 2(p_{\pi^{\pm}} - p_{\pi^0})^{\nu}(p_{\pi^{\pm}} - p_{\pi^0})^{\mu}(k_{\pm})_{\mu} + (p_{\pi^{\pm}} + p_{\pi^0})^{\nu}(p_{\pi^{\pm}} - p_{\pi^0})^2,$$

3.3.3 Averaging the amplitudes

Now, the matrix elements $\mathcal{M}_{\rm SM}^2$, $\mathcal{M}_{Re}^2$ and $\mathcal{M}_{Im}^2$ can be calculated using the τ flight direction $\hat{\boldsymbol{k}}$ and the spin vectors $\boldsymbol{S}_{\pm}$. In the case that both τ leptons decay to hadrons ($\tau \to \pi\nu$ or $\rho\nu$), the τ flight direction is calculated with twofold ambiguity, as described above, and the average of $\mathcal{M}_{\rm SM}^2$, $\mathcal{M}_{Re}^2$ and $\mathcal{M}_{Im}^2$ over the two solutions. In the case where either one or both of the τ leptons decay leptonically ($\tau \to e\nu\bar{\nu}$ and $\mu\nu\bar{\nu}$), a Monte Carlo (MC) treatment is adopted to take into account the additional ambiguity in the effective mass of the $\nu\bar{\nu}$ system ($m_{\nu\bar{\nu}}$). For each event, 100 MC configurations are generated using a hit-and-miss approach by varying $m_{\nu\bar{\nu}}$. With $N_{\rm hit}$ successful tries, in which the τ direction can be construct kinematically, the average value is calculated as

$$\mathcal{M}^2 = \frac{1}{N_{\rm hit}}\sum_i^{N_{\rm hit}}\mathcal{M}_i^2. \tag{3.18}$$

In the calculation, the effect of undetected radiative photons is ignored, because much computing power is needed to include the additional ambiguity into the calculation. Its radiation effect is considered to be included in the conversion parameters, a and b of Eq.(3.3), as below. The influence to the observables is discussed in Section 5.4.5 and Appendix F.

3.4 Extraction of EDM

The EDMs can be extracted using the linear relation of Eq.(3.3), as described in Section 3.2. The sensitivity a_j and the offset b_j can be expressed by the following equations, where $j = Re, Im$ means the real or imaginary part of amplitudes, respectively:

$$a_j = \int \frac{(\mathcal{M}_j^2)^2}{\mathcal{M}_{\mathrm{SM}}^2} d\phi, \quad b_j = \int \mathcal{M}_j^2 d\phi. \tag{3.19}$$

In reality, experimental acceptance $\eta(\phi)$ has to be taken into account for the observable as (the expression for the imaginary part is similar):

$$\begin{aligned} \langle \mathcal{O}_{Re} \rangle &\propto \int \mathcal{O}_{Re} \eta(\phi) \mathcal{M}_{\mathrm{prod}}^2 d\phi, \\ &= \int \eta(\phi) \mathcal{M}_{Re}^2 d\phi + Re(d_\tau) \int \eta(\phi) \frac{(\mathcal{M}_{Re}^2)^2}{\mathcal{M}_{\mathrm{SM}}^2} d\phi, \qquad (3.20) \\ &= b_{Re} + Re(d_\tau) \cdot a_{Re}, \qquad (3.21) \end{aligned}$$

where the conversion parameters, a_j and b_j, are

$$a_j = \int \eta(\phi) \frac{(\mathcal{M}_j^2)^2}{\mathcal{M}_{\mathrm{SM}}^2} d\phi, \quad b_j = \int \eta(\phi) \mathcal{M}_j^2 d\phi. \tag{3.22}$$

Although these parameters are necessary to extract the EDM from the observable, it is difficult to analytically calculate this integral, because the acceptance function, η, is generally very complicated. Thus, the parameters a_j and b_j are extracted from the correlation between $\langle \mathcal{O}_{Re} \rangle$ ($\langle \mathcal{O}_{Im} \rangle$) and $Re(d_\tau)$ ($Im(d_\tau)$) obtained by a full MC simulation including the acceptance effects. The extraction of the parameters in the analysis is described in Section 5.3.1.

The MC events with the EDM effect are obtained by using the normal MC samples weighted by

$$w = \frac{\mathcal{M}_{\mathrm{SM}}^2 + Re(d_\tau) \mathcal{M}_{Re}^2 + Im(d_\tau) \mathcal{M}_{Im}^2 + |d_\tau|^2 \mathcal{M}_{d^2}^2}{\mathcal{M}_{\mathrm{SM}}^2}. \tag{3.23}$$

Figure 3.4 shows the distribution of the optimal observables, $\mathcal{O}_{Re}$ and $\mathcal{O}_{Im}$, for the MC events generated with the weight function of Eq.(3.23). In calculating the weight function, the unmeasurable kinematical variables, such as the τ flight direction, the neutrino momenta and the undetected radiative photons' information, are calculated with soft or hard radiations, separately, as below. The cut-off energy of the radiative photon is set to be 0.1% of $\sqrt{s}/2$ (= 5.29 MeV). Because the MC events are generated and reconstructed with the conceivable effects, such as the undetected radiative photons, the detector resolution, the acceptance effect, etc., the extracted parameters, a and b, can be applied to the experimental data.

No hard (soft) radiation case

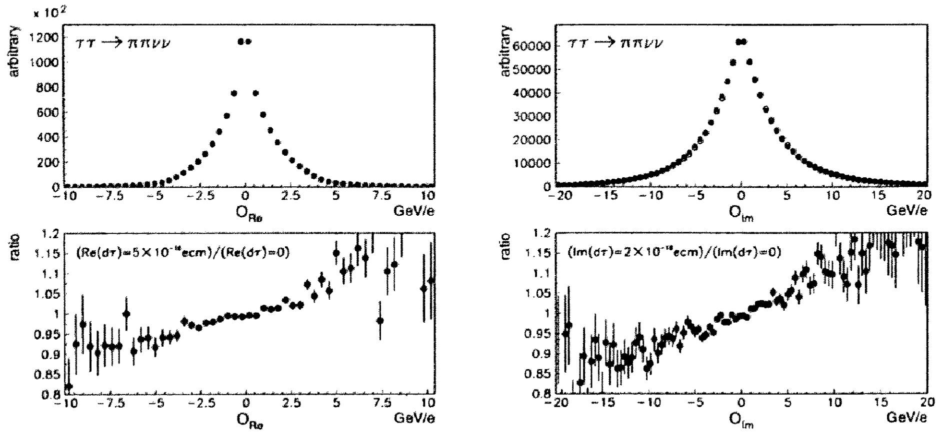

Figure 3.4: Distribution of the optimal observables for $\tau^+\tau^- \to \pi^+\pi^-\nu\bar{\nu}$. The bottom figures show the ratio of the distribution between the case for $Re(d_\tau) = 5 \times 10^{-16}/Im(d_\tau) = 2 \times 10^{-16} e\,\mathrm{cm}$ and the zero EDM.

In the case of no radiation or soft radiation, the amplitudes are calculated without a radiated photon, and are given as Eq.(2.18) - (2.21).

Hard radiation case

In the case for the reaction

$$e^+(\boldsymbol{p}_+) + e^-(\boldsymbol{p}_- \ (= -\boldsymbol{p}_+)\ ) \to \tau^+(\boldsymbol{k}_+, \boldsymbol{S}_+)\tau(\boldsymbol{k}_-, \boldsymbol{S}_-)\gamma(\boldsymbol{k}_\gamma),$$

the amplitudes of the τ-pair production vertex is calculated in the reaction frame determined by adding the radiative gamma vertex to the charge current, whose inner product ($|\boldsymbol{p}_+ \cdot \boldsymbol{k}_\gamma|$, $|\boldsymbol{p}_- \cdot \boldsymbol{k}_\gamma|$, $|\boldsymbol{k}_+ \cdot \boldsymbol{k}_\gamma|$ or $|\boldsymbol{k}_- \cdot \boldsymbol{k}_\gamma|$) is the smallest. Here, $\boldsymbol{k}_\gamma$ is the radiated photon's momentum.

If the radiative gamma arises from the $e^\pm$ as the initial-state radiation, the amplitudes are calculated in the $\tau^+\tau^-$ rest frame, where the momenta of $e^\pm$ and $\tau^\pm$ are boosted to the $\tau^+\tau^-$ rest frame. If $|\boldsymbol{p}_+ \cdot \boldsymbol{k}_\gamma|$ is the smallest inner product, the $-\boldsymbol{p}_-^*$ and $\boldsymbol{k}_+^*$ are taken as the momenta of the e^+ and τ^+. On the other hand, if $|\boldsymbol{p}_- \cdot \boldsymbol{k}_\gamma|$ is the smallest one, the $\boldsymbol{p}_+^*$ and $\boldsymbol{k}_+^*$ are taken. Here, the star denotes the momentum in the $\tau^+\tau^-$ rest frame.

If the radiative gamma come from the $\tau^\pm$ as the final-state radiation, the calculation is performed in the e^+e^- rest frame. If $|\boldsymbol{k}_+ \cdot \boldsymbol{k}_\gamma|$ is the smallest, the $\boldsymbol{p}_+$ and $-\boldsymbol{k}_-$ are used as the momenta of the e^+ and τ^+. On the other hand, if $|\boldsymbol{k}_- \cdot \boldsymbol{k}_\gamma|$ is the smallest, the $\boldsymbol{p}_+$ and $\boldsymbol{k}_+$ are used as the momenta of the e^+ and τ^+.

Chapter 4

KEKB/Belle experiment

In this section, an experimental complex composed of the KEKB accelerator and the Belle detector are introduced, along with the data-handling scheme.

The KEKB accelerator was constructed from 1994 in the tunnel of the TRISTAN accelerator at KEK. In December, 1998, the operation of the KEKB accelerator and the Belle detector started for high-energy physics experiments.

4.1 KEKB accelerator

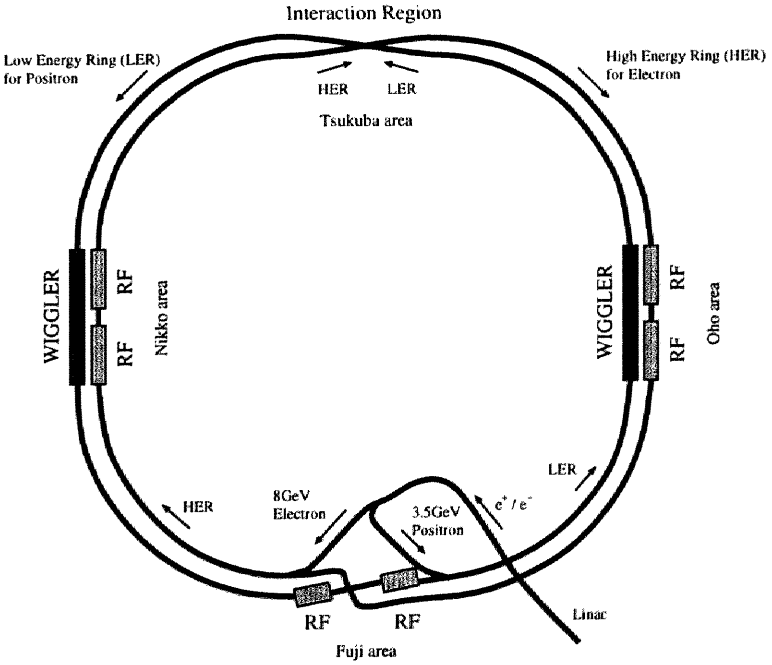

Figure 4.1: KEKB layout.

KEKB is an asymmetric energy e^+e^- collider, whose center-of-mass energy is 10.58 GeV, which corresponds to the energy of the $\Upsilon(4S)$ resonance. The asymmetric energy enables one to analyze time-dependent measurement of the CP asymmetry in a neutral B meson system. The layout of KEKB is shown in Figure 4.1. The electron and positron beams, whose energies are 8 and 3.5 GeV, respectively, are stored in two individual rings and collided at one interaction region with a crossing angle of 22 mrad. The main design parameters are summarized in Table 4.1.

The design luminosity is 10^{34} cm^{-2}s^{-1} and the design-integrated luminosity is on the order of 100 fb^{-1} per year. In this case, since the cross section of the τ pair production is 0.91 nb, the accelerator produces about 10^8 τ pair events in one year.

Ring	LER	HER	
Particles	e^+	e^-	
Energy (E)	3.5	8.0	GeV
Circumference (C)	3016.26		m
Luminosity (L)	10^{34}		cm^{-2}s^{-1}
Crossing angle (θ_x)	± 11		mrad
Tune shifts (ξ_x/ξ_y)	0.039/0.052		
Beta function at IP (β_x^*/β_y^*)	0.33/0.01		m
Beam current (I)	2.6	1.1	A
Natural bunch length (σ_z)	0.4		cm
Energy spread (σ_E/E)	7.1×10^{-4}	6.7×10^{-4}	
Bunch spacing (s_B)	0.59		m
Particles/bunch	3.3×10^{10}	1.4×10^{10}	
Emittance ($\varepsilon_x/\varepsilon_y$)	$1.8 \times 10^{-8}/3.6 \times 10^{-10}$		m
Synchrotron tune (ν_s)	$0.01 \sim 0.02$		
Betatron tune (ν_x/ν_y)	45.52/45.08	47.52/43.08	
Energy loss/turn (U_0)	$0.81^\dagger/1.5^\ddagger$	4.8	MeV
RF voltage (V_c)	$5 \sim 10$	$10 \sim 20$	MV
RF frequency (f_{RF})	508.887		MHz
Total beam power (P_b)	$2.7^\dagger/4.5^\ddagger$	4.0	MW

Table 4.1: KEKB design parameter (†, without wigglers; ‡, with wigglers)

4.2 Belle detector

Belle is a general-purpose detector with an asymmetric structure along the beam direction. A side view is shown in Figure 4.2. Here, only the detector components are described, which are mainly used in this analysis. The parameters of the sub-detectors are summarized in Table 4.2. Full details are given in Ref. [25].

Tracking system

The tracking system is composed of a silicon vertex detector (SVD) and a central drift chamber (CDC). SVD measures the track position of charged particles with three layer plates of a double-sided silicon strip. The strip pitch is 25μm along the azimuthal direction

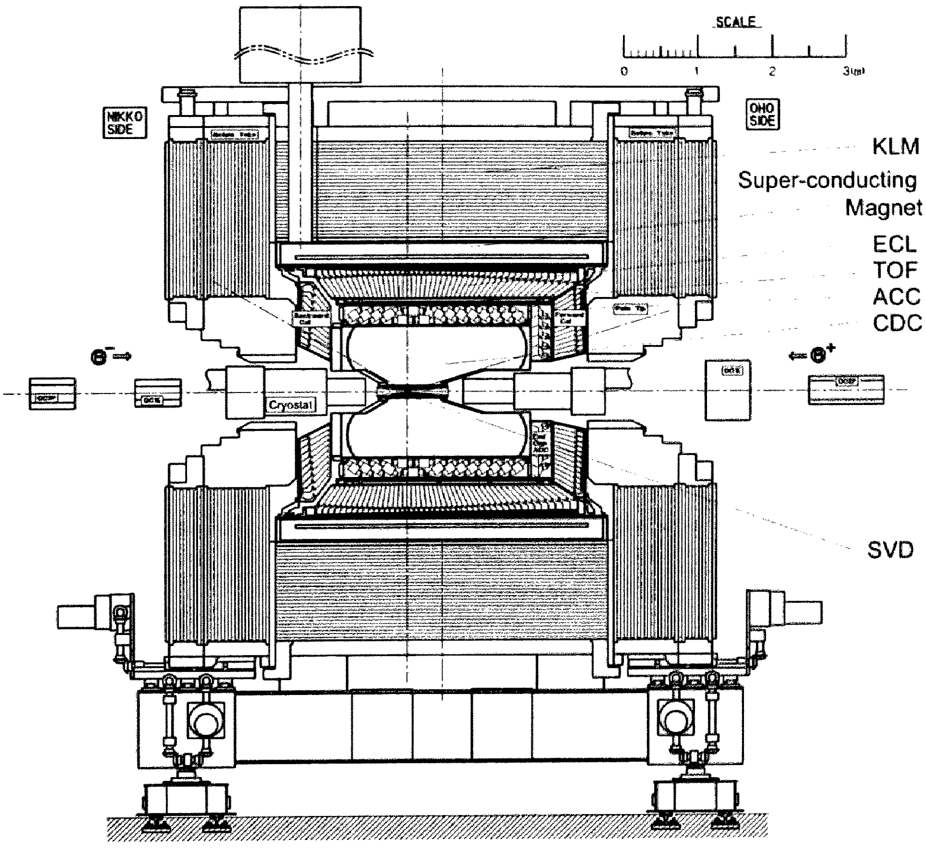

Figure 4.2: Side view of the Belle detector.

and 42μm along the z direction. The SVD angular coverage is $23° < \theta < 139°$, where θ is the polar angle. The CDC measures the trajectory of charged particles in a 1.5T magnetic field supplied by the super-conducting solenoid. The CDC has 50 cylindrical layers with 11 super-layers of axial and stereo layers. Its coverage is $17° < \theta < 150°$. The spatial resolution of the track position is about 130 μm for the r-ϕ direction and 200 $\sim$ 1400μm for the z direction. The momentum resolution measured with cosmic-ray and dimuon events is shown in Figure 4.3. The resulting resolution of the tracking system is

$$\frac{\sigma_{p_t}}{p_t} \sim 0.19 \cdot p_t \oplus \frac{0.34}{\beta}.$$

Electromagnetic calorimeter

The electromagnetic calorimeter (ECL), located inside the solenoid, measures the deposit shower energy of photons and electrons. ECL consists of segmented CsI(Tl) crystals with silicon photodiodes. The segmented array structure enables one to measure the shower position and its shape. The crystal length is 30cm (16.2 X_0) and its cross section is about 5 × 5 cm^2. The polar angle θ coverage is $12.4° < \theta < 31.4°$, $32.2° < \theta < 128.7°$ and $130.7° < \theta < 155.1°$ for the forward endcap, barrel and backward endcap, respectively. ECL is the primary detector for electron identification using the measured shower energy and the shower shape and the sole detector to measure the photon energy and the position. The

Detector	Type	Configuration	Readout	Performance
SVD	Double sided Si strip	$300\,\mu$m thick, 3 layers $r = 3.0 \sim 5.8\,$cm Length $= 22 \sim 34\,$cm	$\phi : 41\,$k $\theta : 41\,$k	$\sigma_{\Delta z} \sim 100\,\mu$m
CDC	Small cell drift chamber	Anode : 52 layers Cathode : 3 layers $r = 8.5 \sim 90\,$cm $-77 \leq z \leq 160\,$cm	A : 8.4 k C : 1.8 k	$\sigma_{r\phi} = 130\,\mu$m $\sigma_z = 200 \sim 1400\,\mu$m $\sigma_{p_t}/p_t = 0.3\%\sqrt{p_t^2+1}$ $\sigma_{\mathrm{d}E/\mathrm{d}x} = 6\%$
ACC	$n =$ $1.01 \sim 1.03$ Silica Aerogel	$\sim 12 \times 12 \times 12\,$cm^3 blocks 960 barrel 228 endcap FMPMT readout	1188	$\mu_{eff} \geq 6$ K/π : $1.2 \leq p \leq 3.5\,$GeV$/c$
TOF TSC	Plastic Scintillator	128 ϕ segmentation $r = 120\,$cm Length $= 3\,$m 64 ϕ segmentation	128×2	$\sigma_t = 100\,$ps $K/\pi : p \leq 1.2\,$GeV$/c$
ECL	CsI(Tl)	$\sim 5.5 \times 5.5 \times 30\,$cm^3 crystals Barrel: $r = 125 \sim 162\,$cm Endcap: $z = -102$ and $+196\,$cm	B : 6624 FE : 1152 BE : 960	σ_E/E= $0.066\%/E$ $\oplus\, 0.81\%/E^{1/4}$ $\oplus\, 1.34\%$ $\sigma_{pos} = 0.5\,\mathrm{cm}/\sqrt{E}$
KLM	Resistive plate counter	14 layers (5 cm Fe + 4 cm gap) 2 RPCs in each gap θ and ϕ strips	$\theta : 16\,$k $\phi : 16\,$k	$\Delta\phi = \Delta\theta$ $= 30\,$mrad for K_L $\sigma_t = 1\,$ns 1% hadron fakes for μ
EFC	BGO	$2 \times 1.5 \times 12\,$cm^3	$\theta : 5$ $\phi : 32$	$\sigma_E/E =$ $(0.3 \sim 1)\%/\sqrt{E}$
Beam pipe	Beryllium double-wall	Cylindrical, $r = 2.3\,$cm 0.5/2.5/0.5(mm) = Be / He / Be		He gas cooled
Magnet	Super- conducting	Inner radius = 170 cm		$B = 1.5\,$T

Table 4.2: Belle parameter. p and p_t are the momenta in unit of GeV$/c$, E is the energy in unit of GeV.

energy and position resolution are shown in Figures 4.4 and 4.5. The obtained resolutions depending on the incident energy are

$$\left(\frac{\sigma_E^2}{E}\right)^2 = \left(\frac{0.066(\%)}{E}\right)^2 + \left(\frac{0.81(\%)}{E^{1/4}}\right)^2 + (1.34(\%))^2,$$

and

$$\sigma_{\mathrm{position}}(\mathrm{mm}) = 0.27 + \frac{3.4}{E^{1/2}} + \frac{1.8}{E^{1/4}} \qquad (E \text{ in GeV}).$$

Muon detector

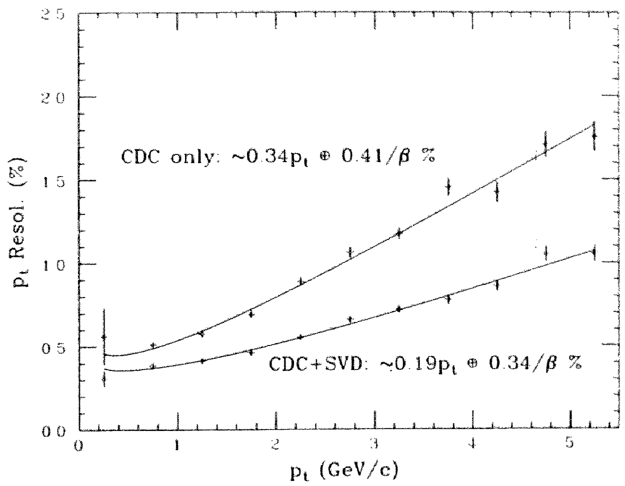

Figure 4.3: p_t resolution, σ_{p_t}/p_t, as a function of p_t. The crosses were obtained with cosmic rays. The circles were obtained with dimuon events. The curves are fitted results. The upper result is for the case where only CDC information is used in the track fitting, and the lower is for the case where SVD hits are included in the fit.

The K_L/μ detector (KLM), located most outside of Belle, detects the muon trajectory. KLM has 14 layers of 4.7 cm-thick iron plates and 15 super-layer 4 cm-thick detector modules in the barrel region (45° $< \theta <$ 125°) and 14 super-layers in the endcap region. The total polar angle coverage is 20° $< \theta <$ 155°. In one super-layer module, two glass-electrode resistive plate counters (RPCs) are installed between the θ and ϕ pickup-strips, which measure the signal induced by a discharge in the gas gap of RPCs. The size of the pickup-strips is about 50 mm wide with lengths from 1.5 to 2.7 m in the barrel region. The measured spatial resolution is 1.2 cm. Muons can be identified by measuring the length and the shape of the trajectory passing through the RPCs. Figure 4.6 shows the muon detection efficiency as a function of the momentum in KLM with a likelihood cut of 0.66.

PID devices

Other devices for the particle identification (PID) are the time-of-flight counter (TOF), the Aerogel Čerenkov counter (ACC) and the dE/dx in CDC. These devices provide likelihood ratio information for PID. Its likelihood ratios are also used for electron identification with the ECL information in order to improve the identification power.

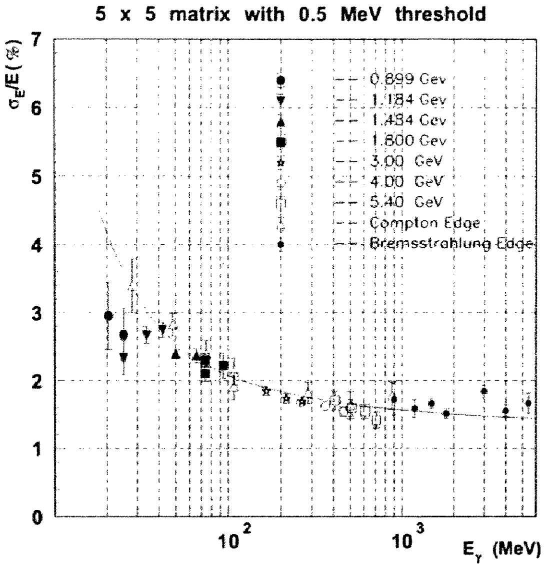

Figure 4.4: Energy resolution as a function of the incident photon energy for a 5 × 5 crystal matrix with a 0.5 MeV threshold. The curve shows the fitted result.

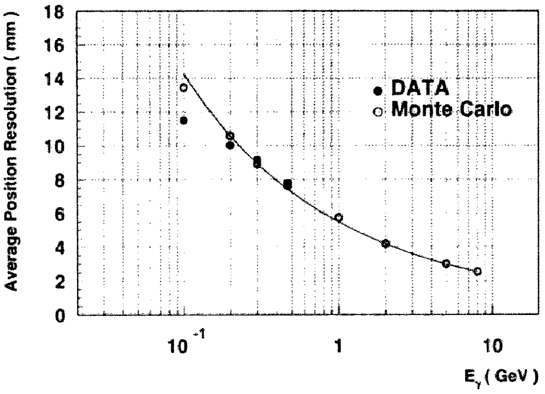

Figure 4.5: Average position resolution as a function of the incident photon energy. The dots are data and the circles were obtained from a MC simulation. The curve is the fitted result.

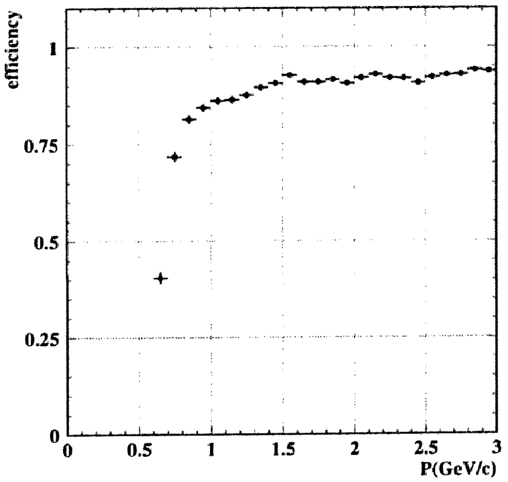

Figure 4.6: Muon detection efficiency as a function of the momentum in KLM with a likelihood cut of 0.66.

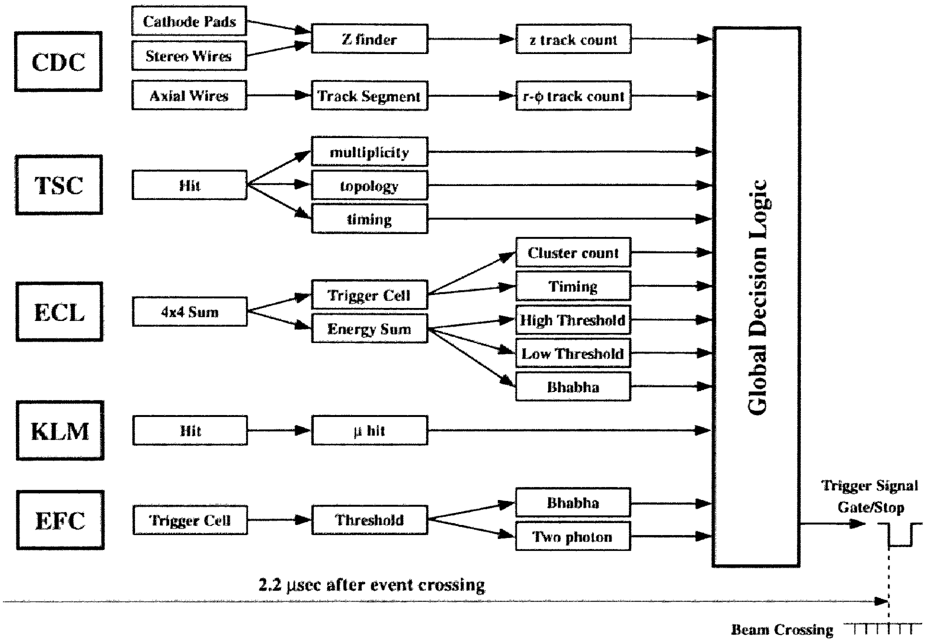

Figure 4.7: Flow chart of the level-1 trigger system.

4.3 Belle trigger system

The Belle trigger system consists of the level-1 hardware trigger (L1) and the level-3 (L3) and level-4 (L4) software triggers. The L3 trigger is implemented in the online computer system and L4 is in the offline reconstruction scheme. (L2 is complex hardware trigger system, and is currently not implemented.) The purpose of the trigger system is to select signal events and to suppress high-rate physical events, Bhabha and 2-photon processes, and the beam-related backgrounds. Recording τ pair events is more or less affected by the criteria of the trigger system, because τ pair events compose low-multiplicity events, and their event shape is somewhat similar to the suppressed events. The trigger system rejects a few % of the τ pair events.

Figure 4.7 shows a schematic view of the Belle L1 trigger system. It comprises the sub-trigger systems and the central trigger system, named Global Decision Logic (GDL). The sub-trigger systems provide trigger signals with each output of the sub-detectors. The track-triggers output the track counts on the r-ϕ plane and the z plane using segmented signals of the CDC. The trigger scintillation counters (TSC), located in front of TOF, produce timing information and the hit pattern to the GDL. ECL produces information about the measured energy level and the number of clusters. KLM yields a trigger related to a muon by using the hit information. GDL assembles the output from the sub-triggers, calculates the combination and then generates the event type.

The L3 software trigger is based on the bit selection output from L1 and the ultra-fast tracker. First, the L3 trigger checks the L1 trigger type, which concerns the energy triggers. Then, L3 executes an ultra-fast tracker and rejects an event which has no track with the condition $|z| < 5\,\mathrm{cm}$. The L3 trigger does not affect the physics events, but reduces the beam-related backgrounds. For the τ pair event used in the physics analysis, the effect of L3 is negligible.

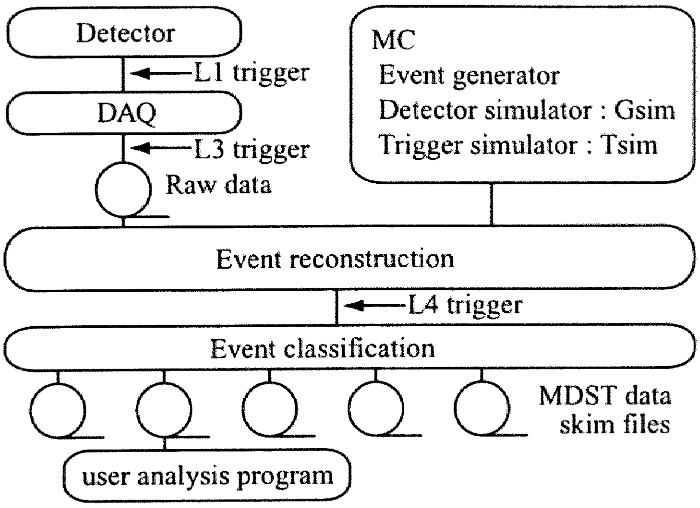

Figure 4.8: Scheme of the data flow.

The scheme of the L4 trigger is almost the same as L3, but the fast tracker is different. The L4 trigger checks the L1 trigger type and the energy measured by ECL (> 4GeV). Then, L4 scans the track information. L4 selects an event with at least one "good track", where "good track" is defined as a track with $p_t > 0.3$ GeV/c, and impact parameters of $|dr| < 1\,\mathrm{cm}$ and $|dz| < 4\,\mathrm{cm}$. The effect of L4 is also negligible for a physics analysis.

4.4 Monte Carlo simulation

A Monte Carlo (MC) event generator, KORALB/TAUOLA [27] is used for τ pair production and τ decays. It calculates the spin-dependent amplitudes with a QED on the order of α^3 for the process $e^+e^- \to \tau^+\tau^-(\gamma)$. The effect of the Z^0 exchange diagram is included with the low-energy approximation. The physics parameters, such as the decay branching ratios, the particle mass, the lifetime etc., are based on the PDG98 value [28]. A detector simulation is performed by a GEANT [29] based program, named GSIM. In order to investigate the effects of background from non τ pair events, we generated MC events for the continuum ($e^+e^- \to q\bar{q}$) and for $B\bar{B}$ ($e^+e^- \to \Upsilon(4S) \to B\bar{B}$) production using the QQ [30] program, two-photon processes ($2\gamma \to l^+l^-, q\bar{q}$) using the AAFHB [31] program, Bhabha and $\mu\mu$ with the initial radiation effect.

4.5 Data flow

Figure 4.8 shows the scheme of the data flow for the experimental data and the MC events. The experimental data, measured by the detector and triggered by the L1 trigger system described in Section 4.3, are accumulated to the data acquisition system (DAQ). After the online L3 trigger, the raw data are stored onto tape libraries. Then, event reconstruction is carried out on an offline computer farm. At the event reconstruction stage, the L4 trigger is applied, and then the events are classified into skim files, depending on the event shape, the measured energy and such. We use the skim files for physics analysis. For this analysis, Tau-pair skim files are used, which include τ pair-like events, such as low multiplicity events with some missing momentum and some visible energy. The detailed selection criteria of the Tau-pair skim files are described in Appendix C.

For MC events, the data flow is basically the same as that for the experimental data. The MC samples produced by the event generator pass into the detector simulator and the trigger simulator. Then, event reconstruction and classification are carried out by programs applied to the experimental data.

Chapter 5

Analysis

In order to calculate the matrix elements, we need to know all momenta of the decay particles, except for that of the neutrino, and to know the particle type, hadron or lepton. Therefore, in this analysis, the final state mode is chosen exclusively by identifying each observed particle. The selected modes are $e\mu(4\nu)$, $e\pi(3\nu)$, $\mu\pi(3\nu)$, $e\rho(3\nu)$, $\mu\rho(3\nu)$, $\pi\rho(2\nu)$, $\pi\pi(2\nu)$ and $\rho\rho(2\nu)$. These eight modes amount to a branching fraction of 45%.

Here, 29.5 fb^{-1} data are used, which correspond to 26.8 million τ pairs, accumulated by the summer of 2001. As described in Section 4.5, τ pre-selection is applied to the data. Its selection criteria are summarized in Appendix C.

5.1 Event selection

First, signal events are required to have two charged tracks with zero net-charge and no photon, except for the daughter of the $\rho^{\pm}$. The latter requirement is to remove any event with the initial-state radiation. Each charged track is demanded to have a transverse momentum of $p_t > 0.1\mathrm{GeV}/c$, and photon candidates should deposit an energy of $E > 0.1\mathrm{GeV}$ in the ECL in order to reduce the fake tracks and photons related to the beam background.

5.1.1 Particle identification

The four daughter particles are selected exclusively based on the following selection criteria:

Electron

An electron track is identified using a likelihood ratio combining dE/dx in the CDC, the ratio of the energy deposited in the ECL and the momentum measured in the CDC, the shower shape of the ECL and the hit information from the ACC. The likelihood ratio is required to be greater than 0.95. The identification efficiency is estimated to be 92% with a $\pi^{\pm}$ fake rate of 0.3% [32].

Muon

A muon is identified by its range and hit pattern passing through KLM detector. The likelihood ratio is required to be greater than 0.95. The detection efficiency is 91% and its fake rate is 2%.

Pion

A pion is identified based on the KLM hit information by requiring its hadron probability, which is defined as 1−(muon likelihood ratio), to be greater than 0.95, and simultaneously the likelihood ratio as an electron to be less than 0.01. The efficiency is estimated to be 81% and the purity for the selected sample is 89%.

Rho

A $\rho^{\pm}$ is reconstructed from a charged track and π^0 while requiring the opening angle of these particles to be less than 90 degrees and the charged track not to be an electron or muon. The daughter π^0 reconstructed from $\gamma\gamma$ should have an invariant mass of between 110 and 150 MeV/c^2 and a momentum of $p_{\mathrm{lab.}} > 0.2$GeV/c. Figure 5.1 shows the $\gamma\gamma$ invariant mass distribution before π^0 event selection. Figure 5.2 shows the $(\pi^{\pm}, \pi^0)$ invariant mass distribution for the selected $\rho^{\pm}$.

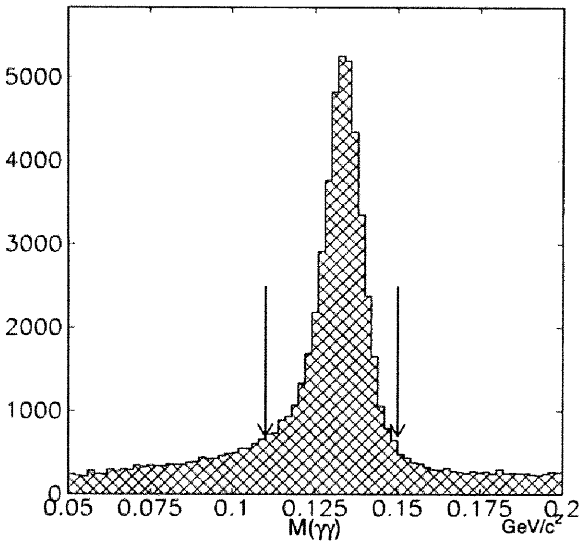

Figure 5.1: $\gamma\gamma$ invariant mass distribution for the experimental data in the 1 prong - 1 prong topology event. The arrows show the selected boundary.

5.1.2 Background rejection

In order to reduce the background and to enhance the particle-identification power, the lepton e/μ is required to be within the barrel region, $-0.60 < \cos\theta_{\mathrm{lab.}} < 0.83$, while the $\pi^{\pm}$ is $-0.50 < \cos\theta_{\mathrm{lab.}} < 0.62$, where $\cos\theta_{\mathrm{lab.}}$ indicates the cosine of the polar angle in the laboratory system. Because of the large discrepancy concerning the $\pi^{\pm}$ detection efficiency between the data and MC in the KLM endcap region, the endcap region is not used for the $\pi^{\pm}$ selection. Therefore, the $\cos\theta$ criteria for $\pi^{\pm}$ is narrower than that for the lepton. Further criteria are imposed: their electron momentum should be greater than 0.5 GeV/c, the muon and pion momenta greater than 1.2 GeV/c and the $\rho^{\pm}$ momentum greater than 1.0 GeV/c. All of these momenta are calculated in the laboratory frame.

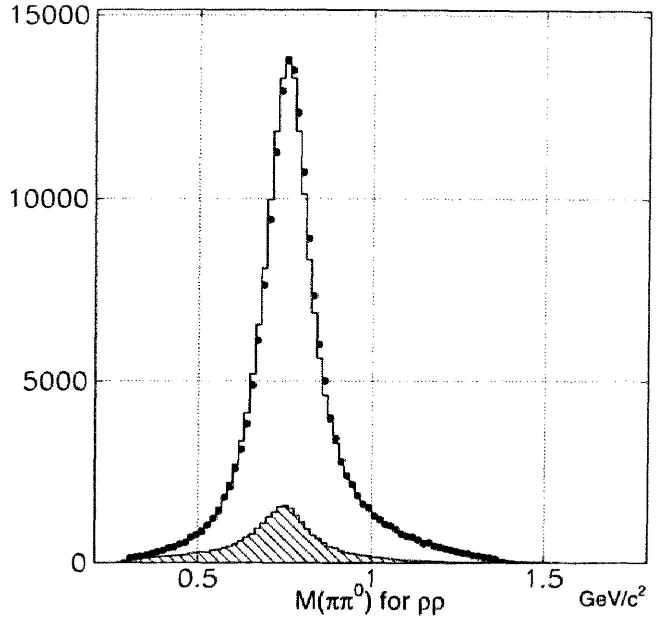

Figure 5.2: $\pi\pi^0$ invariant mass distribution. The dots represent the experimental data, and the histogram is the MC expectation, which is scaled by the number of entries. The hatched histogram is the background, which is not from $\tau\tau \to \rho\rho\nu\nu$.

In order to suppress the two-photon background the missing momentum is required not to be directed along the beam pipe, $-0.950 < \cos\theta_{\mathrm{missing,lab.}} < 0.985$. Figure 5.3 shows the polar-angle distribution of the missing momentum vector for the signal MC and the two-photon MC. The large peak at the forward direction of the two-photon process can be removed efficiently by this selection criterion. To reject Bhabha and $\mu\mu$ backgrounds, the sum of the charged track momenta in CM frame is required to be less than 9.0 GeV/c. For the $e\pi$ mode, Bhabha contamination is reduced by imposing the following criteria. The opening angle of the two charged particles in the r-ϕ plane perpendicular to the beam axis is greater than 175 degrees and the sum of the charged track momenta in the CM frame is greater than 6.0 GeV/c. Figure 5.4 shows scatter plots on the opening angle-vs-momentum sum for the data and τ pair MC. A large peak is seen in the rejected region, which is attributed to Bhabha events, though one of electrons is misidentified as π.

The above event selection criteria are summarized in Table 5.1.

5.1.3 Other requirements

In order to include a trigger effect, a simulator regarding the hardware trigger is equipped in the MC simulation. The trigger efficiency is evaluated to be about 96%, as listed in Table 5.2. (See Appendix D for details.)

Events are removed when the τ flight direction cannot be constructed. Many background processes and τ pairs with hard initial-state radiation are rejected. Figure 5.5 shows the photon energy distribution of the initial-state radiation; it is found that events with a hard photon are easily removed. The rejected event rate is 2.4% for the $e\mu$ mode, about 6-7%

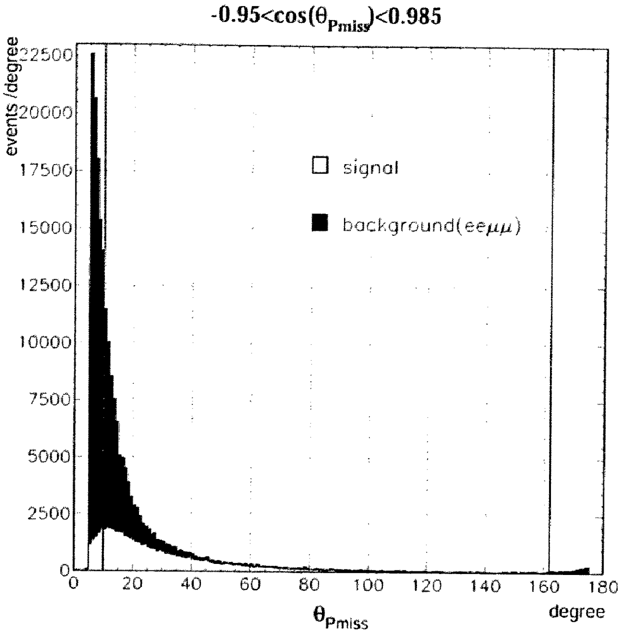

Figure 5.3: Polar-angle distribution of the missing momentum for the $e\mu$ mode. The open histogram is the signal MC and the filled histogram is the two-photon ($ee\mu\mu$) MC. The lines show the selection boundary.

for lepton-hadron mode and about 25-30% for the hadron-hadron mode. For the leptonic modes, owing to an additional ambiguity of $m_{\nu\nu}$ in the calculation of the observables, the τ direction is reconstructed in many cases, even with hard radiation. Therefore, the rejected rate for the leptonic decay is smaller than the hadronic decay.

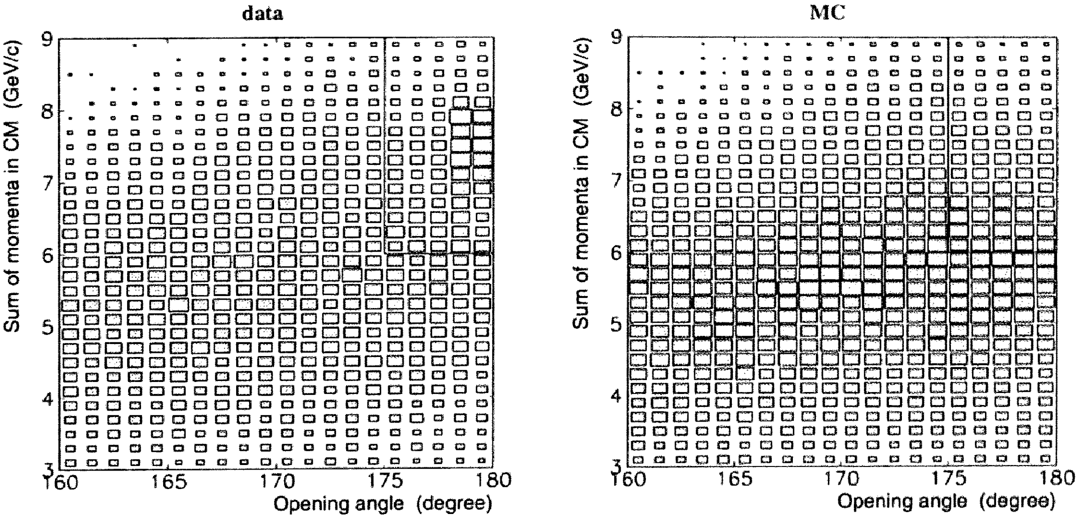

Figure 5.4: Sum of the momenta in the CM frame and the opening angle of two charged particles in the r-ϕ plane for the data (left) and $\tau\tau$ MC (right). The line shows the selection boundary.

Table 5.1: Event selection criteria. $\theta_{\pi^\pm\pi^0}$ indicates the opening angle between the $\pi^\pm$ and π^0 directions. $\theta_{e\pi}$ shows the opening angle between two charged tracks for the $e\pi$ mode.

Charged tracks :	$p_t > 0.1$ GeV/c
Gammas :	$E_\gamma > 0.1$ GeV
2 charged tracks with zero net charge	
No gamma except for the daughter of $\rho^\pm$	
Electron ID:	Electron likelihood > 0.95
	$p > 0.5$ GeV/c, $-0.60 < \cos\theta < 0.83$
Muon ID:	Muon likelihood > 0.95
	$p > 1.2$ GeV/c, $-0.60 < \cos\theta < 0.83$
Pion ID:	Hadron likelihood > 0.95, Electron Likelihood < 0.01
	$p > 1.2$ GeV/c, $-0.50 < \cos\theta < 0.62$
$\rho^\pm$: $\to \pi^\pm\pi^0$	$\theta_{\pi^\pm\pi^0} < 90^\circ$, $p > 1.0$ GeV/c
	$\pi^\pm$: not-e and not-μ
	π^0 : $\to \gamma\gamma$
	$110 < M(\gamma\gamma) < 150$ MeV/c^2, $p_{\pi^0} > 0.2$ GeV/c
$-0.95 < \cos\theta_{\mathrm{missing}} < 0.985$	
$\Sigma\lvert p\rvert < 9.0$ GeV/c	
For $e\pi$ mode:	$\theta_{e\pi} < 175^\circ$ or $\Sigma\lvert p\rvert < 6.0$ GeV/c

Table 5.2: Trigger efficiencies evaluated by $\tau\tau$ MC.

mode	$e\mu$	$e\pi$	$\mu\pi$	$e\rho$	$\mu\rho$	$\pi\rho$	$\rho\rho$	$\pi\pi$
efficiency(%)	96.6	95.0	95.1	93.1	98.5	97.5	97.5	95.0

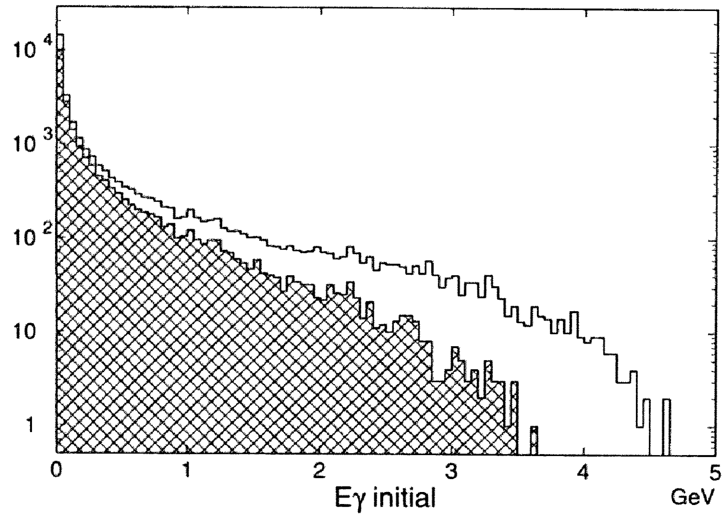

Figure 5.5: Photon energy distribution from the initial-state radiation in the CM system for the $\rho\rho$ mode. The hatched histogram is for the selected samples, and the blank part indicates the rejected ones.

5.2 Selected samples

The results of the above-mentioned selection are listed in Table 5.3. About 1.19 million events are extracted in total. The dominant background sources evaluated by MC are summarized in Table 5.4 along with its rate. Many background events from τ decay are found because of the missing π^0 and the misidentified kaon. For the mode including $\pi^{\pm}$, there are also many backgrounds from μ misidentified as π. The background events from two-photon processes remain at a few %. The other background events, which are Bhabha, $\mu\mu$ and multihadronic processes, contribute at less than a 1% level. In the table, the ratios of the data yield to the MC expectation are also shown, and are found to differ from one. One reason is the difference in the branching ratio between the data (or PDG2000 value) and the MC generation. For $\tau \to \pi\nu$ decay, the difference is about 2%. Another reason is the π^0 mass width. As shown in Figure 5.6, the mass width of the data is wider than that of the MC expectation. Since the π^0 mass selection is applied, the yield of the data is different from the MC. The difference is about 3%. The trigger efficiency also makes the difference a few %.

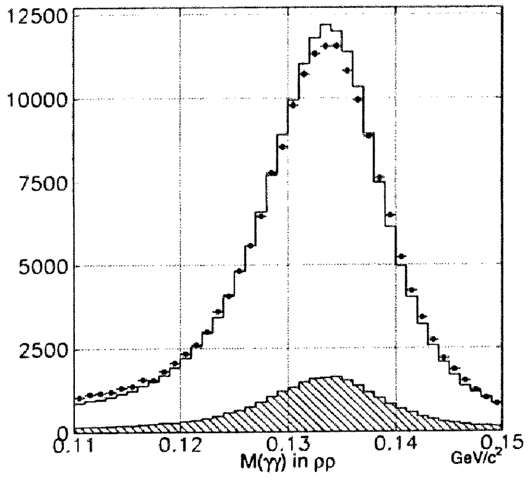

Figure 5.6: $\gamma\gamma$ invariant mass distribution after selecting the π^0 mass. The dots are data and histogram is the MC expectation scaled by the number of entries. The hatched histogram shows the background component.

The momentum distributions and angular $\cos\theta$ distributions of the individual final particles in the laboratory frame are shown in Figures 5.7 and 5.8, respectively. Although the low-momentum regions of the electron and the pion show some disagreement between the data and the MC, the MC predictions match the obtained data in total.

The center-of-mass energy distribution of the τ pairs for selected samples is shown in Figure 5.9, where because of the initial-state radiation a long tail can be seen. The mean value is 10.38 GeV.

Figure 5.10 shows the distribution of N_{hit}, whose definition is described in Section 3.3 for all modes including the leptonic τ decay. Very good agreement between the selected data and MC is found. The MC simulation reproduces the experimental data quite well.

The distributions of the observed $\mathcal{O}_{Re}$ and $\mathcal{O}_{Im}$ are shown in Figure 5.11, together with the MC calculation with zero EDM. The mean values of the measured observables for each

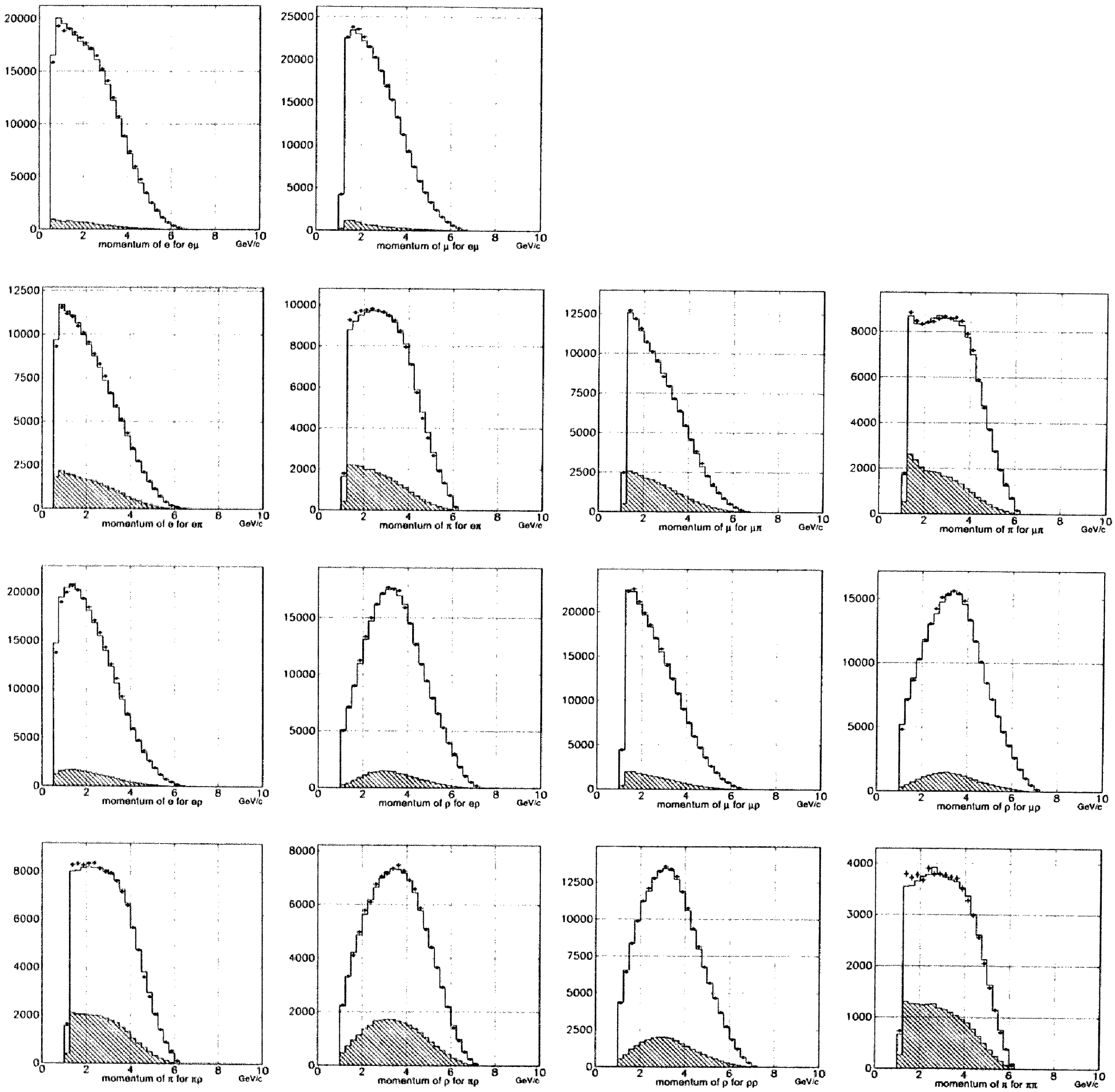

Figure 5.7: Momentum distributions in the laboratory frame for each particle of each final-state mode. The dots are the experimental data, and the histogram is the MC expectation scaled by the number of entries. The hatched histogram is the background component.

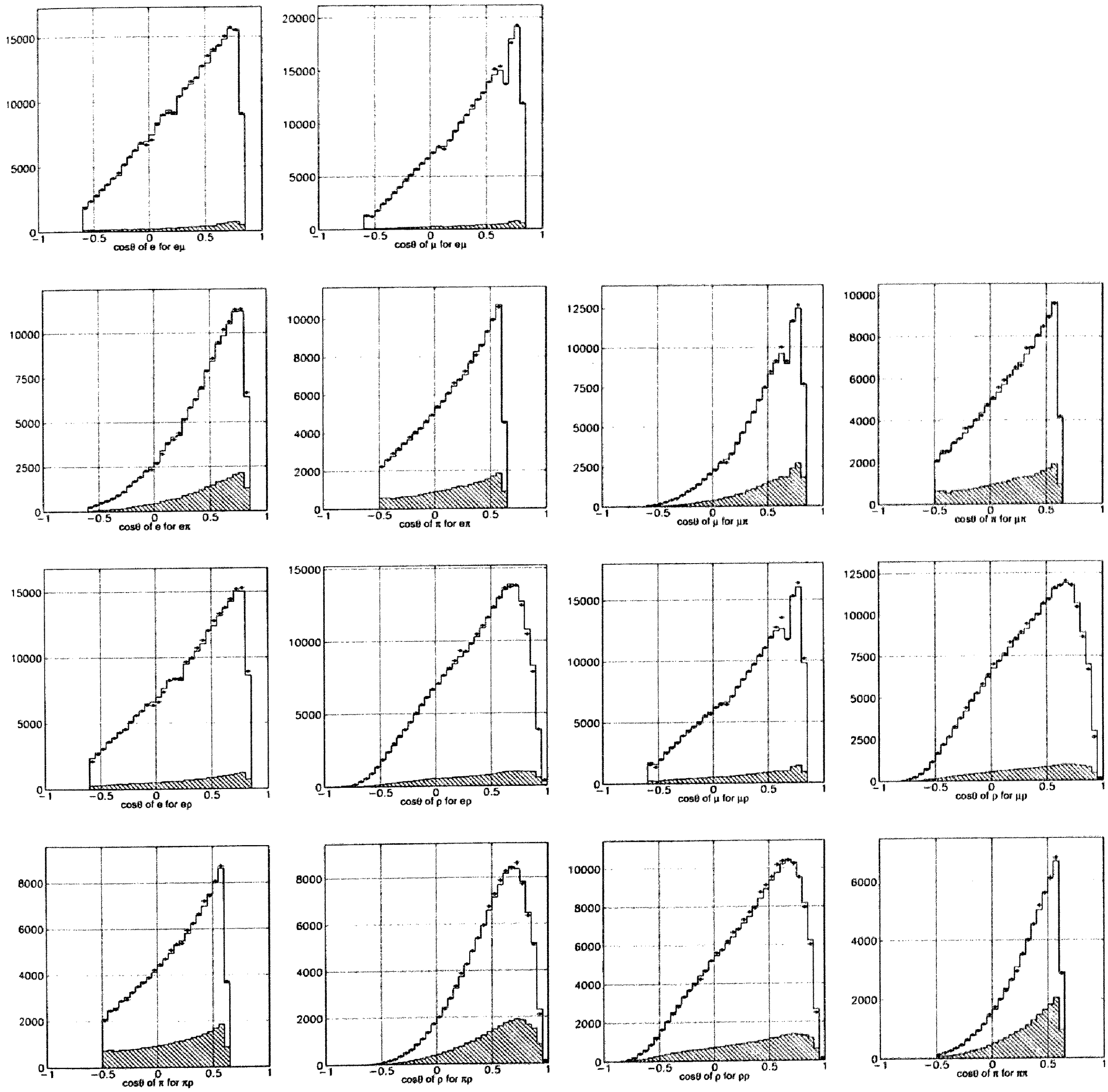

Figure 5.8: $\cos\theta_{\mathrm{lab}}$. distributions. The meaning of the dots and histograms are the same as in Figure 5.7.

Table 5.3: Status of selected samples. The purity is evaluated by MC events, and the error of the purity is due to the MC statistics. "data/MC" means the ratio of the yield between the data and the MC expectation normalized by the integrated luminosity. The efficiency, "eff.", is estimated by MC.

mode	yield	purity(%)	data/MC(%)	eff.(%)
$e\mu$	250948	96.6 ± 0.1	96.3 ± 0.2	15.14
$e\pi$	132574	82.5 ± 0.1	92.1 ± 0.3	11.18
$\mu\pi$	123520	80.6 ± 0.1	93.2 ± 0.3	10.32
$e\rho$	240501	92.4 ± 0.1	93.0 ± 0.2	9.83
$\mu\rho$	217156	91.6 ± 0.1	90.6 ± 0.2	9.29
$\pi\rho$	110414	77.7 ± 0.1	86.5 ± 0.3	6.56
$\rho\rho$	93016	86.2 ± 0.1	86.3 ± 0.3	5.37
$\pi\pi$	28348	70.0 ± 0.2	88.5 ± 0.5	6.80

Table 5.4: Dominant background sources for each selected mode evaluated by MC.

mode	background mode (rate%)
$e\mu$	$2\gamma \to \mu\mu(1.9\%)$, $\tau\tau \to e\pi(1.1\%)$
$e\pi$	$\tau\tau \to e\rho(6.0\%)\ eK(5.4\%)\ e\mu(3.1\%)\ eK^*(1.3\%)$
$\mu\pi$	$\tau\tau \to \mu\rho(5.7\%)\ \mu K(5.3\%)\ \mu\mu(2.9\%)\ \mu K^*(1.2\%)$, $2\gamma \to \mu\mu(2.0\%)$
$e\rho$	$\tau\tau \to e\pi\pi^0\pi^0(4.4\%)\ eK^*(1.7\%)$
$\mu\rho$	$\tau\tau \to \mu\pi\pi^0\pi^0(4.2\%)\ \mu K^*(1.6\%)\ \pi\rho(1.0\%)$
$\pi\rho$	$\tau\tau \to \rho\rho(5.1\%)\ K\rho(4.9\%)\ \pi\pi\pi^0\pi^0(3.8\%)\ \mu\rho(2.7\%)\ \pi K^*(1.4\%)$
$\rho\rho$	$\tau\tau \to \rho\pi\pi^0\pi^0(8.0\%)\ \rho K^*(3.1\%)$
$\pi\pi$	$\tau\tau \to \pi\rho(9.2\%)\ \pi K(9.2\%)\ \pi\mu(4.7\%)\ \pi K^*(2.0\%)$

mode are listed in Table 5.5.

Table 5.5: Mean values of the observables.

mode	$\langle \mathcal{O}_{Re} \rangle$ (GeV/e)	$\langle \mathcal{O}_{Im} \rangle$ (GeV/e)
$e\mu$	0.0035 ± 0.0013	0.0016 ± 0.0061
$e\pi$	0.0025 ± 0.0029	-0.0092 ± 0.0101
$\mu\pi$	0.0001 ± 0.0033	0.0007 ± 0.0120
$e\rho$	-0.0016 ± 0.0036	0.0041 ± 0.0074
$\mu\rho$	0.0037 ± 0.0040	-0.0127 ± 0.0082
$\pi\rho$	0.0110 ± 0.0099	0.0074 ± 0.0185
$\rho\rho$	-0.0049 ± 0.0110	0.0009 ± 0.0194
$\pi\pi$	-0.0012 ± 0.0085	-0.0561 ± 0.0319

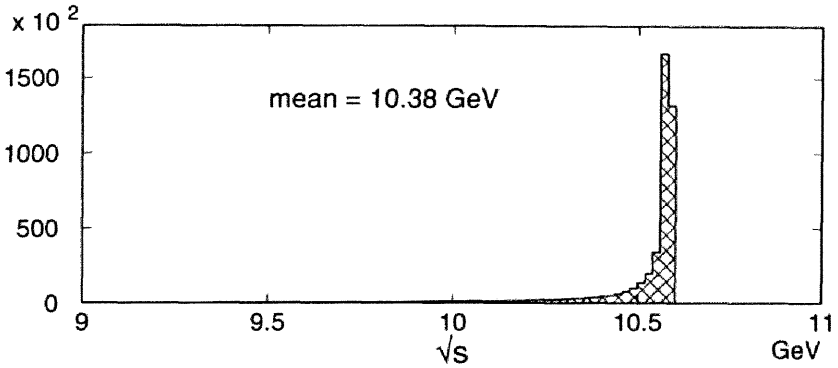

Figure 5.9: Center-of-mass energy distribution of the τ pairs for the observed events obtained by the MC.

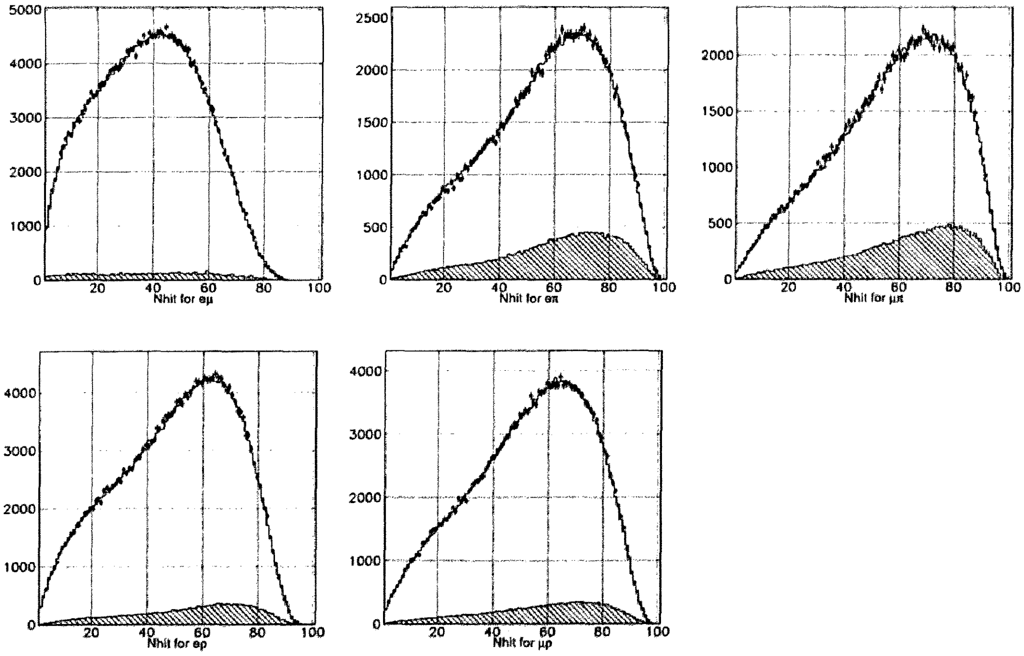

Figure 5.10: N_{hit} distributions for each mode. The dots are the experimental data and the histogram is the MC expectation scaled by the number of entries. The hatched histogram is the background component.

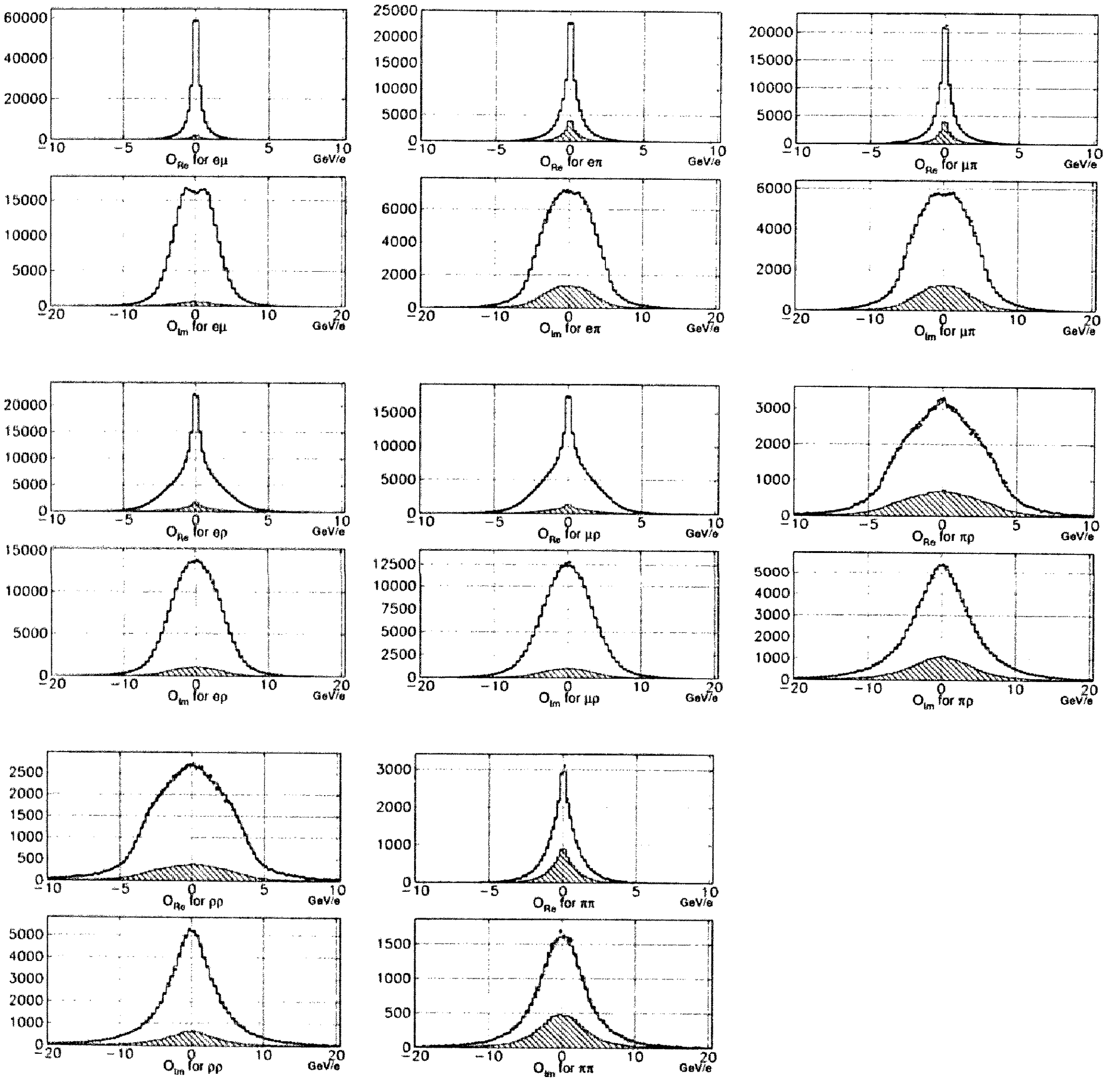

Figure 5.11: Observable distributions for each mode. The top figures in each mode show $\mathcal{O}_{Re}$ and the bottom ones show $\mathcal{O}_{Im}$. The dots are the experimental data and the histogram is the MC expectation scaled by the number of entries. The hatched histogram shows the background.

5.3 Observables and EDM

5.3.1 Sensitivity and offset

EDM can be extracted based on the following linear relation for the mean of measured observable:

$$\langle \mathcal{O}_{Re} \rangle = a_{Re} \cdot Re(d_\tau) + b_{Re}, \quad \langle \mathcal{O}_{Im} \rangle = a_{Im} \cdot Im(d_\tau) + b_{Im}. \tag{5.1}$$

The conversion parameters, a and b, can be obtained by the MC simulation as follows. Figure 5.12 shows the thus-calculated correlation between $\langle \mathcal{O} \rangle$ and d_τ for each mode. These relations are obtained from the signal MC samples with the detector simulation and the event selection. By fitting Eq.(5.1) to this correlation, the coefficients a and the offsets b are obtained. The resulting parameters are listed in Table 5.6 and plotted in Figure 5.13 to compare with each other mode.

Table 5.6: Conversion parameters, a and b, for each mode obtained by MC. The errors are due to the MC statistics. The units are (GeV/e / 10^{-16}ecm) for a and (GeV/e) for b.

mode	a_{Re}	b_{Re}	a_{Im}	b_{Im}
$e\mu$	0.0012 ± 0.0002	0.0009 ± 0.0005	0.0304 ± 0.0009	0.0138 ± 0.0022
$e\pi$	0.0051 ± 0.0005	-0.0005 ± 0.0012	0.0598 ± 0.0017	0.0096 ± 0.0040
$\mu\pi$	0.0048 ± 0.0006	0.0022 ± 0.0013	0.0762 ± 0.0020	-0.0127 ± 0.0047
$e\rho$	0.0113 ± 0.0006	-0.0010 ± 0.0013	0.0600 ± 0.0011	0.0050 ± 0.0027
$\mu\rho$	0.0112 ± 0.0006	0.0026 ± 0.0015	0.0686 ± 0.0013	-0.0126 ± 0.0030
$\pi\rho$	0.0499 ± 0.0016	-0.0027 ± 0.0038	0.1710 ± 0.0030	0.0360 ± 0.0071
$\rho\rho$	0.0509 ± 0.0017	0.0009 ± 0.0040	0.1628 ± 0.0030	0.0124 ± 0.0070
$\pi\pi$	0.0095 ± 0.0015	-0.0035 ± 0.0036	0.1165 ± 0.0055	-0.0874 ± 0.0128

The coefficients, a_{Re} and a_{Im}, give the sensitivities to $Re(d_\tau)$ and $Im(d_\tau)$, respectively. The $\pi\rho$ and $\rho\rho$ modes have a higher sensitivity to $Re(d_\tau)$ than the others, and the $\pi\rho$, $\pi\pi$ and $\rho\rho$ modes to $Im(d_\tau)$. The modes with leptons are less sensitive due to a lack of information on the τ and the spin directions. As can be seen from the values of coefficient a, the $\pi\rho$ and $\rho\rho$ modes have the highest sensitivity for d_τ, while the $\pi\pi$ mode has a somewhat lower sensitivity. For the real part, this is an effect of averaging over the two solutions for the τ direction; in the $\tau \to \pi\nu$ case, this causes spin-correlation information to be lost, whereas for $\tau \to \rho\nu$ the angular distribution of the $\rho \to \pi\pi^0$ decay provides information on the τ spin, which survives the averaging procedure. Figure 5.14 shows the $\mathcal{O}_{Re}$ distributions, as examples, for the $\pi\pi$ and $\rho\rho$ modes. The wider distribution reflects the higher sensitivity; the sensitivities are equal to the mean of the squared observable in an ideal case, as described in Section 3.2. For the $\pi\pi$ mode, the width becomes smaller when the average of the amplitudes over the τ direction is taken. On the other hand, for the $\rho\rho$ mode, the change in the width is small. When the τ direction is supposed to be known, the $\pi\pi$ mode yields a distribution similar to that of the $\rho\rho$ mode. For the imaginary part, the lower sensitivity of the $\pi\pi$ mode is due to the tight $\cos\theta$ cut applied to pions in the $\tau \to \pi\nu$ channel, compared to $\tau \to \rho\nu$; there is also a small effect due to the tighter momentum cut.

The larger offset for the imaginary part rather than that for the real part is due to the forward/backward asymmetric acceptance. The offset for the real part is consistent with zero within the statistical errors.

A more detailed study is described in Appendix E.

5.3.2 Background correction

Because the spin direction directly correlates with the momenta of the final-state particles, the misidentified background contamination affects the relation between $\langle \mathcal{O} \rangle$ and d_τ. Therefore, this effect in corrected based on the sensitivities a and the offsets b as below. The effective sensitivity $a^{\rm eff}$ and offset $b^{\rm eff}$ are given by

$$a^{\rm eff} = pa + r_{\rm bg} a^{\rm bg}, \quad b^{\rm eff} = pb + r_{\rm bg} b^{\rm bg} + r_{\gamma\gamma} b^{\gamma\gamma}, \tag{5.2}$$

where $a^{\rm bg}$ and $b^{\rm bg}$ are parameters reflecting the effect by the misidentified τ backgrounds. $b^{\gamma\gamma}$ is the offset from two-photon backgrounds, p is the sample's purity, $r_{\rm bg}$ is the background rate-to-signal τ decay and $r_{\gamma\gamma}$ is the two-photon rate to signals, which are listed in Table 5.4. The obtained background parameters, $a^{\rm bg}$ and $b^{\rm bg}$, are shown in Table 5.7 and are plotted in Figure 5.15. The offset from the two-photon backgrounds is listed in Table 5.8.

Using these parameters, the effective sensitivities $a^{\rm eff}$ and offsets $b^{\rm eff}$ are given in Table 5.9 and Figure 5.16. The effect of the background correction is about 10% for the sensitivity. The size of the offset correction is almost the same as the statistical error of the parameters. Because of the small background rate, the size of the correction parameter is insignificant.

Table 5.7: Parameters $a^{\rm bg}$ and $b^{\rm bg}$ for the background MC. The errors are due to the MC statistics. The units are (GeV/c / 10^{-16}ecm) for $a^{\rm bg}$ and (GeV/c) for $b^{\rm bg}$.

mode	$a^{\rm bg}_{Re}$	$b^{\rm bg}_{Re}$	$a^{\rm bg}_{Im}$	$b^{\rm bg}_{Im}$
$e\mu$	0.0003 ± 0.0024	0.0054 ± 0.0054	-0.0310 ± 0.0092	0.0077 ± 0.0229
$e\pi$	0.0035 ± 0.0010	0.0050 ± 0.0023	0.0374 ± 0.0036	-0.0283 ± 0.0085
$\mu\pi$	0.0012 ± 0.0012	0.0000 ± 0.0028	0.0387 ± 0.0043	0.0021 ± 0.0103
$e\rho$	0.0019 ± 0.0018	-0.0086 ± 0.0042	0.0132 ± 0.0041	0.0033 ± 0.0096
$\mu\rho$	-0.0011 ± 0.0022	0.0103 ± 0.0053	0.0141 ± 0.0045	0.0023 ± 0.0107
$\pi\rho$	0.0175 ± 0.0032	-0.0066 ± 0.0075	0.0813 ± 0.0058	0.0600 ± 0.0136
$\rho\rho$	0.0157 ± 0.0046	-0.0015 ± 0.0106	0.0557 ± 0.0080	0.0581 ± 0.0186
$\pi\pi$	0.0036 ± 0.0022	-0.0065 ± 0.0052	0.0556 ± 0.0089	-0.0602 ± 0.0208

Table 5.8: Offset for the two-photon background $b^{\gamma\gamma}$. The errors are due to the MC statistics.

mode	$b^{\gamma\gamma}_{Re}$ (GeV/c)	$b^{\gamma\gamma}_{Im}$ (GeV/c)
$e\mu$	0.0000 ± 0.0002	0.0039 ± 0.0020
$\mu\pi$	0.0000 ± 0.0005	0.0029 ± 0.0019

Table 5.9: Corrected parameters a^{eff} and b^{eff}. The errors are due to the MC statistics. The units are (GeV/e / $10^{-16}e$cm) for a^{eff} and (GeV/e) for b^{eff}.

mode	a^{eff}_{Re}	b^{eff}_{Re}	a^{eff}_{Im}	b^{eff}_{Im}
$e\mu$	0.0011 ± 0.0002	0.0010 ± 0.0005	0.0289 ± 0.0009	0.0138 ± 0.0021
$e\pi$	0.0048 ± 0.0004	0.0005 ± 0.0010	0.0559 ± 0.0015	0.0030 ± 0.0036
$\mu\pi$	0.0041 ± 0.0005	0.0018 ± 0.0012	0.0681 ± 0.0018	-0.0098 ± 0.0042
$e\rho$	0.0106 ± 0.0005	-0.0016 ± 0.0013	0.0564 ± 0.0011	0.0048 ± 0.0026
$\mu\rho$	0.0102 ± 0.0006	0.0032 ± 0.0014	0.0640 ± 0.0012	-0.0114 ± 0.0029
$\pi\rho$	0.0426 ± 0.0014	-0.0036 ± 0.0033	0.1510 ± 0.0027	0.0413 ± 0.0063
$\rho\rho$	0.0460 ± 0.0016	-0.0013 ± 0.0038	0.1481 ± 0.0028	0.0187 ± 0.0066
$\pi\pi$	0.0077 ± 0.0014	-0.0044 ± 0.0030	0.0982 ± 0.0047	-0.0793 ± 0.0109

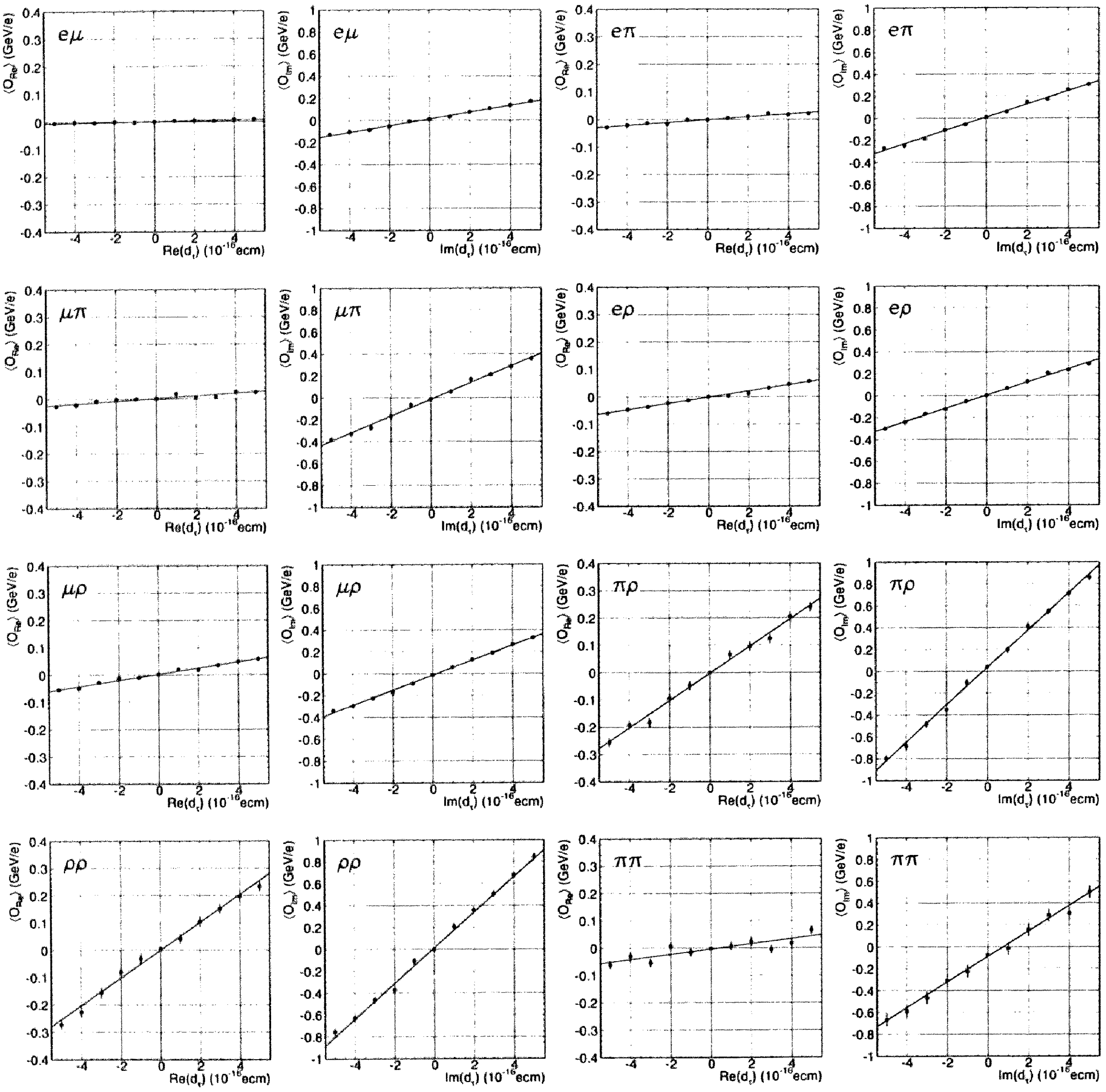

Figure 5.12: Correlation between $\langle \mathcal{O} \rangle$ and d_τ for each final-state mode obtained by MC. The line shows the fitted linear function.

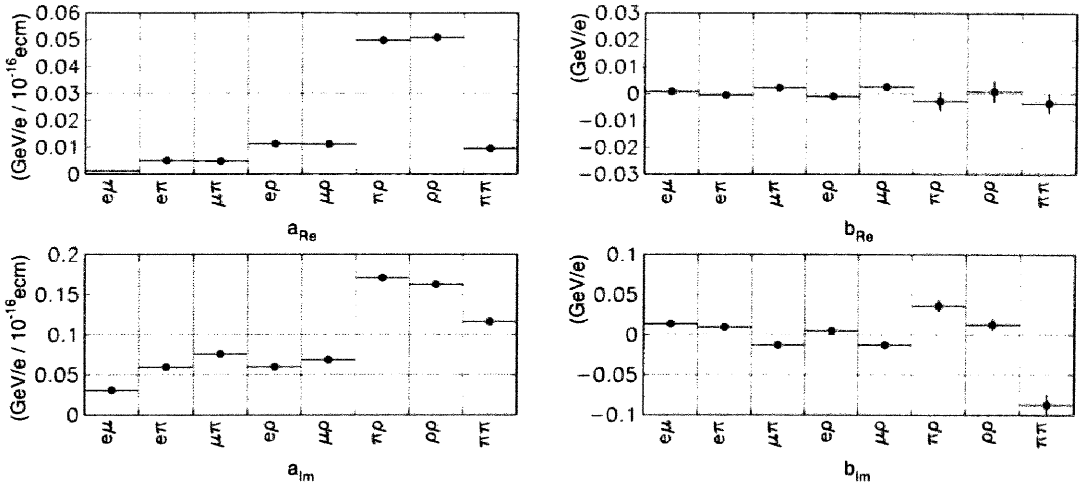

Figure 5.13: Conversion parameters, a and b, for each mode obtained by MC. The top figures show the parameters for $Re(d_\tau)$ and the bottom ones show the parameters for $Im(d_\tau)$. The errors are due to the MC statistics.

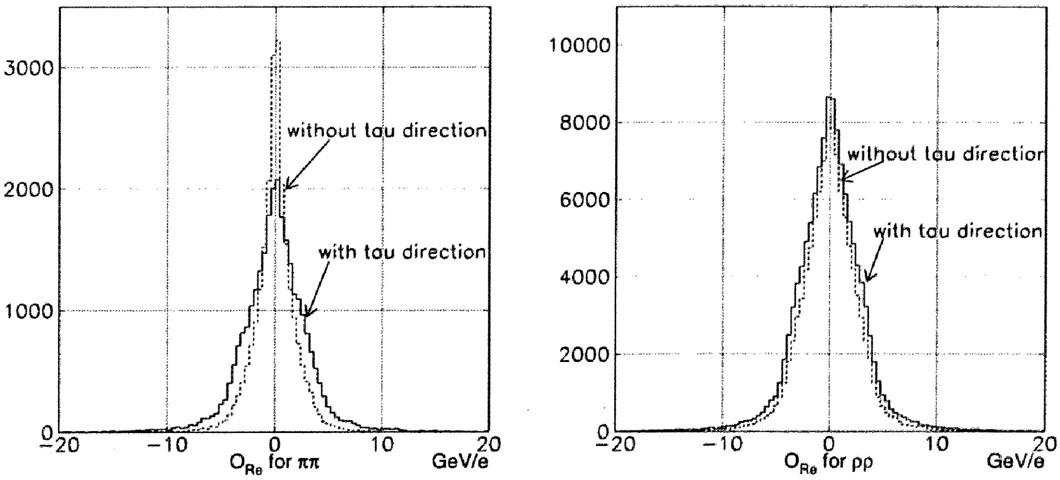

Figure 5.14: $\mathcal{O}_{Re}$ distribution for the $\pi\pi$(left) and the $\rho\rho$(right) mode, made by using the output of the MC generator. The solid line shows $\mathcal{O}_{Re}$ calculated with the generated τ direction, and the dashed line is $\mathcal{O}_{Re}$ averaged over the unknown τ direction.

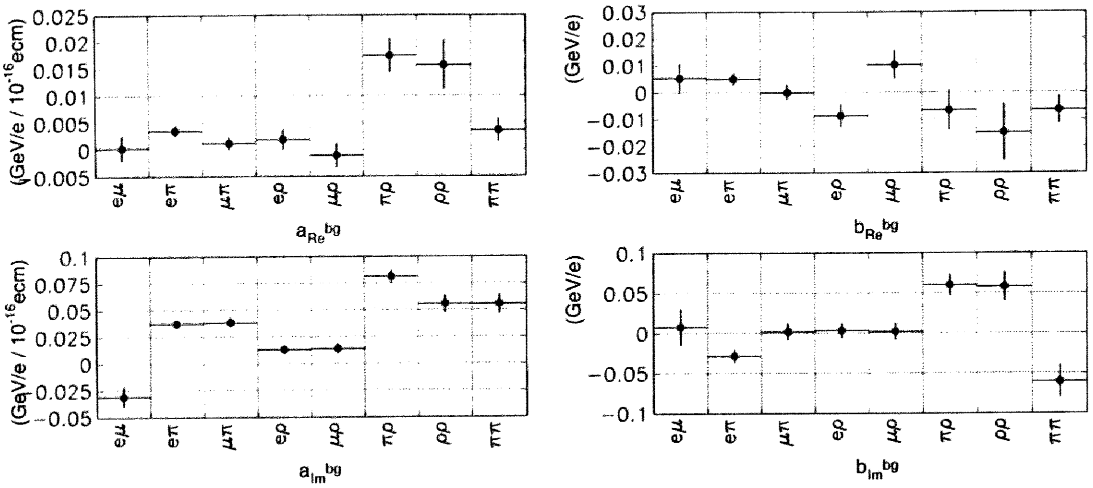

Figure 5.15: Parameters a^{bg} and b^{bg} for the misidentified background obtained by MC. The top figures show the parameters for $Re(d_\tau)$ and the bottom ones show the parameters for $Im(d_\tau)$. The errors are due to the MC statistics.

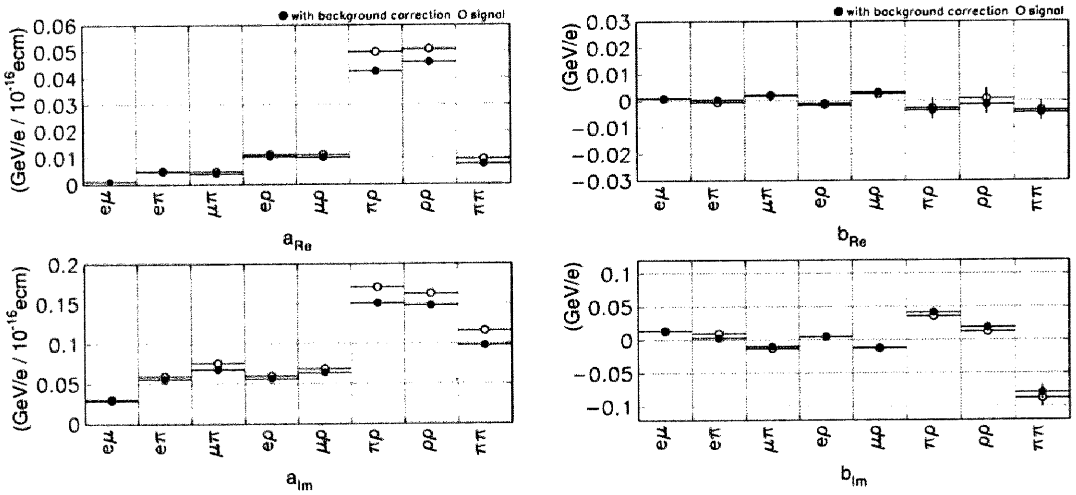

Figure 5.16: Parameters a^{eff} and b^{eff}. The top figures show the parameters for $Re(d_\tau)$ and the bottom ones show the parameters for $Im(d_\tau)$. The black points show the parameters with the background correction and the white points are parameters a and b for the signal. The errors are due to the MC statistics.

5.4 Systematic study

To evaluate any systematic uncertainties related to the MC simulation, various studies have been carried out as follows. The results are detailed in Tables 5.13, 5.14, 5.15 and 5.16.

5.4.1 Detector alignment

Detector alignment

To examine any artificial asymmetry attributed to the tracking systems, the $e^+e^- \to \mu^+\mu^-$ events are extracted and analyzed on their opening angles, $\Delta\theta = \theta^+ - \theta^- - \pi$ and $\Delta\phi = \phi^+ - \phi^- - \pi$, where $\theta^\pm$ and $\phi^\pm$ show polar and azimuthal angles of $\mu^\pm$ in the center-of-mass system. Because of the 2-body reaction, these angles should be zero, so that they can be a good indicator of symmetric alignment. We found $\Delta\theta = 1.48$ mrad and $\Delta\phi = 0.36$ mrad, as shown in Figure 5.17. These errors in the detector alignment yield non-zero residual values on the observables by less than 10% of the statistical errors.

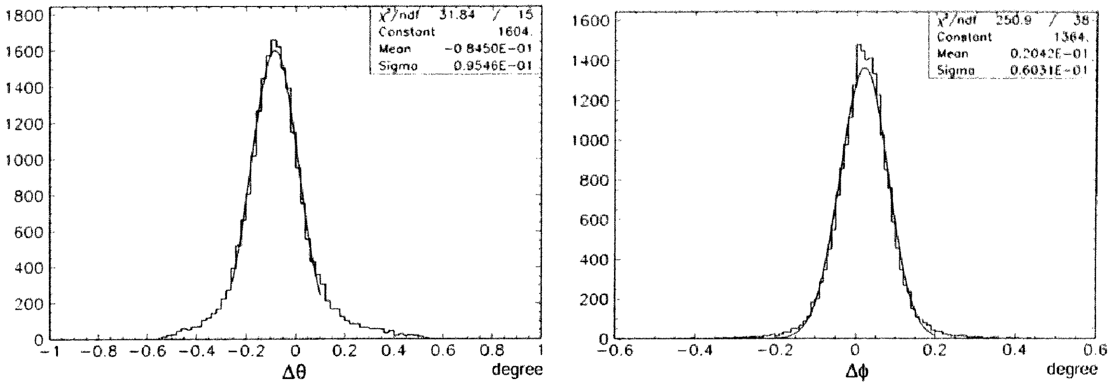

Figure 5.17: $\Delta\theta$(left) and $\Delta\phi$(right) distributions obtained from $e^+e^- \to \mu^+\mu^-$ events of exp.9.

Alignment between the detector and the beam pipe

The effect of a misalignment between the detector and the e^+e^- beam axis is studied by applying 5 mrad artificial rotations on the detector around the x-, y- and z-axes, and thus this effect is found to be negligible.

5.4.2 Momentum reconstruction

As shown in Figures 5.2 and 5.6, there are small differences between the data and MC, especially in the low-momentum region. They can be caused by imperfect momentum reconstruction, and could provide a systematic offset on the observables.

Charged track

The absolute value of the momentum reconstruction is examined. The difference in the ρ-meson mass peak between the data and MC, as shown in Figure 5.2, could indicate a possible deviation. It is represented by a scaling factor of 0.994, which yields a variation by about 10% of the statistical ones.

π^0

The effect of the π^0's momentum shift is studied by applying a scaling factor of 0.994 to the momentum. The result shows that the errors are about 10% of the statistical ones for the modes including $\rho^\pm$.

Photon Resolution

The difference in the π^0 mass resolution between the experimental data and MC is observed as shown in the $\gamma\gamma$ invariant mass distribution of Figure 5.6. This is due to a discrepancy of the photon energy resolution between the data and MC. Its difference is studied using the decay $D^{*0} \to D^0\gamma$ [33], whose result is listed in Table 5.10. By setting the photon energy to be $E'_\gamma = E_\gamma \pm \sigma$, where E'_γ is the scaled energy of a photon and σ is the 1σ difference listed in Table 5.10, the changes in the observables are extracted and then found to be about 10% of the statistical errors for the modes including $\rho^\pm$.

Table 5.10: Difference in the photon energy resolution as a function of the photon energy. σ^{data} and σ^{MC} are obtained from the mass-difference distribution between D^{*0} and D^0 in the decay $D^{*0} \to D^0\gamma$ for the data and MC events, respectively. The 1σ offset is calculated by $\sqrt{(\sigma^{\mathrm{data}})^2 - (\sigma^{\mathrm{MC}})^2}$.

E_γ (GeV)	σ^{data} (MeV/c^2)	σ^{MC} (MeV/c^2)	1σ offset (MeV)
0.10 - 0.15	4.275	4.015	1.468
0.15 - 0.20	5.05	3.932	3.169
0.20 - 0.25	4.704	3.764	2.821
0.25 - 0.30	4.23	3.652	2.134
0.30 - 0.40	4.206	3.454	2.400
0.40 - 0.50	3.711	3.035	2.135
0.50 - 0.60	3.682	2.692	2.512
0.60 -	3.015	2.632	1.471

5.4.3 Efficiency

The detector response is different between the positive and negative particle charges, especially concerning electron and pion identification; such differences cause an asymmetry to the observables.

Charge asymmetry

The ratios of the yields for the charge-conjugated states, $N(A^+B^-)/N(A^-B^+)$, are compared between the data and MC, and about or less than a 1% difference is found, as shown in Table 5.11.

An efficiency variation of ±1% leads to a large systematic shift in the offset of the imaginary part, amounting to the same size as the statistical error. The effects on the other parameters are negligible. The observables of the imaginary part are the sum of the asymmetric distributions over the different charge combinations, as shown in Figure 5.18. Therefore, the charge asymmetry directly affects $\langle \mathcal{O}_{Im} \rangle$, and causes a significant systematic error.

Table 5.11: Ratios of the yields, $N(A^+B^-)/N(A^-B^+)$, for the data and MC.

mode	data	MC
$e\mu$	0.999 ± 0.004	1.004 ± 0.001
$e\pi$	0.996 ± 0.005	0.989 ± 0.002
$\mu\pi$	0.985 ± 0.006	0.995 ± 0.002
$e\rho$	1.016 ± 0.004	1.008 ± 0.001
$\mu\rho$	0.999 ± 0.004	1.012 ± 0.001
$\pi\rho$	1.014 ± 0.006	1.024 ± 0.002

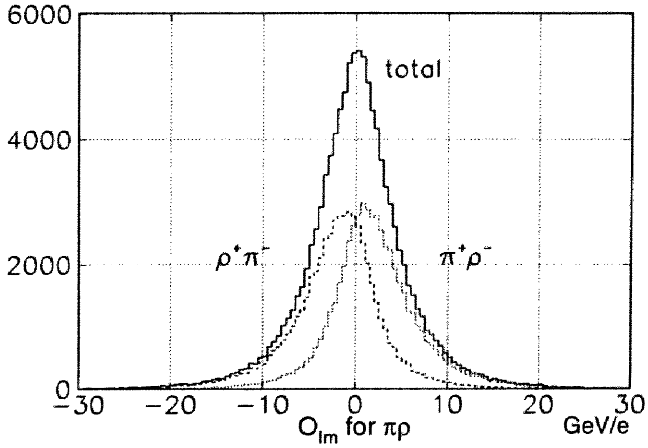

Figure 5.18: $\mathcal{O}_{Im}$ distribution in the $\pi\rho$ mode. The solid line shows the total sample, the dashed line is for the $\rho^+\pi^-$ mode and the dotted line is for the $\pi^+\rho^-$ mode.

Efficiency curve

The systematic effect of the efficiencies, depending on the kinematical variables, is also studied, because a difference in the distribution between the data and MC is observed, as shown Figures 5.7 and 5.8. The ratios of the number of positive and negative charged tracks as a function of $\cos\theta_{\mathrm{lab}}$ and the momentum in the laboratory frame are also examined, as shown in Figures 5.19 and 5.20. Although the consistency of the data and MC seems to be satisfactory, there are some differences, which are probably due to the reconstruction efficiency. The effect of this misunderstanding on the observables is checked by re-weighting the MC samples. The weight functions are constructed bin-by-bin from the ratio of the data to MC for the momentum and $\cos\theta$ distributions, and independently of the charge. The result shows the systematic uncertainties to be about 50% of the statistical errors.

5.4.4 Background

Fake rate

The different estimates of the sample purity between the data and MC yields a systematic error of the sensitivities and offsets. Since the difference in the yields between the data and

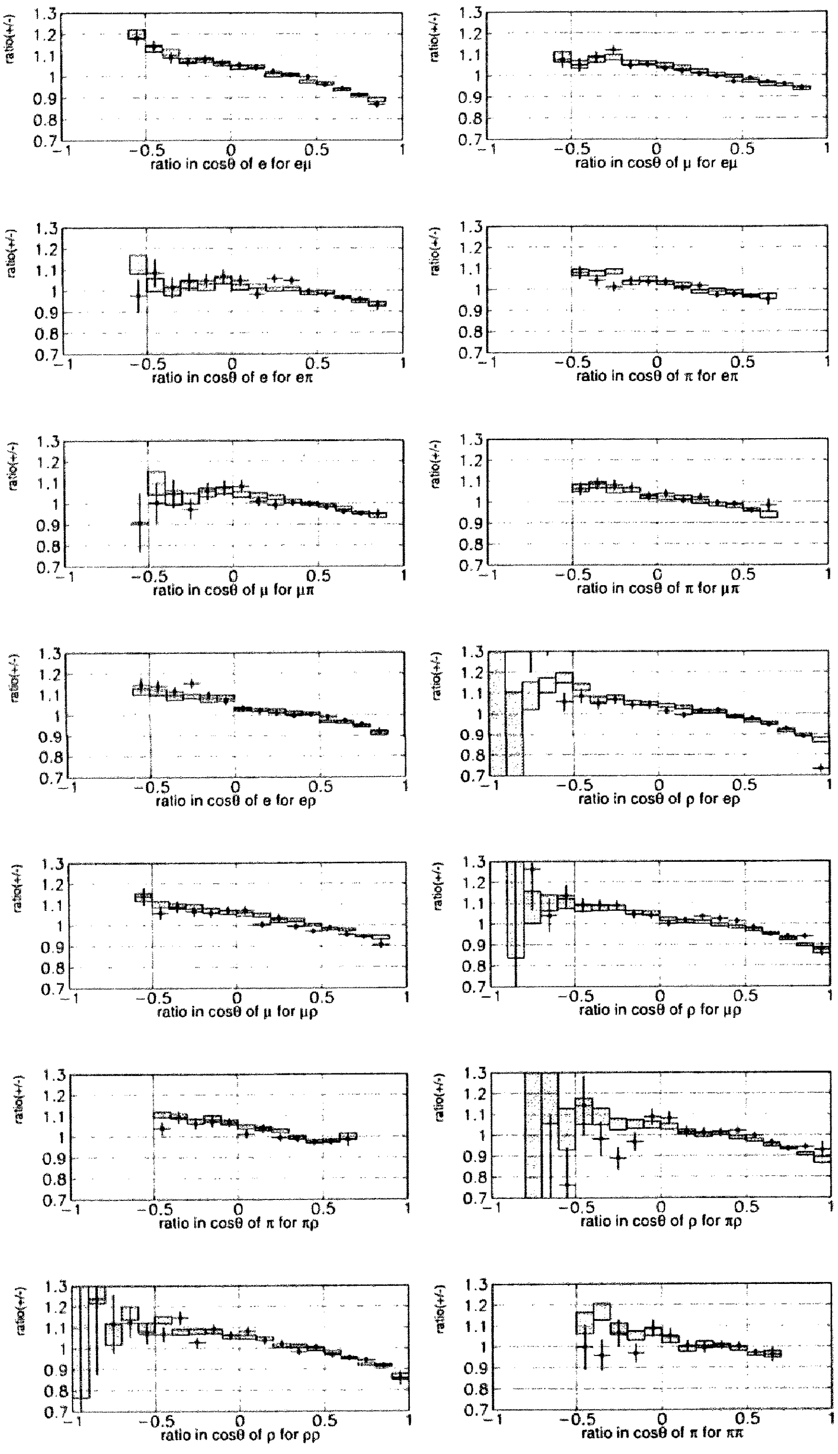

Figure 5.19: Ratio of the number of positive and negative charge tracks in each bin for the $\cos\theta_{\rm lab}$ distribution. The dots are the experimental data and the boxes are the MC expectation.

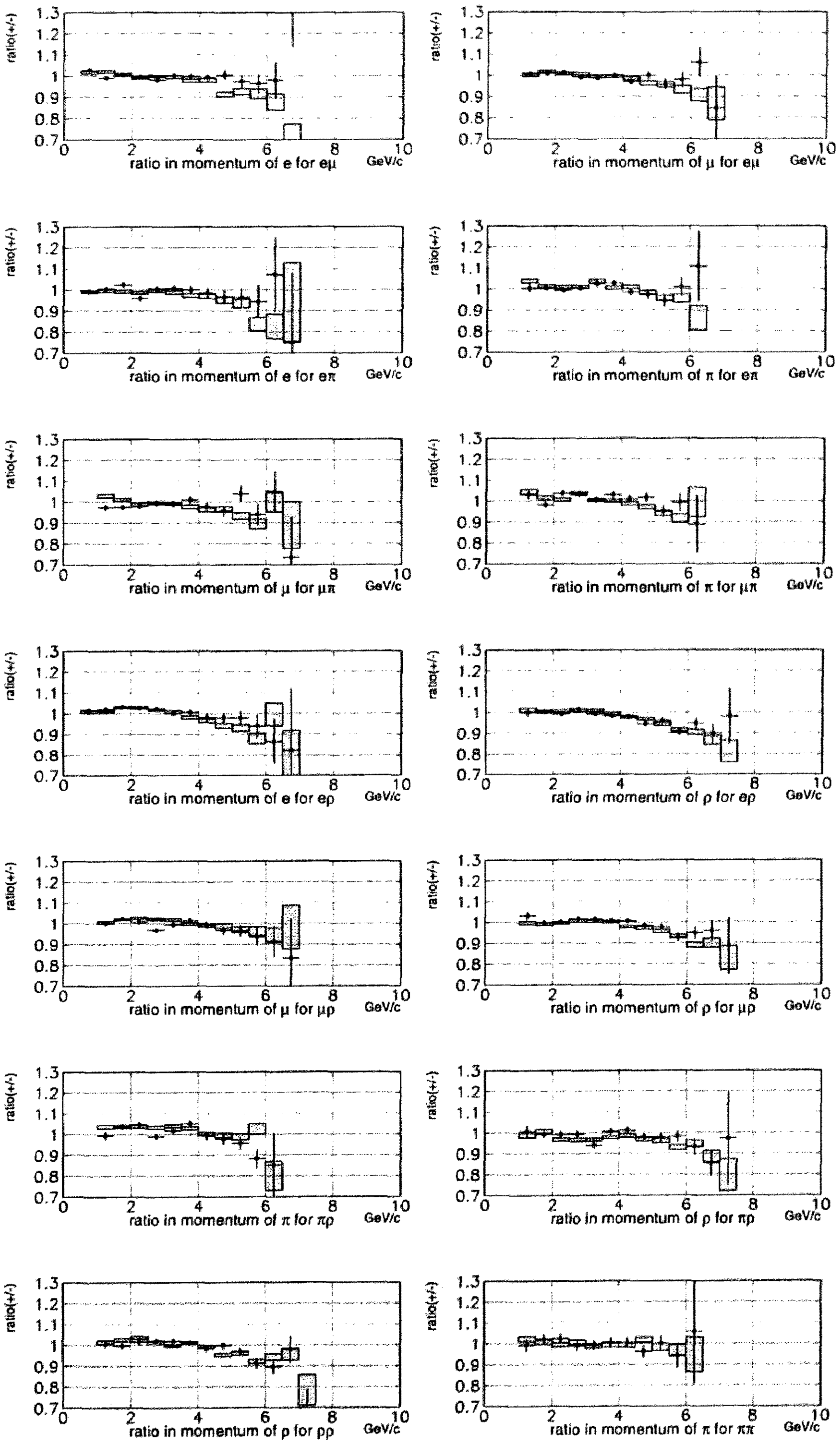

Figure 5.20: Ratios of the number of positive and negative charge tracks in each bin for the momentum distribution in the laboratory frame. The dots are the experimental data and the boxes are the MC expectation.

MC expectation is found to be about 10%, the uncertainty in the background fraction is assumed conservatively to be 10% of the yields, $\Delta n_{\rm bg} = 0.10 \cdot N$; the systematic errors are thus found to be about 10% or less for the sensitivities and about 20% of the statistical errors of the observables for the offsets.

MC statistics

Because the statistics of the background MC is not very large, the statistical error of the background correction parameters is not small. However, the resulting error is greatly reduced due to the small background rate. In this analysis, the statistical error of the background correction is also included in the statistical error of the parameters $a^{\rm eff}$ and $b^{\rm eff}$. The calculated error is about 20% - 50% of the total statistical error of the parameters.

5.4.5 Effect of the initial-state radiation

The effect of the radiations in calculating the amplitudes is ignored because it needs much computing power for the analysis program, although its effect is considered for MC event generation. In order to check the effect of radiation, the effect is introduced into the calculation, and only MC with zero EDM and data are analyzed. The average of the observable is calculated in almost the same way as the default analysis, but including the ambiguity of radiation, as follows: a) The momentum of the initial-state radiation is generated randomly by the KORALB generator. b) All momenta are boosted from the center-of-mass frame into the τ-pair rest frame while assuming that the initial-state radiation comes from the e^+e^- beam. c) In this frame, the observables are calculated. For each event, the above process is iterated 500 times using the hit-and-miss approach, and with successful tries the average value of the observable is found.

Figure 5.21 shows the resulting $\langle \mathcal{O}_{Re} \rangle$ and $\langle \mathcal{O}_{Im} \rangle$ of the data and τ-pair MC with zero EDM. The results with and without the initial-radiation effect are consistent with each other. The shift of $\langle \mathcal{O}_{Re} \rangle$ and $\langle \mathcal{O}_{Im} \rangle$ between with and without the initial radiation gives an estimate of the systematic effect of ignoring the radiation. Since this systematic shift occurs in analyses of both data and MC, it is already taken into account in the analysis (up to the effects of the detector and/or background mismodelling), so the estimate is conservative. As shown in Table 5.12, this shift for all modes, apart from $\pi\pi$, is negligibly small.

Other checks for the effect of the radiation to the parameters are described in Appendix F. The contribution from the final-state radiation is negligibly small. Therefore, its effect is ignored in the above-mentioned study.

Table 5.12: Shift of $\langle \mathcal{O}_{Re} \rangle$ and $\langle \mathcal{O}_{Im} \rangle$ between with and without the radiation effect and the systematic errors. The units are GeV/e.

	$e\mu$	$e\pi$	$\mu\pi$	$e\rho$	$\mu\rho$	$\pi\rho$	$\rho\rho$	$\pi\pi$
Shift of $\langle \mathcal{O}_{Re} \rangle$	0.0001	0.0002	0.0001	0.0001	0.0001	0.0008	0.0000	0.0012
Sys. err. of $\langle \mathcal{O}_{Re} \rangle$	0.0010	0.0029	0.0030	0.0015	0.0019	0.0092	0.0079	0.0035
Shift of $\langle \mathcal{O}_{Im} \rangle$	0.0013	0.0011	0.0007	0.0005	0.0004	0.0026	0.0007	0.0024
Sys. err. of $\langle \mathcal{O}_{Im} \rangle$	0.0132	0.0249	0.0297	0.0071	0.0063	0.0239	0.0160	0.0413

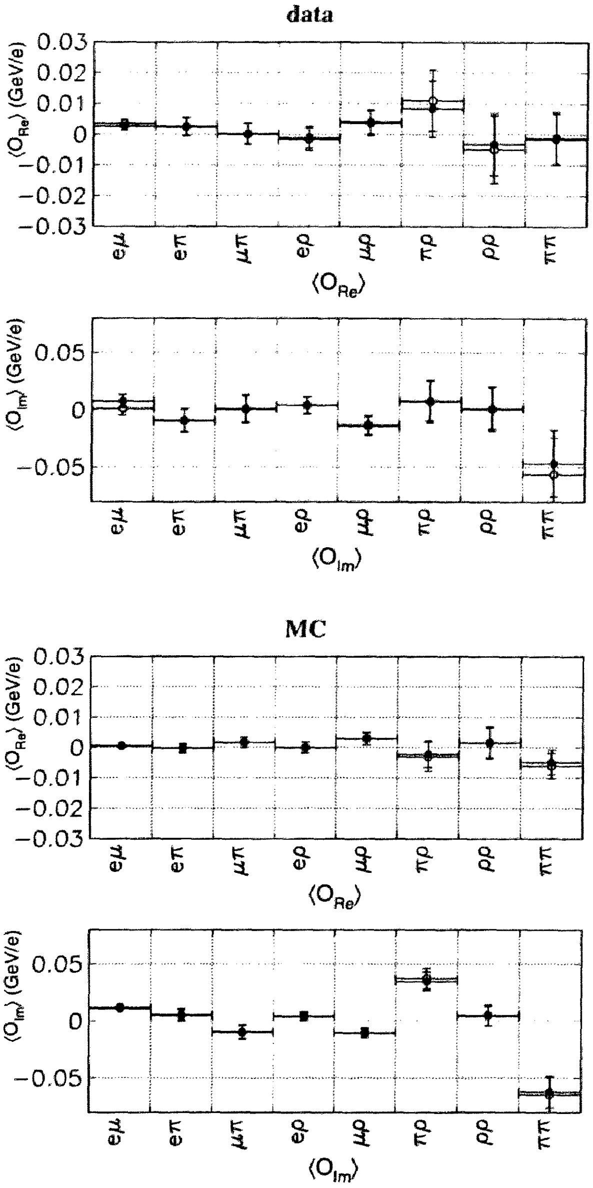

Figure 5.21: Mean values of the observable for the data and the τ-pair MC of zero EDM. The black points show the result calculated with the initial radiation effects and the white circles show the result of the default analysis.

5.4.6 Observable distribution

As described in Section 3.2, the sensitivity directly correlates with the width of the observable. Therefore, the shape of the observable is inspected. Figure 5.22 shows the "pull" distribution for the observables obtained as in Figure 5.11. The "pull" is the residual value normalized by its error, defined as

$$\text{pull} = \frac{N_{\text{data}} - N_{\text{MC}}}{\sqrt{\sigma_{\text{data}}^2 + \sigma_{\text{MC}}^2}},$$

where N_{data} and N_{MC} are the number of events in each bin and σ_{data} and σ_{MC} are its errors for the data and MC. In this plot, MC is made with a zero EDM. The figures show the flat distributions, which indicates that the observed mean values are very close to zero and the MC simulation reproduces the sensitivity well.

5.4.7 Run dependence

In order to examine the data stability, the run dependence of the observables is plotted in Figure 5.23 with the χ^2 values calculated along with the total mean values. The samples are divided into every 50 runs. The systematic errors are not included in the error bars. The fluctuations seem to be statistical.

5.4.8 Cut dependence

As shown in Figure 5.7, a clear difference between the data and MC exists at around the low-momentum regions of the electrons and pions. This region may produce large offsets of the observables because of some unconsidered reason. In order to examine an effect of this difference on the observables, the low-momentum events are removed by applying a cut of $P_{\text{lab.}} > 1.5$ GeV/c for the electrons and $P_{\text{lab.}} > 2.0$ GeV/c for the pions. The results are shown in Figure 5.24. The results of $\langle \mathcal{O}_{Re} \rangle$ and $\langle \mathcal{O}_{Im} \rangle$ for the remaining and removed events are consistent with each other and with null EDM within 2-sigma errors.

The polar angle dependence of the observables is also studied in a similar way as mentioned above by applying $\cos\theta$ cuts: $-0.60 < \cos\theta_{\text{lab.}} < 0.83$ and $-0.50 < \cos\theta_{\text{lab.}} < 0.62$. The results are given in Figures 5.25 and 5.26. These results also show the statistical consistency.

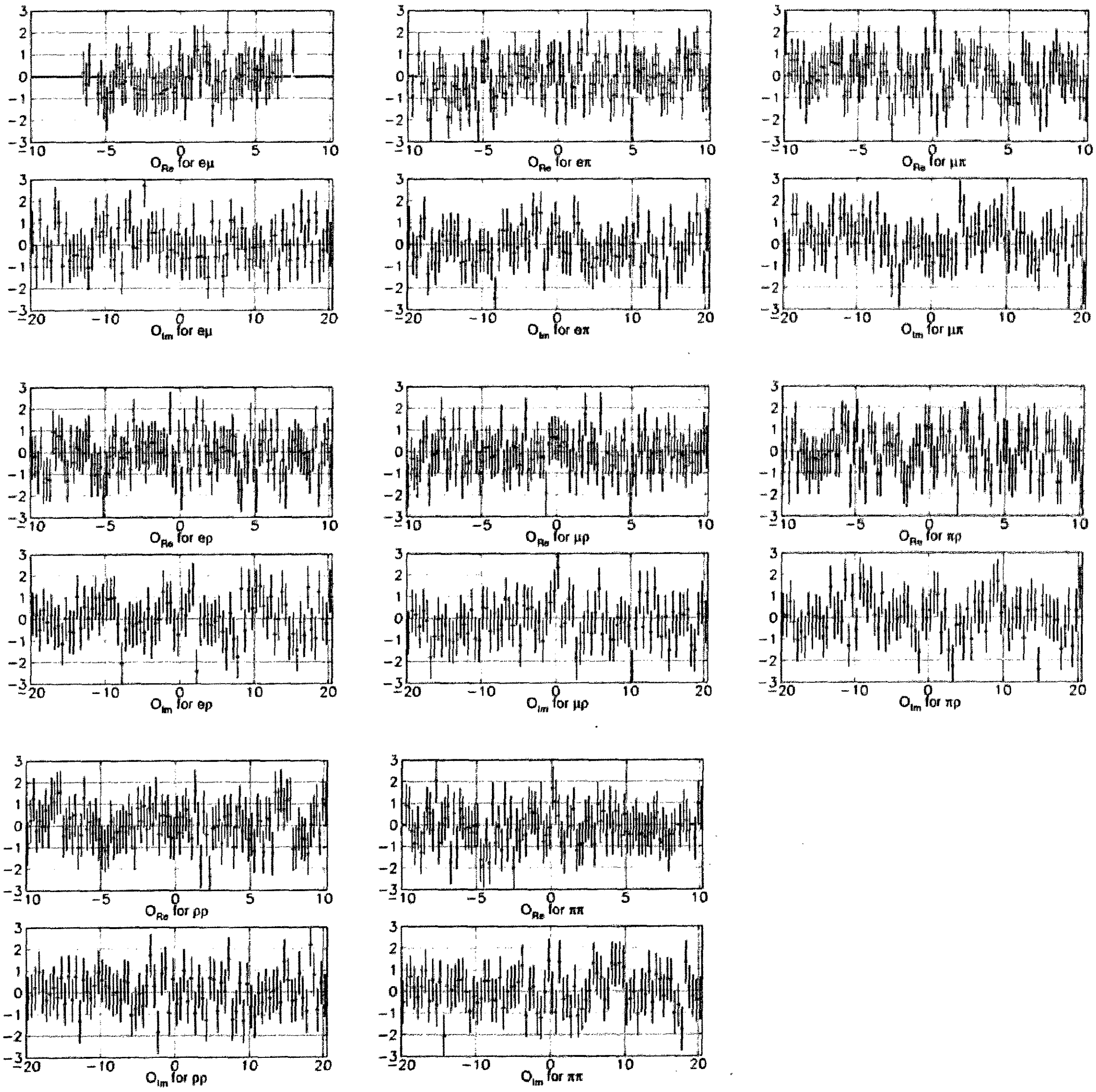

Figure 5.22: "pull" distribution of observables. The top figures of each mode show $\mathcal{O}_{Re}$ and bottom ones show $\mathcal{O}_{Im}$.

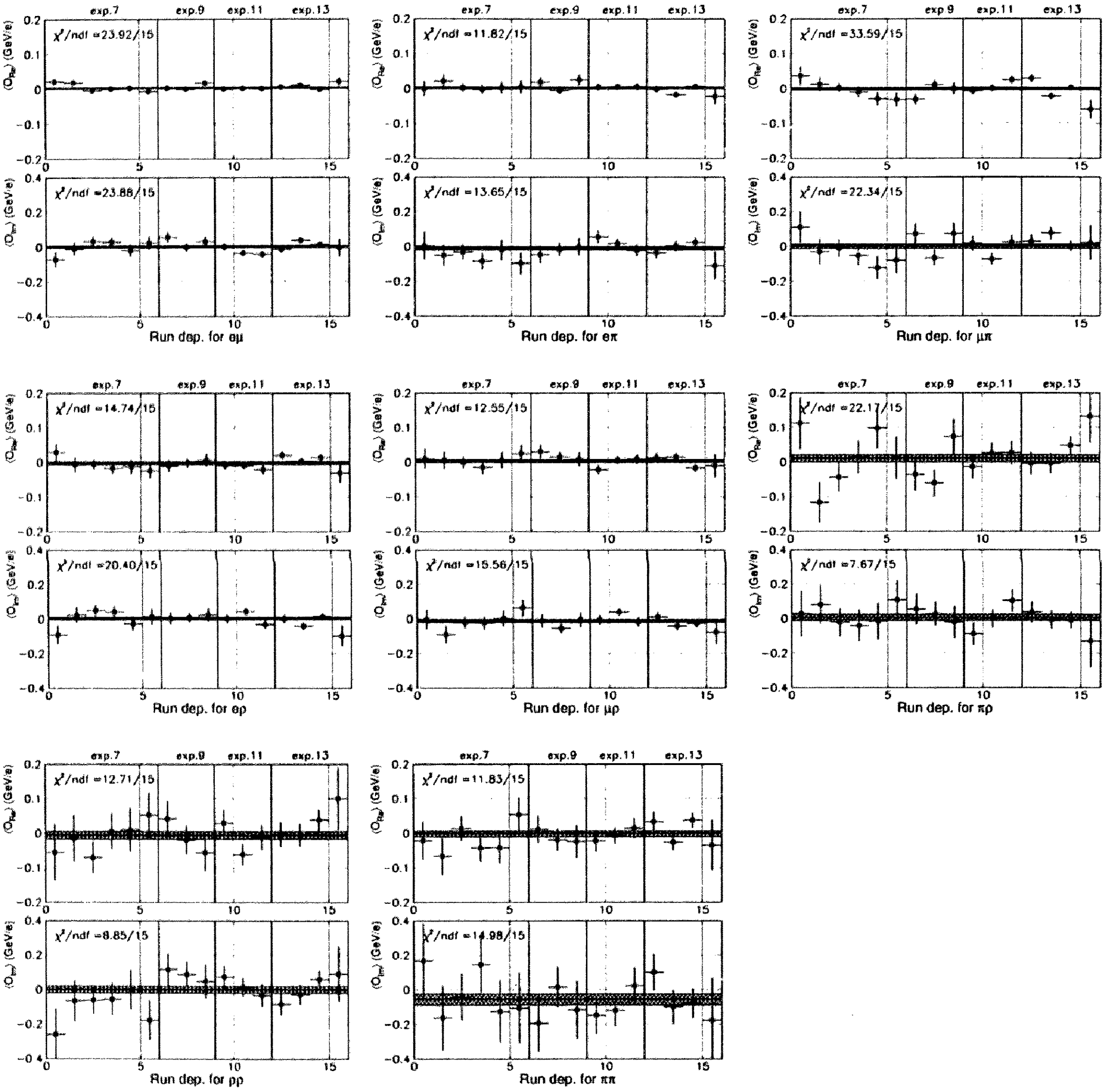

Figure 5.23: Run dependence of $\langle \mathcal{O}_{Re} \rangle$ (top) and $\langle \mathcal{O}_{Im} \rangle$ (bottom) for each mode. The hatched box shows the total mean value with $\pm 1\sigma$ statistical errors.

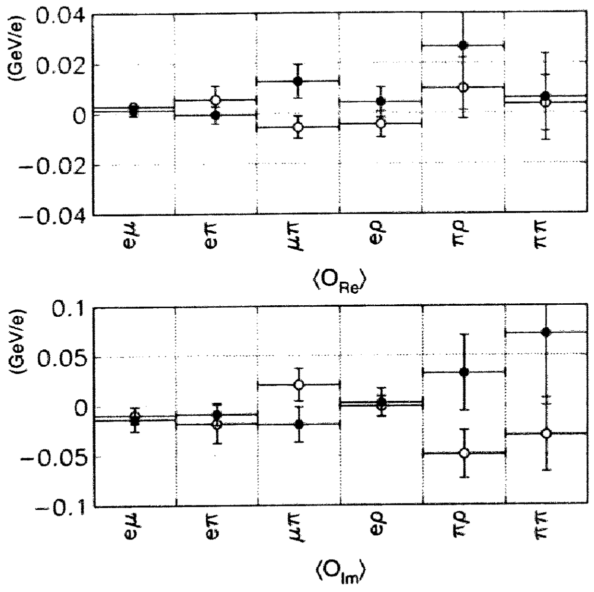

Figure 5.24: Momentum-cut dependence of $\langle\mathcal{O}_{Re}\rangle$ (top) and $\langle\mathcal{O}_{Im}\rangle$ (bottom) for each mode. The dots are the result of the default criteria and the momentum cut of $P_{\mathrm{lab.}} > 1.5$ GeV/c for the electrons and $P_{\mathrm{lab.}} > 2.0$ GeV/c for the pions. The circles are the result of the default criteria and rejected events by the above-mentioned criteria. The error bars show the statistical errors.

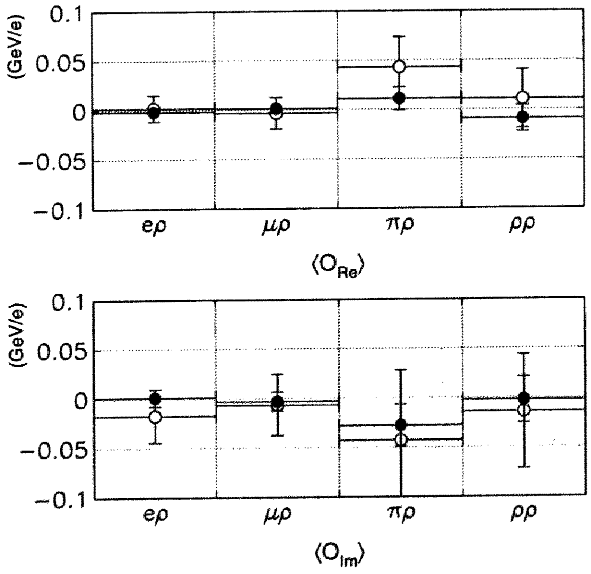

Figure 5.25: $\cos\theta_{\mathrm{lab.}}$ cut dependence of $\langle\mathcal{O}_{Re}\rangle$ (top) and $\langle\mathcal{O}_{Im}\rangle$ (bottom) for each mode. The dots are the result of the default criteria and $-0.60 < \cos\theta_{\mathrm{lab.}} < 0.83$. The circles are the default criteria and rejected events by the above-mentioned criteria. The errors do not include systematic errors.

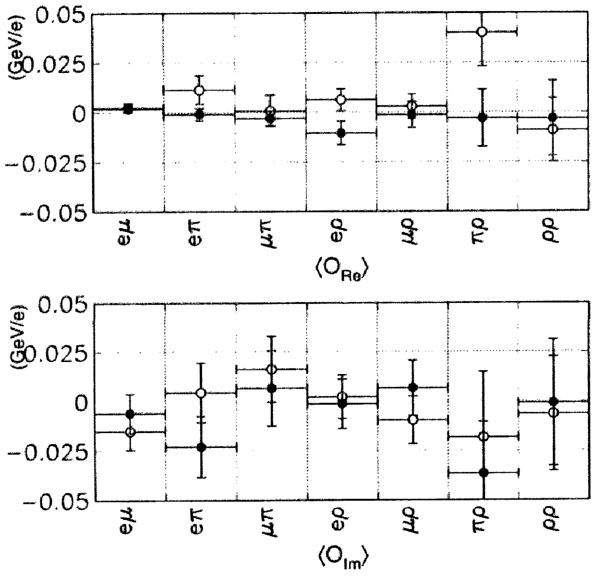

Figure 5.26: $\cos\theta_{\mathrm{lab}}$. cut dependence of $\langle \mathcal{O}_{Re} \rangle$ (top) and $\langle \mathcal{O}_{Im} \rangle$ (bottom) for each mode. The dots are the result of the default criteria and $-0.50 < \cos\theta_{\mathrm{lab}} < 0.62$. The circles are the default criteria and rejected events based on the above criteria. The errors do not include systematic errors.

Table 5.13: Systematic errors for $\langle \mathcal{O}_{Re} \rangle$ and b^{eff}_{Re}. The units are GeV/e.

	$e\mu$	$e\pi$	$\mu\pi$	$e\rho$	$\mu\rho$	$\pi\rho$	$\rho\rho$	$\pi\pi$
Detector alignment	0.0000	0.0001	0.0000	0.0000	0.0001	0.0004	0.0007	0.0002
Momentum reconst.								
Charged track	0.0001	0.0004	0.0010	0.0004	0.0002	0.0004	0.0014	0.0035
π^0	0.0000	0.0000	0.0000	0.0001	0.0005	0.0023	0.0011	0.0000
Photon resolution	0.0001	0.0002	0.0001	0.0001	0.0003	0.0004	0.0006	0.0000
Efficiency								
Charge asymmetry	0.0000	0.0000	0.0000	0.0001	0.0001	0.0002	0.0000	0.0000
Momentum	0.0005	0.0015	0.0022	0.0003	0.0015	0.0065	0.0062	0.0003
$\cos\theta$	0.0007	0.0023	0.0019	0.0011	0.0002	0.0061	0.0043	0.0004
Background								
Fake rate	0.0005	0.0006	0.0002	0.0008	0.0008	0.0004	0.0016	0.0003
Radiative effects	0.0001	0.0002	0.0001	0.0001	0.0001	0.0008	0.0000	0.0012
Total	0.0010	0.0029	0.0030	0.0015	0.0019	0.0093	0.0079	0.0037
Stat. error of $\langle \mathcal{O}_{Re} \rangle$	0.0013	0.0032	0.0037	0.0038	0.0042	0.0111	0.0118	0.0103
MC stat. error of b^{eff}_{Re}	0.0005	0.0010	0.0012	0.0013	0.0014	0.0034	0.0038	0.0030

Table 5.14: Systematic errors for a^{eff}_{Re}. The units are GeV/e/$10^{-16} e\,$cm.

	$e\mu$	$e\pi$	$\mu\pi$	$e\rho$	$\mu\rho$	$\pi\rho$	$\rho\rho$	$\pi\pi$
Background								
Fake rate	0.0001	0.0002	0.0004	0.0009	0.0012	0.0032	0.0035	0.0006
Sensitivity a^{eff}_{Re}	0.0011	0.0048	0.0041	0.0106	0.0102	0.0426	0.0460	0.0077
MC stat. error of a^{eff}_{Re}	0.0002	0.0004	0.0005	0.0005	0.0006	0.0014	0.0016	0.0012

Table 5.15: Systematic errors for $\langle \mathcal{O}_{Im} \rangle$ and b^{eff}_{Im}. The units are GeV/e.

	$e\mu$	$e\pi$	$\mu\pi$	$e\rho$	$\mu\rho$	$\pi\rho$	$\rho\rho$	$\pi\pi$
Detector alignment	0.0004	0.0016	0.0016	0.0004	0.0005	0.0026	0.0016	0.0053
Momentum reconst.								
Charged track	0.0007	0.0016	0.0040	0.0000	0.0007	0.0027	0.0055	0.0043
π^0	0.0000	0.0000	0.0000	0.0000	0.0008	0.0001	0.0018	0.0000
Photon resolution	0.0003	0.0005	0.0007	0.0002	0.0005	0.0012	0.0013	0.0000
Efficiency								
Charge asymmetry	0.0038	0.0244	0.0292	0.0011	0.0059	0.0225	0.0000	0.0000
Momentum	0.0124	0.0012	0.0009	0.0066	0.0007	0.0011	0.0104	0.0023
$\cos\theta$	0.0017	0.0003	0.0031	0.0023	0.0006	0.0067	0.0095	0.0405
Background								
Fake rate	0.0006	0.0038	0.0015	0.0002	0.0015	0.0024	0.0046	0.0027
Radiative effect	0.0013	0.0011	0.0007	0.0005	0.0004	0.0026	0.0007	0.0024
Total	0.0132	0.0249	0.0298	0.0071	0.0063	0.0240	0.0160	0.0413
Stat. error of $\langle \mathcal{O}_{Im} \rangle$	0.0061	0.0112	0.0134	0.0077	0.0085	0.0209	0.0207	0.0377
MC stat. error of b^{eff}_{Im}	0.0021	0.0036	0.0042	0.0026	0.0029	0.0063	0.0066	0.0109

Table 5.16: Systematic errors for a^{eff}_{Im}. The units are GeV/e/$10^{-16}e\,\mathrm{cm}$.

	$e\mu$	$e\pi$	$\mu\pi$	$e\rho$	$\mu\rho$	$\pi\rho$	$\rho\rho$	$\pi\pi$
Background								
Fake rate	0.0061	0.0022	0.0038	0.0047	0.0055	0.0090	0.0107	0.0061
Sensitivity a^{eff}_{Im}	0.0289	0.0559	0.0681	0.0564	0.0640	0.1510	0.1481	0.0982
MC stat. error of a^{eff}_{Im}	0.0009	0.0015	0.0018	0.0011	0.0012	0.0027	0.0028	0.0047

5.5 Result

The resulting EDM values are listed in Table 5.17 and plotted in Figure 5.27. The parameter errors due to the MC statistics are included in the statistical errors. By adding the statistical and systematic errors quadratically, the weighted mean values of the real and imaginary parts of the electric dipole moment are obtained as

$$Re(d_\tau) = (1.15 \pm 1.70) \times 10^{-17} e\,\mathrm{cm}, \tag{5.3}$$

$$Im(d_\tau) = (-0.83 \pm 0.86) \times 10^{-17} e\,\mathrm{cm}. \tag{5.4}$$

The 95% confidence level limits provide

$$-2.2 < Re(d_\tau) < 4.5 \quad (10^{-17} e\,\mathrm{cm}), \tag{5.5}$$

$$-2.5 < Im(d_\tau) < 0.8 \quad (10^{-17} e\,\mathrm{cm}). \tag{5.6}$$

The upper limits in terms of the absolute values of d_τ are

$$|Re(d_\tau)| < 4.0 \times 10^{-17} e\,\mathrm{cm}, \tag{5.7}$$

$$|Im(d_\tau)| < 2.2 \times 10^{-17} e\,\mathrm{cm}, \tag{5.8}$$

at 95% confidence level.

Table 5.17: Resulting electric dipole moment. The first error is statistical and the second one is systematic.

mode	$Re(d_\tau)$ ($10^{-16} e\,\mathrm{cm}$)	$Im(d_\tau)$ ($10^{-16} e\,\mathrm{cm}$)
$e\mu$	$2.25 \pm 1.26 \pm 0.93$	$-0.41 \pm 0.22 \pm 0.46$
$e\pi$	$0.43 \pm 0.64 \pm 0.60$	$-0.22 \pm 0.19 \pm 0.45$
$\mu\pi$	$-0.41 \pm 0.87 \pm 0.74$	$0.15 \pm 0.19 \pm 0.44$
$e\rho$	$0.00 \pm 0.36 \pm 0.14$	$-0.01 \pm 0.14 \pm 0.13$
$\mu\rho$	$0.04 \pm 0.42 \pm 0.18$	$-0.02 \pm 0.14 \pm 0.10$
$\pi\rho$	$0.34 \pm 0.25 \pm 0.22$	$-0.22 \pm 0.13 \pm 0.16$
$\rho\rho$	$-0.08 \pm 0.25 \pm 0.17$	$-0.12 \pm 0.14 \pm 0.11$
$\pi\pi$	$0.42 \pm 1.17 \pm 0.48$	$0.24 \pm 0.34 \pm 0.42$

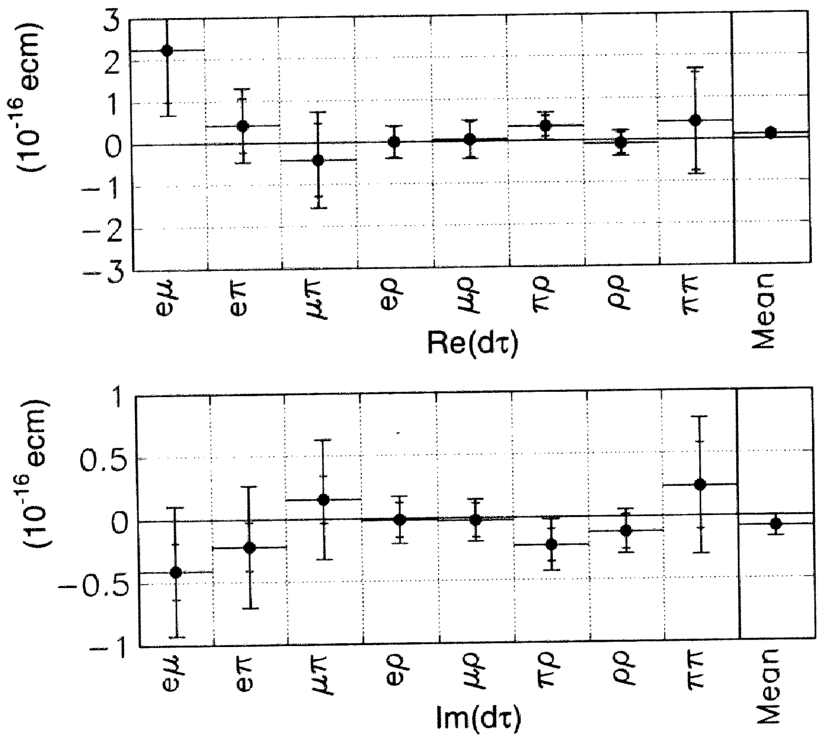

Figure 5.27: $Re(d_\tau)$ and $Im(d_\tau)$ for each mode. The errors are both statistical and the systematic. The error bars with small ticks show the statistical errors.

5.6 Comparisons with other experiment

The best existing bound on EDM comes from an indirect measurement based on the relationship $|d_\tau| = \cot\theta_W |d_\tau^W|$, derived using the effective Lagrangian approach [34]. Using the weak electric dipole moment, $|d_\tau^W| < 5.8 \times 10^{-18} e\,\mathrm{cm}$, measured at LEP [35], an upper limit of $|d_\tau| < 1.1 \times 10^{-17} e\,\mathrm{cm}$ is extracted at the 95% confidence level.

A very strict constraint, $|d_\tau| < 2.2 \times 10^{-25} e\,\mathrm{cm}$, has also been derived from the experimental limits on a branching fraction of $\mu \to e\gamma$ decay [36]. Note, however, that this result relies on a particular ansatz for the lepton mixing matrix. In a recent preprint [37], other authors have argued that the same constraint may be derived under weaker assumptions.

Experimental measurements, on the other hand, have so far been performed at LEP and by ARGUS. At LEP, the L3 [4] and OPAL [5] groups have searched for the EDM effect in terms of the energy and the angular distribution of the radiated gamma in the process $e^+e^- \to \tau^+\tau^-\gamma$ on the Z^0 pole. Their results are $-3.1 < d_\tau < 3.1 (10^{-16} e\,\mathrm{cm})$ and $|d_\tau| < 3.7 \times 10^{-16} e\,\mathrm{cm}$ for L3 and OPAL, respectively. The ARGUS group [6] analyzed the $e^+e^- \to \tau^+\tau^-$ production in using essentially the same method as that used in this thesis, and set limits of $|Re(d_\tau)| < 4.6 \times 10^{-16} e\,\mathrm{cm}$ and $|Im(d_\tau)| < 1.8 \times 10^{-16} e\,\mathrm{cm}$.

Our experiment has successfully improved the upper limit on d_τ by a factor of 10 compared to the above-mentioned previous experimental measurements, and reached the same sensitivity as the indirect measurement. This is not only due to a 100-times larger statistics, but also to very-well-controlled systematic uncertainties in extracting d_τ, especially concerning the influence of acceptance variations.

The ARGUS group extracted the EDM using a relation described in Section 3.2, which is approximately given as

$$Re(d_\tau) = \frac{\langle \mathcal{O}_{Re} \rangle}{\langle \mathcal{O}_{Re}^2 \rangle}, \quad Im(d_\tau) = \frac{\langle \mathcal{O}_{Im} \rangle}{\langle \mathcal{O}_{Im}^2 \rangle}, \tag{5.9}$$

along with the use of the properties of the CP asymmetric quantities,

$$\int \mathcal{M}_{Re}^2 d\phi = \int \mathcal{M}_{Im}^2 d\phi = 0, \tag{5.10}$$

while ignoring the acceptance effect. The acceptance effect has been considered in the systematic error in the ARGUS analysis, and has been estimated to be about 0.4 - $1.0 \times 10^{-16} e\,\mathrm{cm}$.

Figure 5.28 shows a comparison between the sensitivity, a, and the mean of squared observable, $\langle \mathcal{O}^2 \rangle$, which corresponds to the sensitivity for the ARGUS analysis. These differences should be mainly caused by the acceptance cut and should make the systematic error. In this analysis, in order to reduce the systematic uncertainty due to the acceptance, and to treat the offset effect due to the forward/backward asymmetric event selection, the conversion parameters in Eq.(3.3) are made by a large number of MC samples with the detector simulation and the event selection. Therefore, the acceptance effect is automatically included into the conversion from the observable to d_τ, and the systematic error due to the acceptance is greatly reduced to be about one order less than that of the ARGUS experiment.

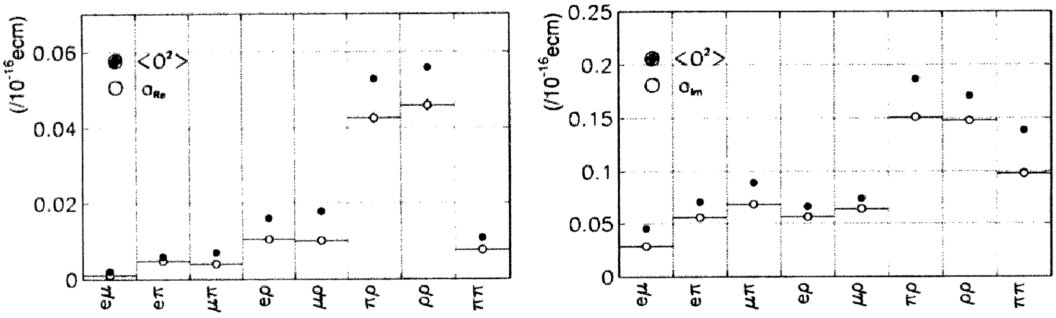

Figure 5.28: Comparison between the sensitivity, a, and the mean of squared observable, $\langle \mathcal{O}^2 \rangle$, for the real part (left) and the imaginary part (right) in the analysis. The circles show the sensitivities, a, and dots are $\langle \mathcal{O}^2 \rangle$.

Chapter 6

Conclusion

The electric dipole moment of the τ lepton was measured in such a way as to search for the CP-violation signature in the lepton sector. 26.8 million τ-pair events are used in this analysis, which are accumulated with the Belle detector at the KEKB accelerator at $\sqrt{s} = 10.58$ GeV. Eight different final-states in the decay of τ-pairs ($(e\nu\bar{\nu})(\mu\nu\bar{\nu})$, $(e\nu\bar{\nu})(\pi\nu)$, $(\mu\nu\bar{\nu})(\pi\nu)$, $(e\nu\bar{\nu})(\rho\nu)$, $(\mu\nu\bar{\nu})(\rho\nu)$, $(\pi\nu)(\rho\nu)$, $(\rho\nu)(\rho\bar{\nu})$, and $(\pi\nu)(\pi\bar{\nu})$) are analyzed.

In order to obtain the maximum sensitivity to the EDM, the *optimal observable method* is adopted, which uses all experimentally available information of spin and momenta of the τ decays. To suppress the systematic uncertainties from the acceptance effects, the conversion parameters from the observables to the EDM are extracted using the full MC simulation with the EDM effect. Thus, the mostly affected uncertainty is from the mismatch between the data and MC.

The results show no evidence of CP-violation. All of the results are consistent with zero-EDM within the errors.

Finally, the mean values of $Re(d_\tau)$ and $Im(d_\tau)$ over the eight different modes weighted by quadratically summed statistical and systematic errors are obtained as

$$Re(d_\tau) = (1.15 \pm 1.70) \times 10^{-17} e\,\text{cm}, \tag{6.1}$$
$$Im(d_\tau) = (-0.83 \pm 0.86) \times 10^{-17} e\,\text{cm}, \tag{6.2}$$

with the following corresponding 95% confidence limits:

$$-2.2 < Re(d_\tau) < 4.5 \quad (10^{-17} e\,\text{cm}), \tag{6.3}$$
$$-2.5 < Im(d_\tau) < 0.8 \quad (10^{-17} e\,\text{cm}). \tag{6.4}$$

This investigation has successfully improved the sensitivity to the τ lepton's electric dipole moment by a factor of more than 10 compared to previous measurements. This is not only due to 100-times larger statistics, but also due to well-controlled systematic uncertainties.

In the future, we will accumulate much more data. Thus, the difficulty of this analysis lies in the MC simulation. We have to improve the reliability of the MC simulation in order to suppress the systematic uncertainties, and we need to increase more computing power to generate many MC events, depending on the statistics of the data. The determination of the τ direction by measuring the vertex will certainly improve the sensitivity.

Appendix A

Optimal observable method

The optimal observable method [21][22] is used for the analysis. In this section, how to form the optimal observable $\mathcal{O}$ is described.

A.1 Formalization

In the following, the differential cross section is denoted by

$$\Sigma(\phi)d\phi, \tag{A.1}$$

where ϕ represents the relevant phase-space variables (momentum, angle, polarization, etc). If the total differential cross section is expanded in terms of a small parameter, λ, the approximate function is given as

$$\Sigma(\phi) = \Sigma_0(\phi) + \lambda\Sigma_1(\phi). \tag{A.2}$$

The mean value of the observable $\langle\mathcal{O}(\lambda)\rangle$ can be expressed using a phase-space dependent function, $f(\phi)$, as

$$\langle\mathcal{O}(\lambda)\rangle \equiv \int f(\phi)\Sigma(\phi)d\phi \bigg/ \int \Sigma(\phi)d\phi\,. \tag{A.3}$$

The change, $\delta_{\mathcal{O}}$, due to the presence of λ is given by

$$\delta_{\mathcal{O}} \equiv \langle\mathcal{O}(\lambda)\rangle - \langle\mathcal{O}(0)\rangle = \lambda \int f(\phi)\Sigma_1(\phi)d\phi \bigg/ \int \Sigma d\phi\,. \tag{A.4}$$

Assuming $\langle\mathcal{O}(0)\rangle = 0$ in order to simplify, if n events are recorded, the error of $\langle\mathcal{O}\rangle$ is given by

$$\Delta\mathcal{O} = \sqrt{\frac{\int f^2\Sigma d\phi}{n\int\Sigma(\phi)d\phi}}. \tag{A.5}$$

The statistical significance S is

$$S \equiv \frac{\delta_{\mathcal{O}}}{\Delta\mathcal{O}} \equiv \lambda\sqrt{nR/\sigma}, \tag{A.6}$$

where $\sigma(=\int\Sigma d\phi)$ is the total cross section and R is the "resolving power" of the function f, given by

$$R \equiv \frac{\sigma}{n\lambda^2}\frac{\delta_{\mathcal{O}}^2}{(\Delta\mathcal{O})^2} \approx \frac{(\int f\Sigma_1 d\phi)^2}{\int f^2\Sigma_0 d\phi}. \tag{A.7}$$

Here, we want to find a function f which can maximize R (and S).

In order to find a function which makes R an extremum, the functional differentiation method is used. At the extremum, the variation of R should be equal to zero. Using an arbitrary function g and a small constant ε, the variation of R is given by

$$\begin{aligned} \Delta R = R(f+\varepsilon g) - R(f) &= \frac{(\int (f+\varepsilon g)\Sigma_1 d\phi)^2}{\int (f+\varepsilon g)^2 \Sigma_0 d\phi} - \frac{(\int f\Sigma_1 d\phi)^2}{\int f^2\Sigma_0 d\phi}, & \text{(A.8)} \\ &= \frac{2\varepsilon(\int f\Sigma_1 d\phi)[\int g\Sigma_1 d\phi \int f^2\Sigma_0 d\phi - \int fg\Sigma_0 d\phi \int f\Sigma_1 d\phi]}{(\int f^2\Sigma_0 d\phi)^2}, & \text{(A.9)} \\ &= 0. & \text{(A.10)} \end{aligned}$$

Because the significance S should not be zero, $\int f\Sigma_1 d\phi \neq 0$. Considering $\int f^2\Sigma_0 d\phi$ and $\int f\Sigma_1 d\phi$ constant, the equation becomes

$$\int g\left\{\Sigma_1 \int f^2\Sigma_0 d\phi - f\Sigma_0 \int f\Sigma_1 d\phi\right\} d\phi' = 0. \tag{A.11}$$

Because the function g is arbitrary, the equation should satisfy the following condition:

$$\Sigma_1 \int f^2\Sigma_0 d\phi - f\Sigma_0 \int f\Sigma_1 d\phi = 0. \tag{A.12}$$

Then,

$$f = \frac{\int f^2\Sigma_0 d\phi}{\int f\Sigma_1 d\phi} \times \frac{\Sigma_1}{\Sigma_0}. \tag{A.13}$$

Note that $\int f^2\Sigma_0 d\phi$ and $\int f\Sigma_1 d\phi$ are constant. Therefore, the above equation can be rewritten as $f = \text{Const.} \times \frac{\Sigma_1}{\Sigma_0}$. Because clearly R does not depend on rescaling f, we can take

$$f = \frac{\Sigma_1}{\Sigma_0}, \tag{A.14}$$

while satisfying Eq.(A.13) without any loss of generality, and the function is only one solution to maximize the R and S. This function is the so-called optimal observable ($\mathcal{O} = f = \frac{\Sigma_1}{\Sigma_0}$).

The mean value of the observable, which is defined in Eq.(A.3), becomes

$$\langle \mathcal{O} \rangle = \int \frac{\Sigma_1}{\Sigma_0}(\Sigma_0 + \lambda\Sigma_1)d\phi \Big/ \int \Sigma d\phi = \lambda \int \frac{\Sigma_1^2}{\Sigma_0} d\phi. \Big/ \int \Sigma d\phi\,. \tag{A.15}$$

Here, the assumption $\langle \mathcal{O}(0) \rangle = 0$ is used. The $\langle \mathcal{O} \rangle$ shows the linear dependence on λ. $\int \frac{\Sigma_1^2}{\Sigma_0} d\phi$ is the sensitivity, and can be calculated analytically, if all kinematical variables are measured.

Even if $\langle \mathcal{O} \rangle \neq 0$, $f = \frac{\Sigma_1}{\Sigma_0}$ is optimized. In this case, the mean value of the observable will have some offset:

$$\langle \mathcal{O} \rangle = \int \frac{\Sigma_1}{\Sigma_0}(\Sigma_0 + \lambda\Sigma_1)d\phi \Big/ \int \Sigma d\phi = \left[\int \Sigma_1 d\phi + \lambda \int \frac{\Sigma_1^2}{\Sigma_0} d\phi\right] \Big/ \int \Sigma d\phi\,. \tag{A.16}$$

A.2 Comparison with a likelihood fit

Here, the optimal observable method is compared with the maximum-likelihood fit method. Using the differential cross section given in Eq.(A.2), the likelihood function $\mathcal{L}(\phi_i, \lambda)$ can be written as

$$\mathcal{L}(\phi_i, \lambda) \sim \prod_i \Sigma(\phi_i) = \prod_i [\Sigma_0(\phi_i) + \lambda\Sigma_1(\phi_i)]. \tag{A.17}$$

The true parameter, λ_0, maximizes the likelihood and satisfies the equation

$$\frac{\partial}{\partial\lambda}\log\mathcal{L}\bigg|_{\lambda=\lambda_0}=\sum_i\frac{\Sigma_1(\phi_i)}{\Sigma_0(\phi_i)+\lambda_0\Sigma_1(\phi_i)}=\sum_i\frac{f(\phi_i)}{1+\lambda_0 f(\phi_i)}=0, \tag{A.18}$$

where $f=\frac{\Sigma_1}{\Sigma_0}$, and it is the same as the optimal observable given in Eq.(A.14). Clearly, the likelihood $\mathcal{L}$ depends only on the optimal observable f. If the parameter λ_0 is small, we can obtain $\sum_i f_i(1-\lambda_0 f_i)=0$. Then, the following equation can be given:

$$\sum_i f_i=\lambda_0\sum_i f_i^2=\lambda_0\int\left(\frac{\Sigma_1}{\Sigma_0}\right)^2(\Sigma_0+\lambda\Sigma_1)d\phi\simeq\lambda_0\int\frac{\Sigma_1^2}{\Sigma_0}d\phi. \tag{A.19}$$

$$\langle\mathcal{O}\rangle=\sum_i f_i\bigg/\sum_i=\lambda_0\int\frac{\Sigma_1^2}{\Sigma_0}d\phi\bigg/\int\Sigma d\phi\,. \tag{A.20}$$

Therefore, the likelihood fit method also gives the same result as Eq.(A.15). This result indicates that these two methods show the same sensitivity.

Appendix B

Amplitude calculation

In this section, the calculation of the spin-density matrix elements with electric and magnetic dipole moments from the effective Lagrangian to the matrix elements with the spin vector indices is summarized.

B.1 Effective Lagrangian

The effective Lagrangian with magnetic dipole moment (MDM) and electric dipole moment (EDM) terms can be expressed as follows:

$$
\begin{aligned}
\mathcal{L}_{\mathrm{eff}} &= \mathcal{L}_{\mathrm{SM}} + \Delta\mathcal{L}, && \text{(B.1)}\\
\mathcal{L}_{\mathrm{SM}} &= \bar{\psi}(i \not{\partial} - eQ \not{A})\psi, && \text{(B.2)}\\
\Delta\mathcal{L} &= c_{\mathrm{MDM}}\bar{\psi}\sigma^{\mu\nu}\psi\partial_\mu A_\nu - ic_{\mathrm{EDM}}\bar{\psi}\sigma^{\mu\nu}\gamma_5\psi\partial_\mu A_\nu + (h.c.), && \text{(B.3)}\\
&= \frac{1}{2}\bar{\psi}\sigma^{\mu\nu}\psi\{\Delta\mu_\tau F_{\mu\nu} - d_\tau\tilde{F}_{\mu\nu}\}, && \text{(B.4)}\\
F^{\mu\nu} &= \partial^\mu A^\nu - \partial^\nu A^\mu, \qquad \tilde{F}^{\mu\nu} = \frac{1}{2}\epsilon^{\mu\nu\rho\sigma}F_{\rho\sigma}, && \text{(B.5)}
\end{aligned}
$$

where $\Delta\mu_\tau(\equiv c_{\mathrm{MDM}} + c^*_{\mathrm{MDM}})$ is the magnetic dipole form-factor (the anomalous magnetic moment) and $d_\tau(\equiv c_{\mathrm{EDM}}+c^*_{\mathrm{EDM}})$ is the electric dipole form-factor. A_μ is the electromagnetic vector potential and $F_{\mu\nu}$ is the electromagnetic field tensor. These form-factors are often used in terms of the dimensionless dipole moment, a_τ and $\tilde{a}_\tau$:

$$
\Delta\mu_\tau = \frac{e}{2m_\tau}a_\tau, \qquad d_\tau = \frac{e}{2m_\tau}\tilde{a}_\tau. \tag{B.6}
$$

By definition, the dipole form-factors must be real. However, from the experimental point of view, the imaginary part should be measured. Therefore, the form-factors are generally re-defined as a complex number hereafter.

Here, the lowest-order gamma exchange diagram and MDM/EDM contribution (Figure B.1) are used to calculate the amplitudes; the Z exchange diagram is ignored.

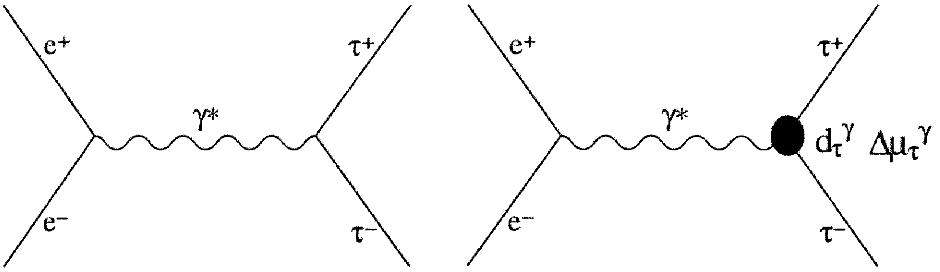

Figure B.1: Diagrams used in the calculation for the lowest order gamma exchange (left) and the MDM/EDM contribution (right).

B.2 Lagrangian to spin amplitudes

B.2.1 Convention

The following Weyl-basis convention is used, which is defined in HELAS [9, 10] /MadGraph [11].

$$\gamma_5 = i\gamma^0\gamma^1\gamma^2\gamma^3 = \begin{pmatrix} -1 & 0 \\ 0 & 1 \end{pmatrix}, \quad \gamma^\mu = \begin{pmatrix} 0 & \sigma_+^\mu \\ \sigma_-^\mu & 0 \end{pmatrix},$$

$$\{\gamma_5, \gamma^\mu\} = 0, \quad \sigma_\pm^\mu = (1, \pm\sigma^i),$$

$$\{\gamma^\mu, \gamma^\nu\} = 2g^{\mu\nu}, \quad g^{\mu\nu} = diag(1, -1, -1, -1),$$

$$\gamma_5\sigma^{\mu\nu} = \sigma^{\mu\nu}\gamma_5 = -\frac{i}{2}\epsilon^{\mu\nu\rho\sigma}\sigma_{\rho\sigma}, \quad \sigma^{\mu\nu} = \frac{i}{2}[\gamma^\mu, \gamma^\nu],$$

$$\epsilon_{0123} = 1, \quad \epsilon^{0123} = -1.$$

B.2.2 Coordinate system and spin amplitudes

The momenta and the helicities for the corresponding particles are defined as

$$e^-(p, \lambda) + e^+(\bar{p}, \bar{\lambda}) \to \tau^-(k, \sigma) + \tau^+(\bar{k}, \bar{\sigma}),$$

where $p, \bar{p}, k$ and $\bar{k}$ denote the 4-momenta and $\lambda, \bar{\lambda}, \sigma$ and $\bar{\sigma}$ denote the helicities ($L : -$, $R : +$). In this calculation, the electron mass is neglected.

In the following, the coordinate system defined as Figure B.2 is used in order to simplify the calculation.

The 4-momenta are defined as:

$$p^\mu = E(1, -\sin\theta, 0, \cos\theta), \tag{B.7}$$

$$\bar{p}^\mu = E(1, \sin\theta, 0, -\cos\theta), \tag{B.8}$$

$$k^\mu = E(1, 0, 0, \beta), \tag{B.9}$$

$$\bar{k}^\mu = E(1, 0, 0, -\beta). \tag{B.10}$$

From the effective Lagrangian, the spin amplitudes can be obtained as

$$i\mathcal{M} = -ieQ_e(j_{L\mu} + j_{R\mu})\frac{-i}{s}[-ieQ_\tau(J_L^\mu + J_R^\mu) - i\frac{e}{2m}(a_\tau J_a^\mu + \tilde{a}_\tau J_{\tilde{a}}^\mu)], \tag{B.11}$$

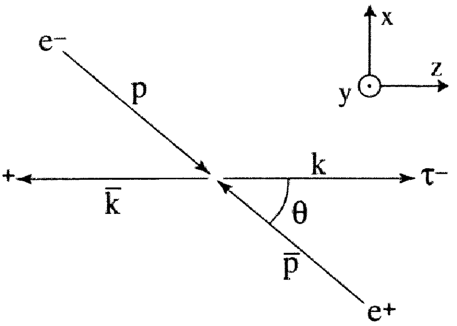

Figure B.2: Coordinate system for the calculation.

where Q_e and Q_τ are the charges of an electron and a τ, respectively. ($Q_e = -1$. $Q_\tau = -1$.) s is the squared center-of-mass energy. ($\sqrt{s} = 2E$.) m is the τ mass, m_τ. The charged currents are defined as follows:

$$j_L^\mu = \bar{v}(\bar{p}, \bar{\lambda} = +)\gamma^\mu \frac{1-\gamma_5}{2} u(p, \lambda = -), \tag{B.12}$$

$$j_R^\mu = \bar{v}(\bar{p}, \bar{\lambda} = -)\gamma^\mu \frac{1+\gamma_5}{2} u(p, \lambda = +), \tag{B.13}$$

$$J_L^\mu = \bar{u}(k, \sigma)\gamma^\mu \frac{1-\gamma_5}{2} v(\bar{k}, \bar{\sigma}), \tag{B.14}$$

$$J_R^\mu = \bar{u}(k, \sigma)\gamma^\mu \frac{1+\gamma_5}{2} v(\bar{k}, \bar{\sigma}), \tag{B.15}$$

$$J_a^\mu = -i\bar{u}(k, \sigma)\sigma^{\mu\nu} q_\nu v(\bar{k}, \bar{\sigma}), \tag{B.16}$$

$$J_{\tilde{a}}^\mu = -\bar{u}(k, \sigma)\sigma^{\mu\nu} q_\nu v(\bar{k}, \bar{\sigma}). \tag{B.17}$$

q_ν is the 4-momentum of an internal gamma, defined as $q_\nu = (\sqrt{s}, 0, 0, 0)$ in this coordinate system.

Using the HELAS conventions, the following expressions are given for the charged currents:

$$j_L^\mu = -2E(0, \cos\theta, -i, \sin\theta), \quad (\lambda, \bar{\lambda}) = (-, +), \tag{B.18}$$

$$j_R^\mu = -2E(0, \cos\theta, \ \ i, \sin\theta), \quad (\lambda, \bar{\lambda}) = (+, -). \tag{B.19}$$

$\sigma\bar{\sigma}$	J_L^μ	J_R^μ	J_a^μ	$J_{\tilde{a}}^\mu$
$++$	$m(1, 0, 0, -1)$	$m(-1, 0, 0, -1)$	$4E^2(0, 0, 0, \ \ 1)$	$4iE^2\beta(0, 0, 0, 1)$
$+-$	$E(1-\beta)(0, -1, \ \ i, 0)$	$E(1+\beta)(0, -1, \ \ i, 0)$	$4Em(0, 1, -i, 0)$	0
$-+$	$E(1+\beta)(0, -1, -i, 0)$	$E(1-\beta)(0, -1, -i, 0)$	$4Em(0, 1, \ \ i, 0)$	0
$--$	$m(1, 0, 0, \ \ 1)$	$m(-1, 0, 0, \ \ 1)$	$4E^2(0, 0, 0, -1)$	$4iE^2\beta(0, 0, 0, 1)$

Then, the 8 current products are obtained as follows:

$\lambda\bar{\lambda}\sigma\bar{\sigma}$	$j_L J_L$	$j_L J_R$	$j_L J_a$	$j_L J_{\tilde{a}}$
$-+++$	$-2Em\sin\theta$	$-2Em\sin\theta$	$8E^3\sin\theta$	$8iE^3\beta\sin\theta$
$-++-$	$2E^2(1-\beta)(1-\cos\theta)$	$2E^2(1+\beta)(1-\cos\theta)$	$-8E^2m(1-\cos\theta)$	0
$-+-+$	$-2E^2(1+\beta)(1+\cos\theta)$	$-2E^2(1-\beta)(1+\cos\theta)$	$8E^2m(1+\cos\theta)$	0
$-+--$	$2Em\sin\theta$	$2Em\sin\theta$	$-8E^3\sin\theta$	$8iE^3\beta\sin\theta$

$\lambda\bar{\lambda}\sigma\bar{\sigma}$	$j_R J_L$	$j_R J_R$	$j_R J_a$	$j_R J_{\tilde{a}}$
$+-++$	$-2Em\sin\theta$	$-2Em\sin\theta$	$8E^3\sin\theta$	$8iE^3\beta\sin\theta$
$+-+-$	$-2E^2(1-\beta)(1+\cos\theta)$	$-2E^2(1+\beta)(1+\cos\theta)$	$8E^2m(1+\cos\theta)$	0
$+--+$	$2E^2(1+\beta)(1-\cos\theta)$	$2E^2(1-\beta)(1-\cos\theta)$	$-8E^2m(1-\cos\theta)$	0
$+---$	$2Em\sin\theta$	$2Em\sin\theta$	$-8E^3\sin\theta$	$8iE^3\beta\sin\theta$

Finally, the spin amplitudes $\mathcal{M}(\lambda\bar{\lambda}\sigma\bar{\sigma})$ are obtained as

$$\begin{aligned}
\mathcal{M}(+-++) &= \frac{e^2}{s}[-4Em\sin\theta] + \frac{-e^2}{2ms}a_\tau[8E^3\sin\theta] + \frac{-e^2}{2ms}\tilde{a}_\tau[8iE^3\beta\sin\theta] \\
\mathcal{M}(+-+-) &= \frac{e^2}{s}[-4E^2(1+\cos\theta)] + \frac{-e^2}{2ms}a_\tau[8E^2m(1+\cos\theta)] \\
\mathcal{M}(+--+) &= \frac{e^2}{s}[4E^2(1-\cos\theta)] + \frac{-e^2}{2ms}a_\tau[-8E^2m(1-\cos\theta)] \\
\mathcal{M}(+---) &= \frac{e^2}{s}[4Em\sin\theta] + \frac{-e^2}{2ms}a_\tau[-8E^3\sin\theta] + \frac{-e^2}{2ms}\tilde{a}_\tau[8iE^3\beta\sin\theta] \\
\mathcal{M}(-+++) &= \frac{e^2}{s}[-4Em\sin\theta] + \frac{-e^2}{2ms}a_\tau[8E^3\sin\theta] + \frac{-e^2}{2ms}\tilde{a}_\tau[8iE^3\beta\sin\theta] \\
\mathcal{M}(-++-) &= \frac{e^2}{s}[4E^2(1-\cos\theta)] + \frac{-e^2}{2ms}a_\tau[-8E^2m(1-\cos\theta)] \\
\mathcal{M}(-+-+) &= \frac{e^2}{s}[-4E^2(1+\cos\theta)] + \frac{-e^2}{2ms}a_\tau[8E^2m(1+\cos\theta)] \\
\mathcal{M}(-+--) &= \frac{e^2}{s}[4Em\sin\theta] + \frac{-e^2}{2ms}a_\tau[-8E^3\sin\theta] + \frac{-e^2}{2ms}\tilde{a}_\tau[8iE^3\beta\sin\theta]
\end{aligned}$$

To make the equations simple, the following definitions are used:

$$\begin{aligned}
A &\equiv \frac{e^2}{s}[-4Em\sin\theta] + \frac{-e^2}{2ms}a_\tau[8E^3\sin\theta] + \frac{-e^2}{2ms}\tilde{a}_\tau[8iE^3\beta\sin\theta] \\
B &\equiv \frac{e^2}{s}[-4E^2(1+\cos\theta)] + \frac{-e^2}{2ms}a_\tau[8E^2m(1+\cos\theta)] \\
C &\equiv \frac{e^2}{s}[4E^2(1-\cos\theta)] + \frac{-e^2}{2ms}a_\tau[-8E^2m(1-\cos\theta)] \\
D &\equiv \frac{e^2}{s}[4Em\sin\theta] + \frac{-e^2}{2ms}a_\tau[-8E^3\sin\theta] + \frac{-e^2}{2ms}\tilde{a}_\tau[8iE^3\beta\sin\theta]
\end{aligned}$$

This indicates that

$$\begin{aligned}
\mathcal{M}(+-++) &= \mathcal{M}(-+++) = A, \\
\mathcal{M}(+-+-) &= \mathcal{M}(-+-+) = B, \\
\mathcal{M}(+--+) &= \mathcal{M}(-++-) = C, \\
\mathcal{M}(+---) &= \mathcal{M}(-+--) = D.
\end{aligned}$$

B.3 Spin amplitudes to the spin density matrix

B.3.1 Transformation of notation

Here, the spin-density matrix is calculated in a way similar to that used in KORALB [27]. Since the conventions used in KORALB and in HELAS are different, the spin amplitudes are transformed by applying the factors as follows:

$$
\begin{array}{lccc}
 & \text{HELAS} & \rightarrow & \text{KORALB} \\
\mathcal{M}(+-++): & A & \rightarrow & -A \\
\mathcal{M}(+-+-): & B & \rightarrow & iB \\
\mathcal{M}(+--+): & C & \rightarrow & iC \\
\mathcal{M}(+---): & D & \rightarrow & D \\
\mathcal{M}(-+++): & A & \rightarrow & -A \\
\mathcal{M}(-++-): & C & \rightarrow & iC \\
\mathcal{M}(-+-+): & B & \rightarrow & iB \\
\mathcal{M}(-+--): & D & \rightarrow & D
\end{array}
$$

B.3.2 Spin density matrix

The spin-density matrix ϱ is defined as

$$\varrho_{\alpha_1\bar{\alpha}_1\alpha_2\bar{\alpha}_2} \equiv \frac{1}{4}\sum_{\lambda_1\lambda_2} \mathcal{M}_{\lambda_1\lambda_2\alpha_1\alpha_2}(\mathcal{M}_{\lambda_1\lambda_2\bar{\alpha}_1\bar{\alpha}_2})^*, \tag{B.20}$$

where λ_1 and λ_2 are the helicities of the $e^{\mp}$ beam, $\alpha_1(\bar{\alpha}_1)$ is the helicity of the τ^- and $\alpha_2(\bar{\alpha}_2)$ is the helicity of the τ^+. (Here, unpolarized e^+ and e^- beams are assumed.) The differential cross-section can be written as

$$d\sigma \sim \varrho \; d\text{Lips},$$

where dLips is the Lorentz-invariant phase space factor. Using the expressions defined in the previous section, ϱ is given as follows:

$$
\begin{aligned}
4\varrho_{++++} &= 2AA^* \\
4\varrho_{+++-} &= i(AB^* + AC^*) \\
4\varrho_{++-+} &= -i(BA^* + CA^*) \\
4\varrho_{++--} &= BB^* + CC^* \\
4\varrho_{+-++} &= i(AB^* + AC^*) \\
4\varrho_{+-+-} &= -2AD^* \\
4\varrho_{+--+} &= BC^* + CB^* \\
4\varrho_{+---} &= i(BD^* + CD^*) \\
4\varrho_{-+++} &= -i(BA^* + CA^*) \\
4\varrho_{-++-} &= BC^* + CB^* \\
4\varrho_{-+-+} &= -2DA^* \\
4\varrho_{-+--} &= -i(DB^* + DC^*) \\
4\varrho_{--++} &= BB^* + CC^* \\
4\varrho_{--+-} &= i(BD^* + CD^*) \\
4\varrho_{---+} &= -i(DB^* + DC^*) \\
4\varrho_{----} &= 2DD^*
\end{aligned}
$$

Now, we want to translate the bispinor indices in the spin-density matrix into the polarization vector indices. Using the "standard techniques" [7, 8], the below equation is obtained.

$$\varrho = \frac{1}{4}\sum \mathcal{M}(\mathcal{M})^* = e^4 \sum_{ab} R_{ab} s_1^a s_2^b, \quad (a, b = 0, 1, 2, 3), \tag{B.21}$$

where s_1 and s_2 are the polarization vectors of the τ^- and the τ^+. The zero-th component is defined as 1.($s^0 = 1$) The three components of s_1 are defined in the τ^- rest frame and the components of s_2 are in the τ^+ rest frame. The third axis is the spin quantization axis, which is the τ^+ flight direction in the τ-pair rest frame, and the first axis is defined to be perpendicular to the reaction plane. (See Figure B.3.)

The matrix R_{ab} can be obtained by the equation [27],

$$e^4 R_{ab} = \sum_{\alpha\bar{\alpha}} C^-_{a,\alpha_1\bar{\alpha}_1} C^+_{b,\bar{\alpha}_2\alpha_2} \varrho_{\alpha_1\bar{\alpha}_1\alpha_2\bar{\alpha}_2}. \tag{B.22}$$

By changing into the matrix notation, the equation becomes

$$e^4 R_{ab} = C^{\tau^-}_{db} \varrho_{cd} C^{\tau^+}_{ac}, \tag{B.23}$$

where c and d are defined as $c = (\alpha_1\bar{\alpha}_1)$, $d = (\alpha_2\bar{\alpha}_2)$ and numbered by $(\alpha\bar{\alpha}) = (++), (--), (+-), (-+)$. The matrices $C^{\tau^-}_{db}$ and $C^{\tau^+}_{ac}$ are defined as

$$C^{\tau^-}_{db} = \begin{pmatrix} 1 & 1 & 0 & 0 \\ 0 & 0 & 1 & 1 \\ 0 & 0 & -i & i \\ -1 & 1 & 0 & 0 \end{pmatrix}, \quad C^{\tau^+}_{ac} = \begin{pmatrix} 1 & 0 & 0 & 1 \\ 1 & 0 & 0 & -1 \\ 0 & 1 & i & 0 \\ 0 & 1 & -i & 0 \end{pmatrix}.$$

(Note that, for the matrix C_{ab}, a is the column number and b is the row number.) The matrix ϱ is defined as

$$\varrho_{cd} = \begin{pmatrix} \varrho_{++++} & \varrho_{--++} & \varrho_{+-++} & \varrho_{-+++} \\ \varrho_{++--} & \varrho_{----} & \varrho_{+---} & \varrho_{-+--} \\ \varrho_{+++-} & \varrho_{--+-} & \varrho_{+-+-} & \varrho_{-++-} \\ \varrho_{++-+} & \varrho_{---+} & \varrho_{+--+} & \varrho_{-+-+} \end{pmatrix}.$$

Then, the matrix R_{ab} can be given using the following equations:

$$\begin{aligned}
4e^4 R_{11} &= 2(AA^* + BB^* + CC^* + DD^*), \\
4e^4 R_{22} &= -2(AD^* + DA^* - BC^* - CB^*), \\
4e^4 R_{33} &= -2(AD^* + DA^* + BC^* + CB^*), \\
4e^4 R_{44} &= -2(AA^* - BB^* - CC^* + DD^*), \\
4e^4 R_{21} = 4e^4 R_{12} &= i([AB^* + AC^* + BD^* + CD^*] - [c.c.]), \\
4e^4 R_{31} = -4e^4 R_{13} &= -([AB^* + AC^* + BD^* + CD^*] + [c.c.]), \\
4e^4 R_{41} = -4e^4 R_{41} &= 2(AA^* - DD^*), \\
4e^4 R_{32} = -4e^4 R_{23} &= -2i(AD^* - DA^*), \\
4e^4 R_{42} = -4e^4 R_{24} &= i([AB^* + AC^* - BD^* - CD^*] - [c.c.]), \\
4e^4 R_{43} = 4e^4 R_{34} &= ([AB^* + AC^* - BD^* - CD^*] + [c.c.]).
\end{aligned}$$

The matrix R_{ab} is expanded in terms of the dipole moment as

$$R = R_{\mathrm{SM}} + R_a + R_{\tilde{a}} + R_{a^2} + R_{\tilde{a}^2} + R_{a\tilde{a}}, \tag{B.24}$$

where R_{SM} is the Standard Model lowest-order term. R_a and $R_{\tilde{a}}$ are interference terms of the lowest order and the dipole moment coupling for MDM and EDM, respectively. R_{a^2}, $R_{\tilde{a}^2}$ and $R_{a\tilde{a}}$ are bilinear in the dipole form factors, which can be neglected for the small dipole form-factors.

The decomposed matrices R are obtained as follows:

$$R_{\mathrm{SM}} = \begin{pmatrix} 1+c^2+\frac{m^2}{E^2}s^2 & 0 & 0 & 0 \\ 0 & -(1-\frac{m^2}{E^2})s^2 & 0 & 0 \\ 0 & 0 & (1+\frac{m^2}{E^2})s^2 & 2\frac{m}{E}sc \\ 0 & 0 & 2\frac{m}{E}sc & 1+c^2-\frac{m^2}{E^2}s^2 \end{pmatrix}, \tag{B.25}$$

$$R_a = \begin{pmatrix} 4Re(a) & 2(\frac{m}{E}-\frac{E}{m})scIm(a) & 0 & 0 \\ 2(\frac{m}{E}-\frac{E}{m})scIm(a) & 0 & 0 & 0 \\ 0 & 0 & 4s^2Re(a) & 2(\frac{m}{E}+\frac{E}{m})scRe(a) \\ 0 & 0 & 2(\frac{m}{E}+\frac{E}{m})scRe(a) & 4c^2Re(a) \end{pmatrix} \tag{B.26}$$

$$R_{\tilde{a}} = \begin{pmatrix} 0 & 0 & 2\frac{E}{m}\beta sc\cdot Im(\tilde{a}) & -2\beta s^2\cdot Im(\tilde{a}) \\ 0 & 0 & -2\beta s^2\cdot Re(\tilde{a}) & -2\frac{E}{m}\beta sc\cdot Re(\tilde{a}) \\ -2\frac{E}{m}\beta sc\cdot Im(\tilde{a}) & 2\beta s^2\cdot Re(\tilde{a}) & 0 & 0 \\ 2\beta s^2\cdot Im(\tilde{a}) & 2\frac{E}{m}\beta sc\cdot Re(\tilde{a}) & 0 & 0 \end{pmatrix}, \tag{B.27}$$

$$R_{a^2} = \begin{pmatrix} (1+c^2+\frac{E^2}{m^2}s^2)\cdot aa^* & 0 & 0 & 0 \\ 0 & -(1-\frac{E^2}{m^2})s^2\cdot aa^* & 0 & 0 \\ 0 & 0 & (1+\frac{E^2}{m^2})s^2\cdot aa^* & 2\frac{E}{m}sc\cdot aa^* \\ 0 & 0 & 2\frac{E}{m}sc\cdot aa^* & (1+c^2-\frac{E^2}{m^2}s^2)\cdot aa^* \end{pmatrix} \tag{B.28}$$

$$R_{\tilde{a}^2} = \begin{pmatrix} \frac{E^2}{m^2}\beta^2s^2\cdot\tilde{a}\tilde{a}^* & 0 & 0 & 0 \\ 0 & -\frac{E^2}{m^2}\beta^2s^2\cdot\tilde{a}\tilde{a}^* & 0 & 0 \\ 0 & 0 & -\frac{E^2}{m^2}\beta^2s^2\cdot\tilde{a}\tilde{a}^* & 0 \\ 0 & 0 & 0 & -\frac{E^2}{m^2}\beta^2s^2\cdot\tilde{a}\tilde{a}^* \end{pmatrix}, \tag{B.29}$$

$$R_{a\tilde{a}} = \begin{pmatrix} 0 & 0 & 2\frac{E}{m}\beta sc\cdot Im(a\tilde{a}) & 0 \\ 0 & 0 & 2\frac{E^2}{m^2}\beta s^2\cdot Re(a\tilde{a}) & -2\frac{E}{m}\beta sc\cdot Re(a\tilde{a}) \\ -2\frac{E}{m}\beta sc\cdot Im(a\tilde{a}) & -2\frac{E^2}{m^2}\beta s^2\cdot Re(a\tilde{a}) & 0 & 0 \\ 0 & 2\frac{E}{m}\beta sc\cdot Re(a\tilde{a}) & 0 & 0 \end{pmatrix}, \tag{B.30}$$

where $s = \sin\theta$ and $c = \cos\theta$.

B.3.3 Spin vector notation

The spin-vector indices should be translated into explicit spin-vector notation. For the reaction

$$e^+(\boldsymbol{p}) + e^-(-\boldsymbol{p}) \to \tau^+(\boldsymbol{k}, \boldsymbol{S}_+) + \tau^-(-\boldsymbol{k}, \boldsymbol{S}_-),$$

where $\boldsymbol{p}$ and $\boldsymbol{k}$ are the 3-momenta and $\boldsymbol{S}_\pm$ is the spin vector, the coordinate system of the spin vector indices is defined as

$$\hat{\boldsymbol{X}} = \frac{\hat{\boldsymbol{p}}\times\hat{\boldsymbol{k}}}{|\hat{\boldsymbol{p}}\times\hat{\boldsymbol{k}}|}, \tag{B.31}$$

$$\hat{\boldsymbol{Y}} = a[\hat{\boldsymbol{p}} - (\hat{\boldsymbol{k}}\cdot\hat{\boldsymbol{p}})\hat{\boldsymbol{k}}], \tag{B.32}$$

$$\hat{\boldsymbol{Z}} = \hat{\boldsymbol{k}}, \tag{B.33}$$

where the hat denotes the unit vector and $a = \frac{1}{\sqrt{1-(\hat{\boldsymbol{k}}\cdot\hat{\boldsymbol{p}})^2}} = 1/\sin\theta$. (See Figure B.3.)

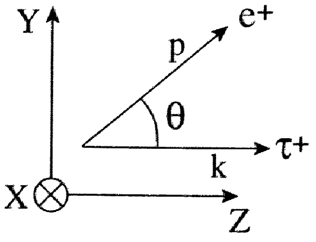

Figure B.3: Coordinate system of the spin-vector indices.

Then, the spin-vector indices $s^{1,2,3}$ are expressed as

$$s^1 = \boldsymbol{S} \cdot \hat{\boldsymbol{X}} = a[\boldsymbol{S} \cdot (\hat{\boldsymbol{p}} \times \hat{\boldsymbol{k}})], \tag{B.34}$$

$$s^2 = \boldsymbol{S} \cdot \hat{\boldsymbol{Y}} = a[(\boldsymbol{S} \cdot \hat{\boldsymbol{p}}) - (\hat{\boldsymbol{k}} \cdot \hat{\boldsymbol{p}})(\boldsymbol{S} \cdot \hat{\boldsymbol{k}})], \tag{B.35}$$

$$s^3 = \boldsymbol{S} \cdot \hat{\boldsymbol{Z}} = \boldsymbol{S} \cdot \hat{\boldsymbol{k}}. \tag{B.36}$$

Finally, using Eq.(B.21), the matrices R and the above spin-vector indices, the following result is obtained:

$$\begin{aligned} \varrho_{\mathrm{prod}} = {} & \varrho_{\mathrm{SM}} + Re(d_\tau)\varrho_{Re} + Im(d_\tau)\varrho_{Im} + |d_\tau|^2 \varrho_{d^2} \\ & + Re(a_\tau)\varrho_{ReF2} + Im(a_\tau)\varrho_{ImF2}, \end{aligned} \tag{B.37}$$

$$\begin{aligned} \varrho_{\mathrm{SM}} = {} & \frac{e^4}{k_0^2}[\ k_0^2 + m_\tau^2 + |\boldsymbol{k}^2|(\hat{\boldsymbol{k}}\cdot\hat{\boldsymbol{p}})^2 - \boldsymbol{S}_+\cdot\boldsymbol{S}_-|\boldsymbol{k}|^2(1-(\hat{\boldsymbol{k}}\cdot\hat{\boldsymbol{p}})^2) \\ & + 2(\hat{\boldsymbol{k}}\cdot\boldsymbol{S}_+)(\hat{\boldsymbol{k}}\cdot\boldsymbol{S}_-)(|\boldsymbol{k}|^2 + (k_0-m_\tau)^2(\hat{\boldsymbol{k}}\cdot\hat{\boldsymbol{p}})^2) + 2k_0^2(\hat{\boldsymbol{p}}\cdot\boldsymbol{S}_+)(\hat{\boldsymbol{p}}\cdot\boldsymbol{S}_-) \\ & - 2k_0(k_0-m_\tau)(\hat{\boldsymbol{k}}\cdot\hat{\boldsymbol{p}})((\hat{\boldsymbol{k}}\cdot\boldsymbol{S}_+)(\hat{\boldsymbol{p}}\cdot\boldsymbol{S}_-) + (\hat{\boldsymbol{k}}\cdot\boldsymbol{S}_-)(\hat{\boldsymbol{p}}\cdot\boldsymbol{S}_+))\ ], \end{aligned} \tag{B.38}$$

$$\begin{aligned} \varrho_{Re} = {} & 4k_0|\boldsymbol{k}|\frac{e^3}{k_0^2}[\ -(m_\tau + (k_0-m_\tau)(\hat{\boldsymbol{k}}\cdot\hat{\boldsymbol{p}})^2)(\boldsymbol{S}_+ \times \boldsymbol{S}_-)\cdot\hat{\boldsymbol{k}} \\ & + k_0(\hat{\boldsymbol{k}}\cdot\hat{\boldsymbol{p}})(\boldsymbol{S}_+ \times \boldsymbol{S}_-)\cdot\hat{\boldsymbol{p}}\ ], \end{aligned} \tag{B.39}$$

$$\begin{aligned} \varrho_{Im} = {} & 4k_0|\boldsymbol{k}|\frac{e^3}{k_0^2}[\ -(m_\tau + (k_0-m_\tau)(\hat{\boldsymbol{k}}\cdot\hat{\boldsymbol{p}})^2)(\boldsymbol{S}_+ - \boldsymbol{S}_-)\cdot\hat{\boldsymbol{k}} \\ & + k_0(\hat{\boldsymbol{k}}\cdot\hat{\boldsymbol{p}})(\boldsymbol{S}_+ - \boldsymbol{S}_-)\cdot\hat{\boldsymbol{p}}\ ], \end{aligned} \tag{B.40}$$

$$\varrho_{d^2} = 4k_0^2|\boldsymbol{k}|^2\frac{e^2}{k_0^2}\cdot\ (1-(\hat{\boldsymbol{k}}\cdot\hat{\boldsymbol{p}})^2)(1-\boldsymbol{S}_+\cdot\boldsymbol{S}_-), \tag{B.41}$$

$$\begin{aligned} \varrho_{ReF2} = {} & \frac{2e^4}{mk_0}[\ 2mk_0 - 2(\hat{\boldsymbol{k}}\cdot\boldsymbol{S}_+)(\hat{\boldsymbol{k}}\cdot\boldsymbol{S}_-)(k_0-m_\tau)^2(\hat{\boldsymbol{k}}\cdot\hat{\boldsymbol{p}})^2 + 2mk_0(\hat{\boldsymbol{p}}\cdot\boldsymbol{S}_+)(\hat{\boldsymbol{p}}\cdot\boldsymbol{S}_-) \\ & + (k_0-m_\tau)^2(\hat{\boldsymbol{k}}\cdot\hat{\boldsymbol{p}})((\hat{\boldsymbol{k}}\cdot\boldsymbol{S}_+)(\hat{\boldsymbol{p}}\cdot\boldsymbol{S}_-) + (\hat{\boldsymbol{k}}\cdot\boldsymbol{S}_-)(\hat{\boldsymbol{p}}\cdot\boldsymbol{S}_+))\ ], \end{aligned} \tag{B.42}$$

$$\varrho_{ImF2} = \frac{2e^4}{mk_0}[\ |\boldsymbol{k}|^2(\hat{\boldsymbol{k}}\cdot\hat{\boldsymbol{p}})(\boldsymbol{S}_+ + \boldsymbol{S}_-)\cdot(\hat{\boldsymbol{k}} \times \hat{\boldsymbol{p}})\ ], \tag{B.43}$$

where $k_0 = E_\tau$.

Appendix C

τ-pair pre-selection

Pre-selection of the τ pair event is described in this section. Its criteria are used in the *evtcls* module, which is a Belle event-classification program. The following list gives the selection criteria in *evtcls*.

Definitions

Charged tracks: $P_t \geq 0.1$ GeV/c and Helix $|dr| < 1$ cm, $|dz| < 5$ cm
We assume the pion mass for all charged particles.
ECL cluster: $E_{\rm ECL} > 0.1$ GeV
Gamma: $E_{\rm ECL} > 0.1$ GeV
$E_{\rm rec}$ = Sum of $P^{\rm CM}_{\rm charged\ track}$ + Sum of $E^{\rm CM}_{\rm gamma}$
$Pt_{\rm max}$: maximum P_t among charged tracks in the laboratory frame
$E_{\rm tot} = E_{\rm rec} + |P^{\rm CM}_{\rm miss}|$; assume a massless particle for $P_{\rm miss}$ to boost to the CM frame
$N_{\rm barrel}$: Numer of tracks with $30^\circ < \theta < 130^\circ$ (barrel region)
$E_{\rm ECLtrk}$ = Sum of $E^{\rm CM}_{\rm ECL}$ − Sum of $E^{\rm CM}_{\rm gamma}$

Selection criteria

1) $2 \leq$ Number of charged tracks ≤ 8
2) $|$charge sum$| \leq 2$
3) Sum of $P^{\rm CM}_{\rm chargedtrack} < 10$ GeV/c
4) Sum of $E_{\rm ECL} < 10$ GeV
5) $Pt_{\rm max} > 0.5$ GeV/c
6) Event vertex $|r| < 0.5$ cm,$|z| < 3$ cm
7) For 2 track event
   7-1) Sum of $P^{\rm CM}_{\rm chargedtrack} < 9$ GeV/c
   7-2) Sum of $E_{\rm ECL} < 9$ GeV
   7-3) $5^\circ < \theta_{\rm missing\ momentum} < 175^\circ$
8) $E_{\rm rec} > 3$ GeV .or. $Pt_{\rm max} > 1.0$ GeV/c
9) For the 2-4 charged track case
   9-1) $E_{\rm tot} < 9$ GeV .or. maximum opening angle $< 175^\circ$
   9-2) $N_{\rm barrel} \geq 2$ .or. $E_{\rm ECLtrk} < 5.3$ GeV
10) Maximum opening angle $> 20^\circ$

C.1 Situation

In the environment of the Belle experiment, which works on the $\Upsilon(4S)$ resonance with a high luminosity, we obtain much data which contain $B\bar{B}$, continuum, Bhabha, $\mu\mu$, 2-photons, beam background and $\tau\tau$ processes. In order to reduce the data into a reasonable size for a τ physics analysis, the selection criteria are set, as described in the next section.

In the Belle experiment, the τ data are shared with the hadronic skim-files. If an event satisfies the τ selection criteria and the hadronic skim's criteria simultaneously, it is stored in the hadronic skim-file. A τ event with multi-hadronic decay tends to be stored in hadronic skim-files. Because of this situation, we are not care about reducing the hadronic events by τ pre-selection.

Because of the reconstruction scheme, there are three skim-files for the τ events, named `TauPair`, `tau_skimA` and `HadronB`. `HadronB` is a hadronic skim-file which includes the τ events in part. `tau_skimA` is for the τ events that are selected as another hadronic skim `HadronA`, but not selected as `HadronB`. `TauPair` contains the remaining τ events. In the analysis, we need to accumulate τ events from these files.

In the following study, we use mainly the MC events and partly pilot data to see the beam background contribution.

C.2 Criteria

1) $2 \leq$ **Number of charged tracks** ≤ 8 (Figure C.1)
2) $|\text{charge sum}| \leq 2$

The τ decay to one charged track mode shows a high branching ratio. Therefore, the τ events include many two-charged-tracks events. An event which includes 2 to 8 charged tracks and $|\text{charge sum}| \leq 2$, is selected.

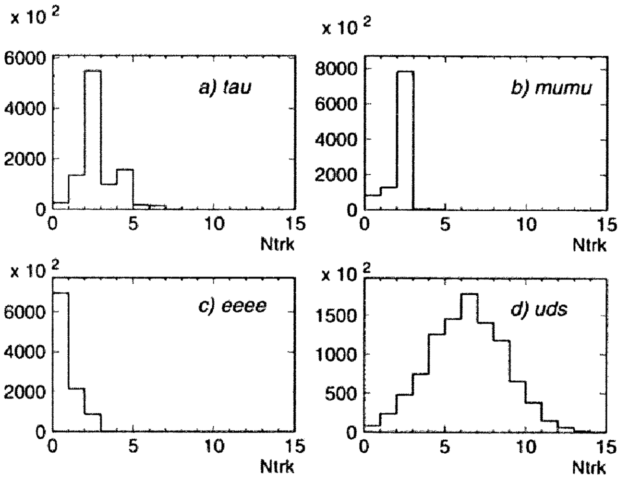

Figure C.1: Number of detected charged tracks for a) $\tau\tau$ events, b) $\mu\mu$ events, c) 2-photon ($eeee$) and d) continuum (uds).

3) Sum of $P^{\text{CM}} < 10$ **GeV/**c (Figure C.2)

4) Sum of $E_{\mathrm{ECL}} < 10$ GeV

This criterion is required to reject $\mu\mu$ and Bhabha events. In this selection, most $\mu\mu$ and Bhabha events are rejected, but the τ events are not significantly affected. The radiative $\mu\mu$ and Bhabha events remain.

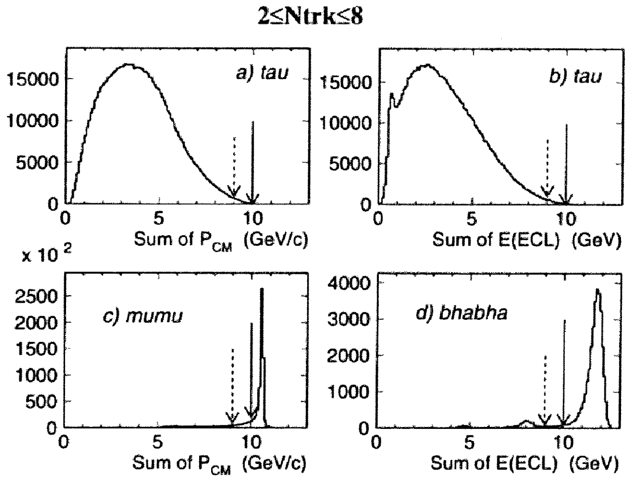

Figure C.2: Sum of momentum in the CM frame for a) τ events and c) $\mu\mu$ events, and sum of the energy measured in ECL for b) τ events and d) Bhabha with the cut-1. The arrows show the selection boundary of cut-3. The arrows with a dashed line define the boundary for 2-track events (cut-7).

5) $Pt_{\max} > 0.5$ **GeV/c** (Figure C.3)

Because 2-photon events include many low-P_t tracks, they can be removed by the high-P_t requirement. The τ events in which all charged tracks have a low P_t are not considered to be very important for physics analysis. Therefore, such events are rejected by this selection.

6) Event vertex $|r| < 0.5$ cm,$|z| < 3$ cm (Figure C.5)

It is necessary to reject the clear beam background events, in this selection.

7) For 2 track event

7-1) Sum of $P^{\mathrm{CM}} < 9$ GeV/c (Figure C.2)

7-2) Sum of $E_{\mathrm{ECL}} < 9$ GeV

Although a similar selection is required in cut-3 and 4, many Bhabha events remain because of the high cross section. Therefore, a tighter selection is required again for 2-track events.

7-3) $5° < \theta_{\text{missing momentum}} < 175°$ (Figure C.4)

In the radiative $\mu\mu$ and Bhabha events, many photons fly out in the beam-pipe direction. In 2-photon events, e^+ and e^- go in the beam direction. Therefore, in this selection radiative $\mu\mu$, Bhabha events and 2-photon events are rejected.

8) $E_{\mathrm{rec}} > 3$ **GeV .or.** $Pt_{\max} > 1.0$ **GeV/c** (Figure C.5)

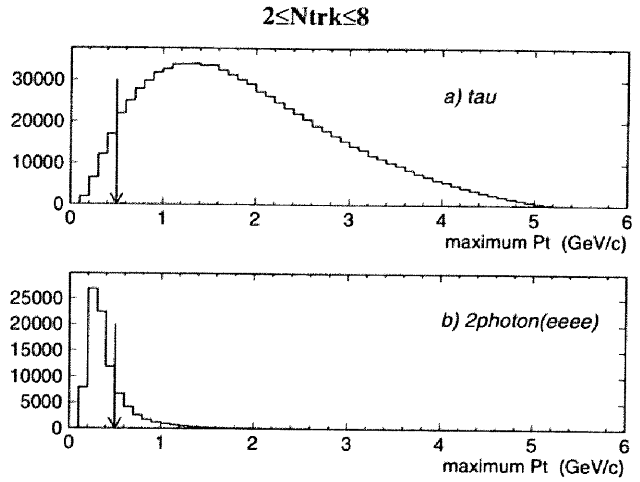

Figure C.3: Maximum Pt among the charged tracks for a) τ events and b) 2-photon ($eeee$). The arrows show the selection boundary.

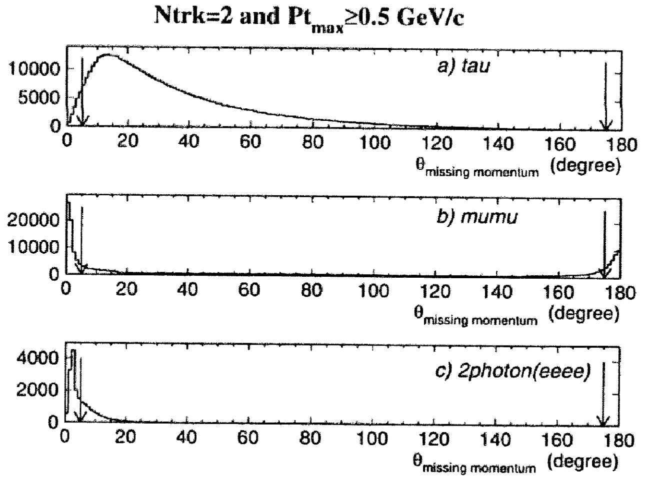

Figure C.4: Polar angle of the missing momentum for a) τ events, b) $\mu\mu$ events and c) 2-photon ($eeee$) with the cut-5). The arrows show the selection boundary.

This is used to reduce more 2-photon and beam-background events. The 2-photon and beam-background events show a low energy of the reconstructed particles and a low P_t. On the other hand, the τ events distribute in the high-energy, high-P_t region. By this selection, many background events can be removed, though some τ events are also lost. However, the rejected τ events are of low priority in the analysis.

9) For the 2-4 charged track case

9-1) $E_{tot} < 9$ **GeV .or. maximum opening angle**$< 175°$ (Figure C.6)

Because many Bhabha events still remain, this selection is required. The remaining

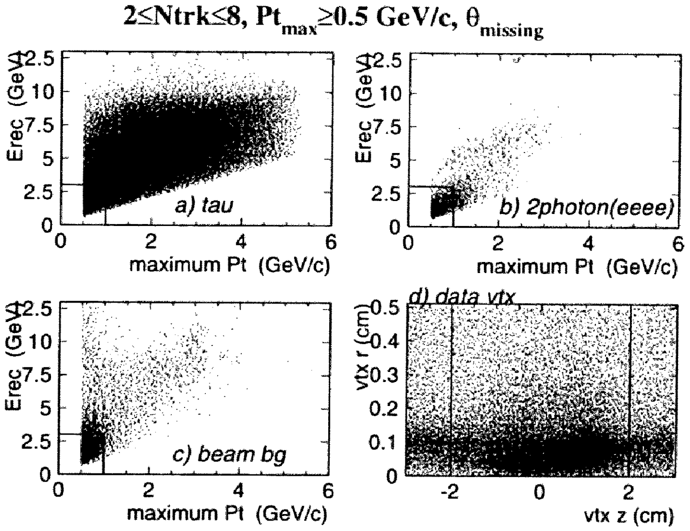

Figure C.5: 2D plot of $E_{\rm rec}$ and the maximum Pt for a) τ events, b) 2-photon ($eeee$) and c) beam background with cut-1 to 7. The beam background events are selected with an event vertex of $|z| > 2$cm, as plotted in d). The lines show the selection boundary.

Bhabha events include the missed radiative photon that flys to the gap of the ECL detector. The value $E_{\rm tot}(= E_{\rm rec} + |P_{\rm miss}^{\rm CM}|)$ shows the beam energy if the missing momentum has no effective mass. In the case of lepton-flavor-violating decay (LFV) of the τ lepton with hadronic decay on the tag side, the missing particle almost becomes one neutrino, whose mass is nearly zero. Therefore, selection by the opening angle of the charged tracks is also required. With this requirement fulfilled, the LFV modes are saved.

9-2) $N_{\rm barrel} \geq 2$ **.or.** $E_{\rm ECLtrk} < 5.3$ **GeV** (Figure C.7)

The remaining Bhabha events include many particles going to the endcap region and the missed gamma with higher momentum. Therefore, the radiative Bhabha events are removed by this selection.

10) Maximum opening angle> 20° (Figure C.8)

A strange Bhabha event can be rejected by this selection. Rejected Bhabha samples include many miss-track events and shower-like events. Miss-track means that the one charged track is reconstructed as two tracks.

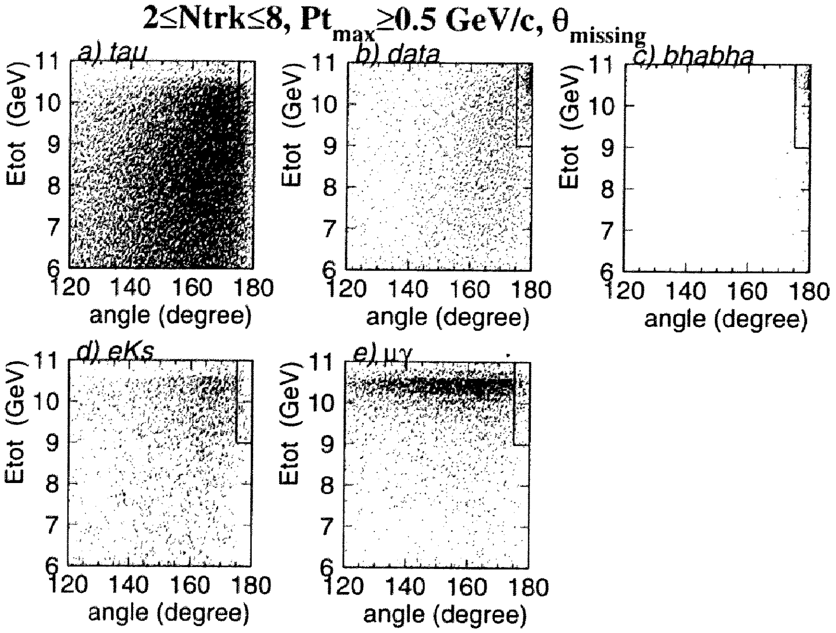

Figure C.6: 2D plot of $E_{\rm tot}$ and the maximum opening angle among the charged tracks for a) τ events, b) exp.3 pilot data, c) Bhabha, d) $\tau \to eK_s$ and e) $\tau \to \mu\gamma$. The lines show the selection boundary.

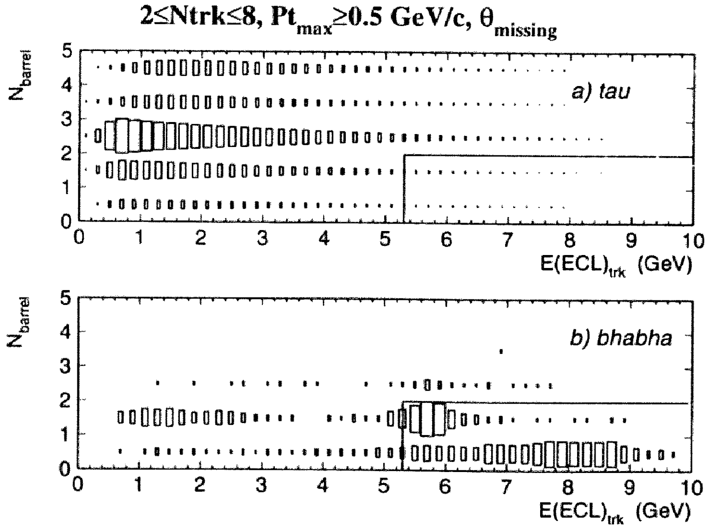

Figure C.7: 2D plot of $N_{\rm barrel}$ and $E_{\rm ECLtrk}$ for a) τ events and b) Bhabha. The lines show the selection boundary.

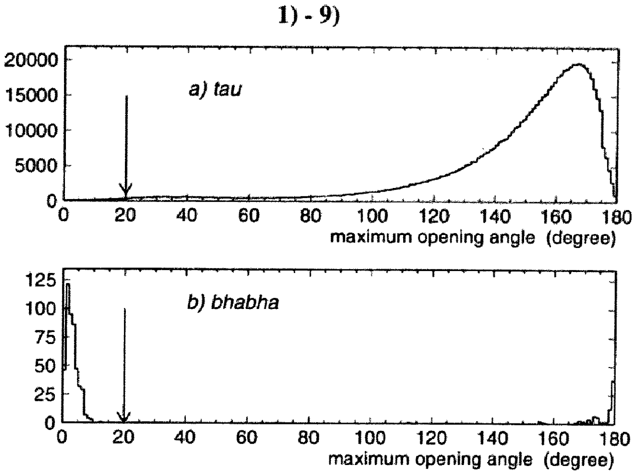

Figure C.8: Maximum opening angle for a) τ event and b) Bhabha. The arrows show the selection boundary.

C.3 Efficiency and reduction power

The efficiencies and cross sections are summarized in Table C.1. The effective cross section of non-tau processes are reduced to a reasonable level, except for hadronic processes.

Table C.1: Efficiencies and cross sections evaluated by MC.

	$\tau\tau$	$\mu\mu$	Bhabha	*eeee*	*eeuu*	*uds*
Cross section (nb)	0.91	1.05	1249	40.85	11.7	2.09
Efficiency (%)						
cut-1 to 5	80.1	20.7	0.21	2.1	3.9	77.7
cut-1 to 7	78.1	6.4	0.13	0.90	2.3	77.1
cut-1 to 9-1	72.6	5.8	0.036	0.41	0.80	71.2
cut-1 to 10	70.2	5.7	0.0011	0.24	0.56	70.7
Effective cross section (nb)	0.639	0.060	0.014	0.098	0.065	1.48

The rates of the number of events in three skim files for each mode are listed in Table C.2. Most of the τ events are stored in the `TauPair` and `tau_skimA`. Because the hadronic events in the `TauPair` and `tau_skimA` are not very large, we do not care about the rejection of hadronic processes.

Table C.2: Event rates in three skims for each modes evaluated by MC.

(%)	$\tau\tau$	$\mu\mu$	Bhabha	*eeee*	*eeuu*	*uds*
`TauPair`	67.1	97.0	91	88.4	37.7	3.2
`tau_skimA`	26.5	1.2	9	10.6	18.6	6.5
`HardonB`	6.4	1.8	0	1.1	43.7	90.3

Appendix D

Level-1 trigger

D.1 Level-1 trigger logic

The Belle hardware trigger system [25] consists of sub-detector trigger systems and the central trigger system called Global Decision Logic (GDL). The sub-detector trigger systems produce the output to GDL as follows.

name		definitions
CDC r-ϕ		
ncdr_full	:	Number of full tracks (Pt>0.2GeV/c)
ncdr_short	:	Number of short tracks
cdc_bb	:	Back to back topology by CDC
cdc_open	:	Minimum opening angle (135 degree)
CDC z		
ncdz	:	Number of tracks by CDC z trigger
TOF(TSC)		
tsc_mult	:	Multiplicity by TSC
tsc_pat	:	TSC hit pattern
ntsc	:	Number of TSC hit
tsc_timing	:	Trigger timing by TSC
ECL		
csi_timing	:	Trigger timing by ECL
e_high	:	Energy trigger (E>1GeV)
e_low	:	Energy trigger (E>0.5GeV)
e_lum	:	Energy trigger for luminosity measurement (E>3GeV)
csi_bb	:	Back to back topology by ECL (for Bhabha)
csi_bbpre	:	Back to back with 1/10 pre-scale.
nicl	:	Number of ECL cluster hits
csi_cosmic	:	Cosmic topology by ECL
KLM		
klm_fwd	:	Forward endcap
klm_bwd	:	Backward endcap
klm_brl	:	Barrel
EFC		
efc_bb	:	Back to back topology by EFC
efc_tag	:	EFC tag

The GDL system makes global correlation of 48 input from the sub trigger systems and output up to 48 types of event trigger signals as follows.

FTDL logic (version 4.8)

bit	mnemonic	definitions
0	ff_zt2oc	(ncdr_full>1)&cdc_open&(ntsc>1)&(ncdz>0)&csi_timing&!csi_bb
1	ff_t2oc	(ncdr_full>1)&cdc_open&(ntsc>1)&csi_timing&!csi_bb
2	fs_ztoc	(ncdr_short>1)&(ncdr_full>0)&cdc_open&(ntsc>0)&(ncdz>0)&csi_timing&!csi_bb
3	fs_toc	(ncdr_short>1)&(ncdr_full>0)&cdc_open&(ntsc>0)&csi_timing&!csi_bb
4	ffs_zt2	(ncdr_short>2)&(ncdr_full>1)&(ntsc>1)&(ncdz>0)
5	ffs_zt2oc	(ncdr_short>2)&(ncdr_full>1)&(ntsc>1)&(ncdz>0)&cdc_open&csi_timing
6	fff_ot2c2z	(ncdr_full>2)&cdc_open&(ntsc>1)&(nicl>1)&(ncdz>0)
7	fff_ot2c2	(ncdr_full>2)&cdc_open&(ntsc>1)&(nicl>1)
8	ffs_t2	(ncdr_short>2)&(ncdr_full>1)&(ntsc>1)
9	ffs_t2oc	(ncdr_short>2)&(ncdr_full>1)&(ntsc>1)&cdc_open&csi_timing
10	fsss_ztoc	(ncdr_short>3)&(ncdr_full>0)&(ntsc>0)&(ncdz>0)&cdc_open&csi_timing
11	fsss_toc	(ncdr_short>3)&(ncdr_full>0)&(ntsc>0)&cdc_open&csi_timing
12	hie	e_high&!csi_bb&!csi_cosmic
13	clst4	(nicl>3)&!csi_cosmic
14	loe_clst3	e_low&(nicl>2)&!csi_cosmic
15	loe_trk2	e_low&(ncdr_short>1)&((ncdr_full>0)#(ncdz>0))&cdc_open&!csi_bb
16	two_photon	efc_tag&(ncdr_short>1)&(ncdr_full>0)
17	csi_bhabha_p	csi_bbpre
18	csi_bhabha	csi_bb
19	csi_lum_e	e_lum
20	efc_bhabha	efc_bb
21	tof_b2b	tsc_pat
22	abe_bhabha	csi_bb&cdc_bb
23	dimu_noz	cdc_bb&(tsc_pat#(nicl>1))
24	klm_opn	cdc_open&(klm_brl#klm_fwd#klm_bwd)
25	klm_b2b	cdc_bb&(klm_brl#klm_fwd#klm_bwd)
26	random	(calib0)
27	clst5	(nicl>4)&!csi_cosmic
28	short_gt_1	(ncdr_short>1)
29	short_gt_2	(ncdr_short>2)
30	hadronb	(ncdr_short>2)&(ncdr_full>0)&(ncdz>0)&e_low&(nicl>1)&(ntsc>0)
31	ff_zt2c	(ncdr_full>1)&(ntsc>1)&(ncdz>0)&csi_timing&!csi_bb
32	loe_fs_z	e_low&(ncdr_short>1)&(ncdr_full>0)&(ncdz>0)&!csi_bb
33	cdcbb	cdc_bb
34	gphi	e_lum&(ncdr_short>1)&!cdc_open
35	loe	e_low
36	clst2	(nicl>1)
37	tof_multi	tsc_mult
38	revol	misc_in
39	clst2_o	(nicl>1)&cdc_open&!csi_bb
40	hadron	(ncdr_short>2)&e_low&(nicl>1)&(ntsc>0)
41	efc	efc_tag&(nicl>1)
42	e_hi_clst4	(nicl>3)&e_high
43	hadronc	(ncdr_short>2)&(ncdr_full>1)&cdc_open&e_high&(nicl>2)&(ntsc>0)
44	loe_fs_oz	e_low&(ncdr_short>1)&(ncdr_full>0)&cdc_open&(ncdz>0)&!csi_bb
45	dimu_z	cdc_bb&(tsc_pat#(nicl>1))&(ncdz>0)
46	clst2_oz	(nicl>1)&cdc_open&(ncdz>0)&!csi_bb
47	e_had	e_lum&!csi_bb

D.2 Trigger in the analysis

Because the hardware trigger condition should be applied to MC samples, a trigger simulator, Tsim, is prepared. However, Tsim for EFC (and some others) has not worked completely. Therefore, in the analysis, the related trigger bits are not used. Furthermore, the bits, whose definition is changed during the experimental period, are masked. The masked trigger bits are bit16, bit17, bit20, bit26, bit31, bit32 and bit41. As shown in Figure D.1, the contribution of these trigger bits is small. Therefore, the effect of this mask is negligible.

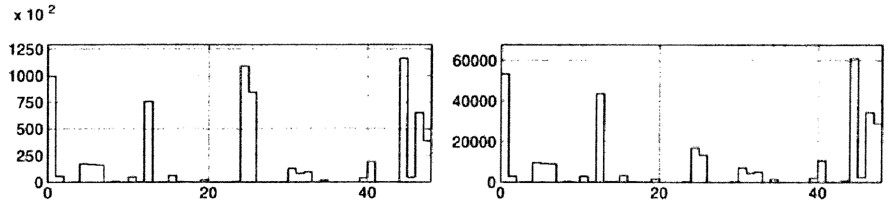

Figure D.1: Hit histograms of the trigger bit for the $e^+\mu^-$ mode(left) and $e^+\pi^-$ mode(right).

D.3 Effect of the trigger

The effect of the L1 trigger for the analysis is checked. Figures D.2 and D.3 show the distributions and the ratios of the momentum and $\cos\theta$ in the laboratory system with and without the trigger requirement, evaluated by the MC simulation for the $e\mu$ mode. Due to the P_t threshold of the track trigger, the low-momentum part is reduced. Figure D.4 shows the opening-angle distribution between two charged tracks in the r-ϕ plane. The small opening-angle part ($< 130°$) is reduced due to the requirement of the cdc_open trigger.

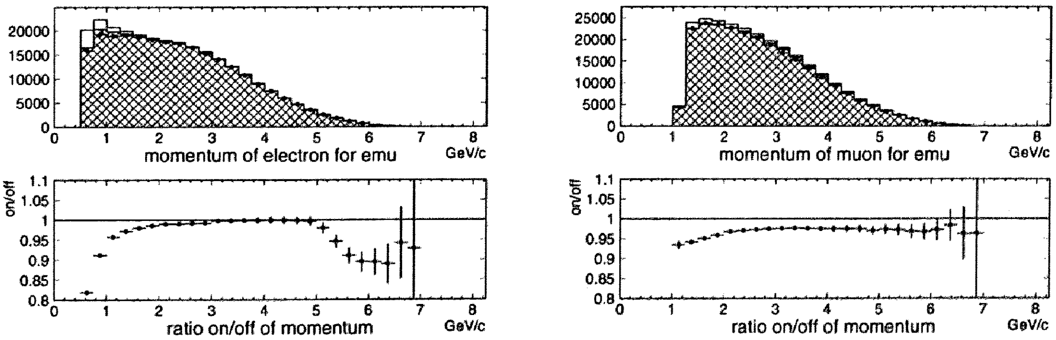

Figure D.2: Momentum distribution in the laboratory frame of the electron (left) and the muon (right) for the $e\mu$ mode. The blank histogram is τ-pair MC event without the trigger requirement, the hatch histogram is MC with the trigger requirement and the dots are the experimental data. The MC histograms are normalized by the integrated luminosity. The lower plots show the ratios of the hatch histogram divided by the blank histogram.

Table D.1 gives the trigger efficiencies for each mode used in the analysis evaluated by the MC. The efficiency is more than 93%.

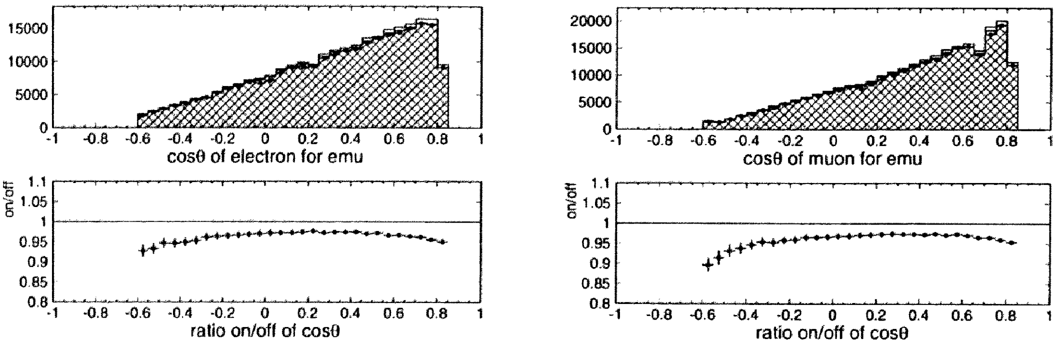

Figure D.3: $\cos\theta_{\mathrm{lab.}}$ distribution of the electron (left) and the muon (right) for the $e\mu$ mode. The blank histogram is τ-pair MC event without the trigger requirement, the hatch histogram is MC with the trigger requirement and the dots are the experimental data. The MC histograms are normalized by the integrated luminosity. The lower plots show the ratios of the hatch histogram divided by the blank histogram.

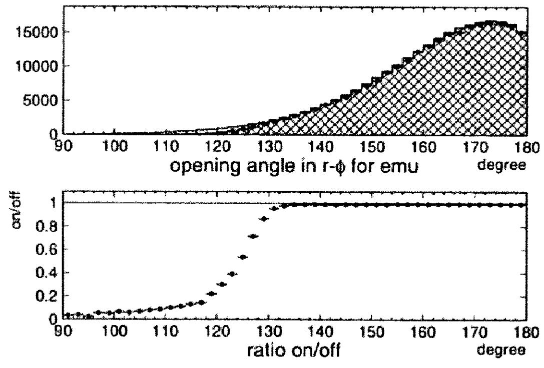

Figure D.4: Distribution of the opening angle between two charged tracks in the r-ϕ plane for the $e\mu$ mode. The blank histogram is τ-pair MC event without the trigger requirement, the hatch histogram is MC with the trigger requirement and the dots are the experimental data. The MC histograms are normalized by the integrated luminosity. The lower plot shows the ratio of the hatch histogram divided by the blank histogram.

Table D.1: Trigger efficiencies evaluated by MC.

mode	$e\mu$	$e\pi$	$\mu\pi$	$e\rho$	$\mu\rho$	$\pi\rho$	$\rho\rho$	$\pi\pi$
efficiency(%)	96.6	95.0	95.1	93.1	98.5	97.5	97.5	95.0

Appendix E

Sensitivity and offset

E.1 Observable

The mean value of the optimal observable is approximately calculated as

$$\langle \mathcal{O} \rangle \sim \int \Sigma_1 d\phi + \lambda \int \left(\frac{\Sigma_1}{\Sigma_0} \right)^2 \Sigma d\phi, \tag{E.1}$$

where the differential cross section is denoted by

$$\Sigma d\phi = [\Sigma_0(\phi) + \lambda \Sigma_1(\phi)] d\phi,$$

with the phase-space parameter ϕ. λ is a small parameter which we measure; it is the electric dipole moment d_τ in this analysis. The first term, $\int \Sigma_1 d\phi$, gives the offset and the second term, $\int (\frac{\Sigma_1}{\Sigma_0})^2 \Sigma d\phi$, gives the sensitivity.

Figure 5.13 shows the sensitivities, a_{Re} and a_{Im}, and the offsets, b_{Re} and b_{Im}, obtained in the analysis. In the following, qualitative discussions of parameters a and b are presented.

E.2 Parameters

In the analysis, the observables $\mathcal{O}_{Re}$ and $\mathcal{O}_{Im}$ are formed as

$$\mathcal{O}_{Re} = \frac{\mathcal{M}^2_{Re}}{\mathcal{M}^2_{\rm SM}}, \quad \mathcal{O}_{Im} = \frac{\mathcal{M}^2_{Im}}{\mathcal{M}^2_{\rm SM}}. \tag{E.2}$$

These are functions of the spin-momentum correlation terms: $(\boldsymbol{S}_+ \times \boldsymbol{S}_-) \cdot \hat{\boldsymbol{k}}$, $(\boldsymbol{S}_+ \times \boldsymbol{S}_-) \cdot \hat{\boldsymbol{p}}$, $(\boldsymbol{S}_+ - \boldsymbol{S}_-) \cdot \hat{\boldsymbol{k}}$ and $(\boldsymbol{S}_+ - \boldsymbol{S}_-) \cdot \hat{\boldsymbol{p}}$. The major terms are given as

$$\mathcal{M}^2_{Re} \propto \; -(m_\tau + (k_0 - m_\tau)(\hat{\boldsymbol{k}} \cdot \hat{\boldsymbol{p}})^2)(\boldsymbol{S}_+ \times \boldsymbol{S}_-) \cdot \hat{\boldsymbol{k}} \; + k_0 (\hat{\boldsymbol{k}} \cdot \hat{\boldsymbol{p}})(\boldsymbol{S}_+ \times \boldsymbol{S}_-) \cdot \hat{\boldsymbol{p}}, \tag{E.3}$$

$$\mathcal{M}^2_{Im} \propto \; -(m_\tau + (k_0 - m_\tau)(\hat{\boldsymbol{k}} \cdot \hat{\boldsymbol{p}})^2)(\boldsymbol{S}_+ - \boldsymbol{S}_-) \cdot \hat{\boldsymbol{k}} \; + k_0 (\hat{\boldsymbol{k}} \cdot \hat{\boldsymbol{p}})(\boldsymbol{S}_+ - \boldsymbol{S}_-) \cdot \hat{\boldsymbol{p}}. \tag{E.4}$$

These terms show the characteristics of CP-odd/T-odd for the real part and CP-odd/T-even for the imaginary part. Here, $\hat{\boldsymbol{p}}$ is the unit vector of the e^+-beam momentum and $\hat{\boldsymbol{k}}$ is defined as the unit vector of the τ flight direction, given by

$$\hat{\boldsymbol{k}}^{\pm} = \tilde{u} \boldsymbol{p}_+ + \tilde{v} \boldsymbol{p}_- \pm \tilde{w} (\boldsymbol{p}_+ \times \boldsymbol{p}_-), \tag{E.5}$$

where $\boldsymbol{p}_+$ and $\boldsymbol{p}_-$ are the three-momentum vectors of the daughter particles. The coefficients $\tilde{u}$, $\tilde{v}$ and $\tilde{w}$ are expressed using the energy and magnitude of the momenta of the daughter particle and its mother τ. The τ direction can be reconstructed to be two cross lines of two cones, which are obtained from the momenta of the daughter particles. For the leptonic mode, there is one more ambiguity because of an additional missing neutrino. Therefore, the τ direction can be calculated with a two-fold (or more) ambiguity.

The structure of the spin-vector $\boldsymbol{S}_\pm$ is written as the following form:

$$\boldsymbol{S}_\pm(\tau \to l^\pm \nu_l \nu_\tau) = \alpha^l_\pm \boldsymbol{p}_{l^\pm} + \beta^l_\pm \boldsymbol{k}, \tag{E.6}$$

$$\boldsymbol{S}_\pm(\tau \to \pi^\pm \nu_\tau) = \alpha^\pi_\pm \boldsymbol{p}_{\pi^\pm} + \beta^\pi_\pm \boldsymbol{k} \quad = \pm\alpha^\pi \boldsymbol{p}_{\pi^\pm} + \beta^\pi_\pm \boldsymbol{k}, \tag{E.7}$$

$$\boldsymbol{S}_\pm(\tau \to \rho^\pm \nu_\tau \to \pi^\pm \pi^0 \nu_\tau) = \alpha^\rho_\pm \boldsymbol{H}_\pm + \beta^\rho_\pm \boldsymbol{k}, \tag{E.8}$$

where the coefficients α and β are functions of the momenta of the measured daughter particles and the assumed τ direction. $\boldsymbol{H}_\pm$ is given using a combination of the momenta of the π and π^0 as

$$(H_\pm)^\nu = 2(p_{\pi^\pm} - p_{\pi^0})^\nu (p_{\pi^\pm} - p_{\pi^0})^\mu (\pm k)_\mu + (p_{\pi^\pm} + p_{\pi^0})^\nu (p_{\pi^\pm} - p_{\pi^0})^2.$$

The magnitude of the spin vectors for the hadronic decays is defined to be one. On the other hand, for leptonic decays, the magnitude is not necessarily one because of its low spin-analyzing power due to the missing neutrinos.

E.3 Offset

As mentioned above, the offsets arise from the term

$$\int \Sigma_1 d\phi \sim \int \mathcal{M}^2_{Re,Im} d\phi, \tag{E.9}$$

integrated over the experimentally limited acceptance. As shown in Figure 5.13, the offset values for the real part, b_{Re}, are consistent with zero within the statistical errors, while the offset values for the imaginary part, b_{Im}, are non-zero. It relates to the structure of the amplitudes, $\mathcal{M}^2_{Re,Im}$. From Eq.(E.3) and Eq.(E.4), we can find its characteristics, which are also described in Section 2.2.3: $\mathcal{M}^2_{Re}$ shows the rotation asymmetry around the beam and the τ flight direction, and $\mathcal{M}^2_{Im}$ shows the forward/backward asymmetry along the beam and the τ direction. Because Belle is a forward/backward asymmetric detector, there is an asymmetry of $\mathcal{M}^2_{Im}$ intrinsically. Therefore, the offsets for the imaginary part are non-zero.

E.3.1 $\pi\pi$

For the $\pi\pi$ mode, the second term of Eq.(E.4) contributes to the large offset, b_{Im}. From Eq.(E.4) and Eq.(E.7), the following expression can be extracted:

$$\begin{aligned}(\boldsymbol{S}_+ - \boldsymbol{S}_-)\cdot\hat{\boldsymbol{p}} &= \alpha^\pi(\boldsymbol{p}_{\pi^+}\cdot\hat{\boldsymbol{p}} + \boldsymbol{p}_{\pi^-}\cdot\hat{\boldsymbol{p}}) + (\beta^\pi_+ - \beta^\pi_-)\boldsymbol{k}\cdot\hat{\boldsymbol{p}},\\ &= \alpha^\pi(|\boldsymbol{p}_{\pi^+}|\cos\theta_+ + |\boldsymbol{p}_{\pi^-}|\cos\theta_-) + (\beta^\pi_+ - \beta^\pi_-)\boldsymbol{k}\cdot\hat{\boldsymbol{p}},\end{aligned} \tag{E.10}$$

where $\theta_\pm$ is the polar angle of the $\pi^\pm$. Figure E.1 shows the $\cos\theta_\pm$ distribution. Because of the particle selection criteria, the distribution become asymmetric. Therefore, the first term of Eq.(E.10) clearly shows a non-zero value.

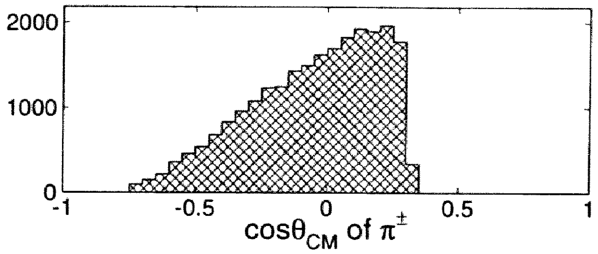

Figure E.1: $\cos\theta_\pm$ distribution for the $\pi\pi$ mode in the CM frame.

E.3.2 $\pi\rho$, $l\pi$

The offsets for the $\pi\rho$ and $l\pi$ modes arise because of the combination of two types of charge asymmetry, which are the charge asymmetries of the observable $\mathcal{O}_{Im}$ and the efficiency.

For the $\pi^+\rho^-$ mode, the term $(\boldsymbol{S}_+ - \boldsymbol{S}_-)\cdot\hat{\boldsymbol{k}}$ tends to be minus because the requirement of the high momentum π^+ makes the product $\boldsymbol{S}_+\cdot\hat{\boldsymbol{k}}$ to be minus, and because the spin direction of the ρ^- does not largely correlate with its momentum. The term $(\hat{\boldsymbol{k}}\cdot\hat{\boldsymbol{p}})(\boldsymbol{S}_+ - \boldsymbol{S}_-)\cdot\hat{\boldsymbol{p}}$ tends to be plus because of the polar-angle selection. Therefore, $\mathcal{M}^2_{Im}$ tends to be plus for the $\pi^+\rho^-$ mode. For the $\rho^+\pi^-$ mode, $\mathcal{M}^2_{Im}$ tend to be minus for the same reasons. Figure E.2 shows the distribution of $\mathcal{O}_{Im}$ for the $\pi\rho$ mode. It clearly represents the charge asymmetry of the observables.

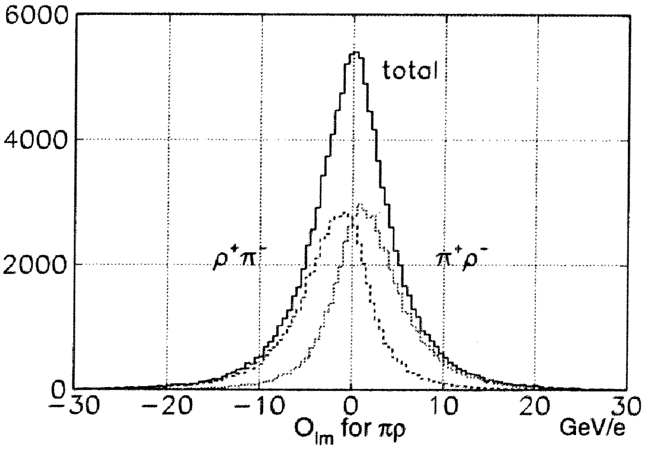

Figure E.2: $\mathcal{O}_{Im}$ of the $\pi\rho$ mode. The solid line shows the total sample, the dashed line is for the $\rho^+\pi^-$ mode and the dotted line is for the $\pi^+\rho^-$ mode.

The offset does not become non-zero only due to the charge asymmetry of the observables. It is because two distributions of the observables are symmetric. In addition to the asymmetry of the observables, the charge asymmetry of the efficiency is produced by the particle selections. One reason is because of the small forward/backward asymmetry of the τ-pair production due to the Z^0 effect and the requirement of the polar-angle. Figure E.3

shows the cosine of the polar angle distribution of the $\tau^{\pm}$. The forward/backward asymmetry can be found at the 2% level. Another reason is because of the charge asymmetry in the detector efficiency.

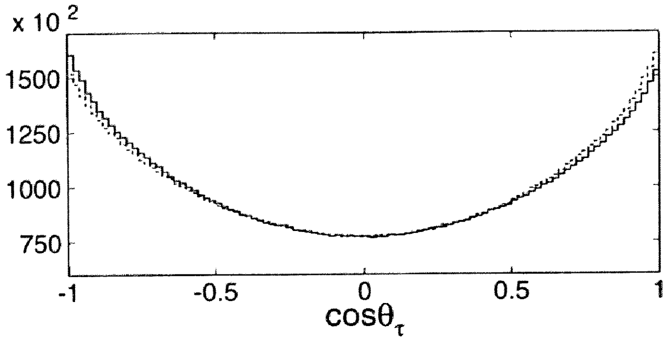

Figure E.3: $\cos\theta$ distribution of the $\tau^{\pm}$ in CM frame. The solid line and the dashed line show τ^{+} and τ^{-}, respectively.

For these two reasons, the offsets become non-zero. For the $l\pi$ mode, the situation is similar. The $\pi^{\pm}$ selection mostly affects the non-zero offsets.

E.4 Sensitivity

Approximately, the sensitivity is obtained as $\int(\frac{\Sigma_1}{\Sigma_0})^2\Sigma d\phi$, which is the mean of the squared observable. Therefore, the width of the observable distribution is directly correlated with the sensitivity.

Generally, the sensitivity for the leptonic decay modes is less than that for the hadronic decay modes, because the spin-analyzing power of the leptonic decay channel is low due to the missing neutrinos.

E.4.1 Real part vs. imaginary part

Comparing the sensitivity for the real part, a_{Re}, with that for the imaginary part, a_{Im}, we can find that a_{Im} is about 3-10 times larger than a_{Re}. This is due to the applicable range of the spin-momentum correlation terms and the relation between the $\mathcal{M}^2_{Re,Im}$ and $\mathcal{M}^2_{\rm SM}$ terms.

Figure E.4 shows the distributions of the spin-momentum correlation terms for the $\rho\rho$ mode. The index "±" shows the ambiguity of the τ direction $\boldsymbol{k}^{\pm}$. The distribution of the terms $(\boldsymbol{S}_+ - \boldsymbol{S}_-)\cdot\hat{\boldsymbol{k}}$ and $(\boldsymbol{S}_+ - \boldsymbol{S}_-)\cdot\hat{\boldsymbol{p}}$ is wider than that of $(\boldsymbol{S}_+ \times \boldsymbol{S}_-)\cdot\hat{\boldsymbol{k}}$ and $(\boldsymbol{S}_+ \times \boldsymbol{S}_-)\cdot\hat{\boldsymbol{p}}$.

Figure E.5 shows the relation between the the amplitude $\mathcal{M}^2_{Re,Im}$ and $\mathcal{M}^2_{\rm SM}$. From this figure, the correlation between $\mathcal{M}^2_{Re}$ and $\mathcal{M}^2_{\rm SM}$ works to reduce $\mathcal{O}_{Re}$, while the correlation between $\mathcal{M}^2_{Im}$ and $\mathcal{M}^2_{\rm SM}$ does not work so. This is because of the characteristic of the product terms: $\boldsymbol{S}_\pm\cdot\hat{\boldsymbol{k}}$, $\boldsymbol{S}_\pm\cdot\hat{\boldsymbol{p}}$, $(\boldsymbol{S}_+ \times \boldsymbol{S}_-)\cdot\hat{\boldsymbol{k}}$ and $(\boldsymbol{S}_+ \times \boldsymbol{S}_-)\cdot\hat{\boldsymbol{p}}$.

E.4.2 Real part

The structure of the spin vectors of the lepton and pion can be written as

$$\boldsymbol{S}_\pm = \alpha_\pm \boldsymbol{p}_\pm + \beta_\pm \boldsymbol{k}. \tag{E.11}$$

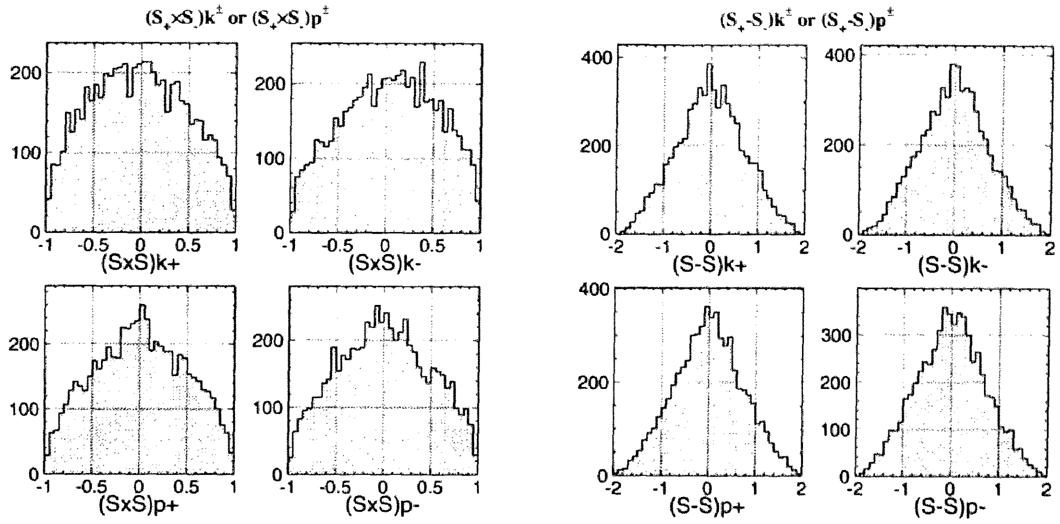

Figure E.4: Spin-momentum correlation distributions for the $\rho\rho$ mode. The left four figures show the distributions of the correlation terms proportional to $\mathcal{O}_{Re}$ and the right four figures are that for $\mathcal{O}_{Im}$. The index "±" means the case for $\hat{\boldsymbol{k}}^{\pm}$.

For the $\pi\pi$, πl and ll modes, the term $(\boldsymbol{S}_{+} \times \boldsymbol{S}_{-}) \cdot \boldsymbol{k}$ can be calculated as

$$
\begin{aligned}
(\boldsymbol{S}_{+} \times \boldsymbol{S}_{-}) \cdot \boldsymbol{k} &= \alpha_{+}\alpha_{-}(\boldsymbol{p}_{+} \times \boldsymbol{p}_{-}) \cdot \boldsymbol{k} + \alpha_{+}\beta_{-}(\boldsymbol{p}_{+} \times \boldsymbol{k}) \cdot \boldsymbol{k} \\
&\quad + \beta_{+}\alpha_{-}(\boldsymbol{k} \times \boldsymbol{p}_{-}) \cdot \boldsymbol{k} + \beta_{+}\beta_{-}(\boldsymbol{k} \times \boldsymbol{k}) \cdot \boldsymbol{k}, && \text{(E.12)} \\
&= \alpha_{+}\alpha_{-}(\boldsymbol{p}_{+} \times \boldsymbol{p}_{-}) \cdot (\tilde{u}\boldsymbol{p}_{+} + \tilde{v}\boldsymbol{p}_{-} \pm \tilde{w}(\boldsymbol{p}_{+} \times \boldsymbol{p}_{-})), && \text{(E.13)} \\
&= \alpha_{+}\alpha_{-}(\pm\tilde{w})|\boldsymbol{p}_{+} \times \boldsymbol{p}_{-}|^{2}. && \text{(E.14)}
\end{aligned}
$$

The coefficients $\alpha_{\pm}$ do not depend on the sign of the τ direction $\boldsymbol{k}^{\pm}$. Therefore, the term $(\boldsymbol{S}_{+} \times \boldsymbol{S}_{-}) \cdot \hat{\boldsymbol{k}}$ is counteracted by averaging over the ambiguity of the τ direction. Figure E.6 shows the correlation between $(\boldsymbol{S}_{+} \times \boldsymbol{S}_{-}) \cdot \hat{\boldsymbol{k}}^{+}$ and $(\boldsymbol{S}_{+} \times \boldsymbol{S}_{-}) \cdot \hat{\boldsymbol{k}}^{-}$. Therefore, the sensitivity for the real part of the $\pi\pi$, πl and ll modes is much lower than that of the $\rho\rho$, $\rho\pi$ and ρl modes.

Furthermore, the term $(\hat{\boldsymbol{k}} \cdot \hat{\boldsymbol{p}})(\boldsymbol{S}_{+} \times \boldsymbol{S}_{-}) \cdot \hat{\boldsymbol{p}}$ is affected by the polar angle range of the particle selection. The range of the $(\hat{\boldsymbol{k}} \cdot \hat{\boldsymbol{p}})$ value is small for the $\pi\pi$ mode. Therefore, the sensitivity of the $\pi\pi$ mode is greatly reduced.

E.4.3 Imaginary part

Among the $\rho\rho$, $\pi\pi$ and $\pi\rho$ modes, a higher sensitivity for the $\pi\rho$ mode and a lower sensitivity for the $\pi\pi$ mode is found. This is because of the selection criteria for the polar angle. For the $\pi\pi$ mode, because of the particle selection, the range of the $(\hat{\boldsymbol{k}} \cdot \hat{\boldsymbol{p}})$ value is less than that for the $\rho\rho$ mode. Therefore, the sensitivity for the $\pi\pi$ mode becomes small. On the other hand, for the $\pi\rho$ mode, the distribution of the observable becomes wide because of the charge asymmetry of the distribution, as described in Section E.3.2. Therefore, the sensitivity for the $\pi\rho$ mode becomes large.

The difference in the sensitivity among the modes decaying to πl and ρl is due to the selection criteria of the particle momentum. The higher momentum lepton shows a better

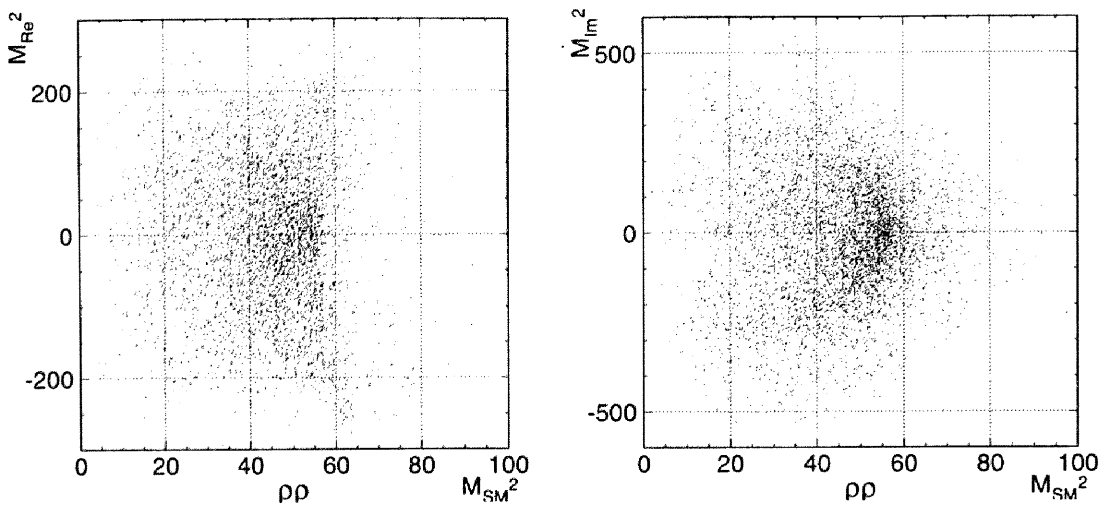

Figure E.5: Correlation between the amplitude $\mathcal{M}^2_{Re,Im}$ and $\mathcal{M}^2_{\rm SM}$ for the $\rho\rho$ mode.

spin-analyzing power. Therefore, the modes including μ show a higher sensitivity than the modes including an electron.

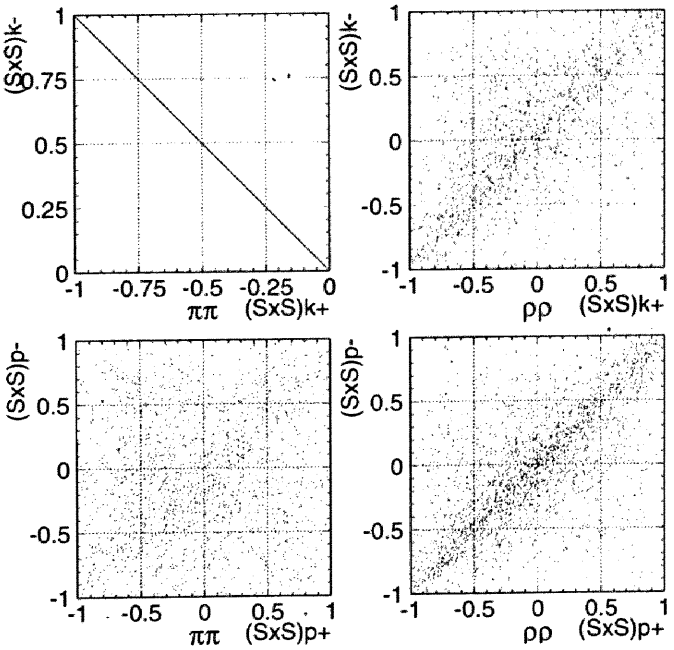

Figure E.6: Correlation between the case of two τ direction $\hat{k}_\pm$ for the $\pi\pi$ and $\rho\rho$ modes.

Appendix F

Effect of radiation

In this analysis, the unmeasured radiative photons are ignored in the calculation of the observables. These unmeasured variables make the sensitivity lower. This effect is examined by using the MC without the initial-state radiation and the internal bremsstrahlung at the τ decay vertex. Figure F.1 shows the sensitivity and the offset. The black points correspond to the case of no radiation, while the white points correspond to the default case used in this analysis. The sensitivity of the default case is lower than that of the case of no radiation, as we expected. That strength is only about 10%. The offsets for the real part are consistent with each other within the statistical errors. For the imaginary part, photons from the initial-state radiation escaping to the beam pipe direction contribute to the offset.

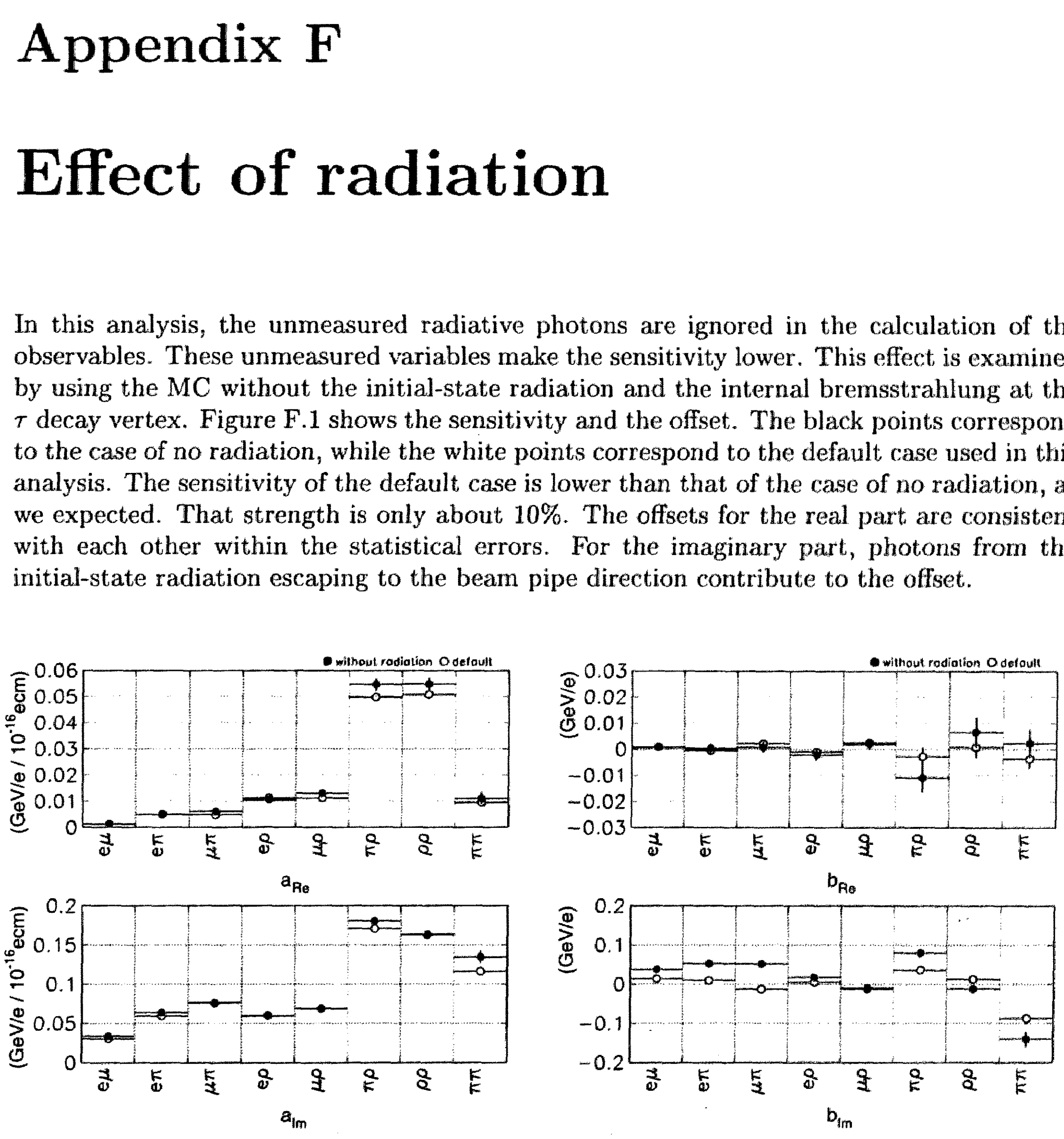

Figure F.1: EDM parameter sensitivity $a_{Re/Im}$ and offset $b_{Re/Im}$ for each mode obtained by MC without the initial-state radiation and internal bremsstrahlung (black points) and for the default (white points), which is the same as Figure 5.13. The top figures show the parameters for $Re(d_\tau)$ and bottom ones show the parameters for $Im(d_\tau)$. The errors are due to the MC statistics.

Additionally, the effect for only the (internal) bremsstrahlung is examined. Figure F.2 shows the sensitivity and offset by including the initial-state radiation events to the above test. The results show no significant change between the two case.

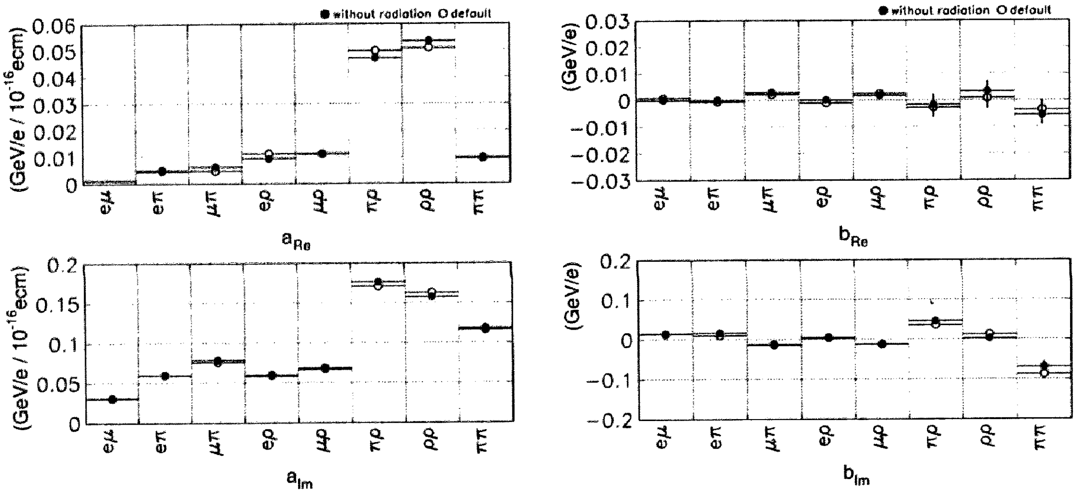

Figure F.2: EDM parameter sensitivity $a_{Re/Im}$ and offset $b_{Re/Im}$ for each mode obtained by MC without the (internal) bremsstrahlung only (black points) and for the default (white points), which is the same as Figure 5.13. The initial radiation is included. The top figures show the parameters for $Re(d_\tau)$ and bottom ones show the parameters for $Im(d_\tau)$. The errors are due to the MC statistics.

Bibliography

[1] Y. Fukuda et al. (Super-Kamiokande Collaboration), Phys. Rev. Lett. **81** (1998) 1562; Phys. Lett. **B436** (1998) 33; Phys. Rev. Lett. **85** (2000) 3999.

[2] K. Abe et al. (Belle Collaboration), Phys. Rev. Lett. **87** (2001) 091802; Phys. Rev. **D66** (2002) 032007.

[3] B. Aubert et al. (BaBar Collaboration), Phys. Rev. Lett. **87** (2001) 091801; Phys. Rev. **D66** (2002) 032003.

[4] M. Acciarri et al. (L3 Collaboration), Phys. Lett. **B434** (1998) 169.

[5] K. Ackerstaff et al. (OPAL Collaboration), Phys. Lett. **B431** (1998) 188.

[6] H. Albrecht et al. (ARGUS Collaboration), Phys. Rev. **B485** (2000) 37.

[7] J. D. Bjorken and S. D. Drell, "Relativistic Quantum Mechanics", McGraw-Hill.

[8] Y. Tsai, Phys. Rev. **D4** (1971) 2821.

[9] HELAS: K. Hagiwara, KEK report 91-11, January 1992.

[10] K. Hagiwara and D. Zeppenfeld, "Helicity Amplitudes For Heavy Lepton Production In E+ E- Annihilation", Nucl. Phys. **B274** (1986) 1.

[11] MadGraph: T. Stelzer and W. F. Long, Comput. Phys. Commun. **81** (1994) 357.

[12] W. Bernreuther, O. Nachtmann, and P. Overmann, Phys. Rev. **D48** (1993) 78.

[13] M. J. Booth, hep-ph/9301293.

[14] U. Mahanta, Phys. Rev. **D54** (1996) 3377.

[15] J. Q. Zhang, X. C. Song, W. J. Huo, and T. F. Feng, hep-ph/0205309.

[16] W. Bernreuther and O. Nachtmann, Phys. Rev. Lett. **63** (1989) 2787.

[17] Y. L. Wu and L. Wolfenstein, Phys. Rev. Lett. **73** (1994) 1762.

[18] A. Soni and R. M. Xu, Phys. Rev. Lett. **69** (1992) 33.

[19] T. Huang, W. Lu, and Z. Tao, Phys. Rev. **D55** (1997) 1643.

[20] W. Bernreuther, A. Brandenburg, and P. Overmann, Phys. Lett. **B391** (1996) 413; ibid., **B412** (1997) 425.

[21] D. Atwood and A. Soni, Phys. Rev. **D45** (1992) 2405.

[22] M. Davier et al., Phys. Lett. **B306** (1993) 411.

[23] W. Bernreuther, A. Brandenburg, and P. Overmann, Phys. Lett. **B391** (1997) 413; ibid., **B412** (1997) 425.

[24] W. Hollik et al., Phys. Lett. **B425** (1998) 322.

[25] A. Abashian et al. (Belle Collaboration), Nucl. Instr. and Meth. **A479** (2002) 117.

[26] KEKB accelerator group, KEKB B Factory Design Report, KEK Report 95-7, 1995; K. Akai et al., Proc. 1999 Particle Accelerator Conference, New York(1999); Y. Funakoshi et al., Proc. 2000 European Particle Accelerator Conference, Vienna(2000).

[27] KORALB(v.2.4)/TAUOLA(v.2.6): S. Jadach and Z. Wąs, Comp. Phys. Commun. **85** (1995) 453; ibid., **64** (1991) 267; ibid., **36** (1985) 191; S. Jadach, Z. Wąs, R. Decker, and J. H. Kühn, Comp. Phys. Commun. **64** (1991) 275; ibid., **70** (1992) 69; ibid., **76** (1993) 361.

[28] C. Caso et al., The Europian Physical Journal **C3** (1998) 1.

[29] R. Brun et al., GEANT 3.21, CERN Report No. DD/EE/84-1 (1987).

[30] 'QQ - The CLEO Event Generator' (http://www.lns.cornell.edu/public/CLEO/soft/QQ/).

[31] F. A. Berends, P. H. Daverveldt, and R. Kleiss, Comp. Phys. Commun. **40** (1986) 285.

[32] K. Hanagaki et al., Nucl. Instr. and Meth. A **485** (2002) 490.

[33] H. Sagawa et al. Belle note 502.

[34] R. Escribano and E. Massó, Phys. Lett. **B301** (1993) 419; Nucl. Phys. B **429** (1994) 19; Phys. Lett. **B395** (1997) 369.

[35] L. Silvestris, *A Test of CP-Invariance in* $Z \to \tau^+\tau^-$, talk presented at ICHEP96, Warsaw, 25-31 July 1996.

[36] T. Huang, Z. H. Lin, and X. Zhang, Phys. Lett. **B450** (1999) 257.

[37] J. Q. Zhang, X. C. Song, W. J. Huo, and T. F. Feng, hep-ph/0205309.

[38] B. C. Regan, E. D. Commins, C. J. Schmidt, and D. DeMille, Phys. Rev. Lett. **88** (2002) 071805.

[39] J. Bailey et al. (CERN-Mainz-Daresbury Collaboration), Nucl. Phys. **B150** (1979) 1.

[40] P. G. Harris et al., Phys. Rev. Lett. **82** (1999) 904.

[41] D. Cho, K. Sangsterm and E. A. Hinds, Phys. Rev. Lett. **63** (1989) 2559.

[42] X. G. He, B. H. J. McKellar and S. Pakvasa, Int. J. Mod. Phys. **A4** (1989) 5011.

[43] K. Ackerstaff et al. (OPAL Collaboration), Z. Phys. **C74** (1997) 403.